ORGANIC INORGANIC PHOTORESIST AND LASER INDUCED HEATING PROCESS FOR NEXT GENERATION LITHOGRAPHY

A Dissertation

Presented to the Faculty of the Graduate School

of Cornell University

in Partial Fulfillment of the Requirements for the Degree of

Doctor of Philosophy

By

Jing Jiang

July 2015

© 2015 Jing Jiang

ORGANIC INORGANIC PHOTORESIST AND LASER INDUCED HEATING PROCESS FOR NEXT GENERATION LITHOGRAPHY

Jing Jiang, Ph. D.

Cornell University 2014

What technology will enable lithography to continue Moore's law beyond 10 nm node? Traditional photolithography, using a 193 nm wavelength and chemically amplified resist (CAR), is currently the workhorse in the semiconductor industry, but faces challenge of achieving required resolution and line width roughness (LWR). Extreme Ultraviolet Lithography (EUVL), using 13.5 nm light, is considered as the likely successor to 193 nm immersion lithography, but has been delayed for years due to both light source and resist materials challenges. Directed self-assembly (DSA) of block copolymers, as a bottom-up approach, has the potential for high resolution, but its process integration is completely different from conventional top-down lithography. All of these different techniques coexist as competing solutions, but also facing challenges at the same time. So how can we enable these technologies for the next generation lithography? This dissertation explores the materials used in these three main categories of lithography technologies (CAR, EUVL and DSA), providing unconventional approaches to address this question.

Ultrafast and high temperature laser induced heating is utilized as a post exposure bake (PEB) method for chemically amplified photoresists. By studying the reaction and diffusion kinetics of photoresist systems during laser PEB, we have been able to correlate the apparent activation energies with pattern LWR for 193 nm

photoresists. We found that the system with highest deprotection activation energy and lowest diffusion activation energy achieved 60% LWR reduction using laser PEB compared to conventional hotplate annealing.

Laser annealing is also utilized for directed self-assembly of block copolymers. Polymer chain mobility is greatly increased by increasing temperature, allowing ordering within 5-20 ms before polymer decomposition can occur. Effects of laser power, dwell time, underlayer and graphoepitaxy were examined with long range order and alignment was achieved with 20 ms laser annealing.

Ligand-stabilized metal oxide nanoparticles resist have shown extraordinary sensitivity for EUV lithography (4.2 $mJ/cm^2$for the 22 nm features). This study suggests that ligands can be directly cleaved by UV radiation, which is accelerated in the presence of a photoacid generator (PAG). This implies that the ligand structures is important to resist performance. By systematically synthesizing and characterizing of nanoparticles with different ligands, we correlated the lithographic performance with ligand structures, offering the potential for future rational resist design.

BIOGRAPHICAL SKETCH

Jing Jiang was born in Xiamen, China on April 15th 1988. She grew up in a happy and open-minded family. They were supportive, allowing her to freely explore her interests and make decisions for her own life. When she was a child, she dreamed to be a super model or a business woman or even an astronaut. Her grandfather, a chemistry professor, deeply influenced her life and introduced her to the world of science. When entering into college, she chose pharmaceutical engineering as a major since she considered herself more an engineer for problem solving than a pure scientist.

In Tianjin University, she worked under Professor Yingjin Yuan and it was the first time she started to explore the unknown world. She learned to culture cells, extract metabolites and proteins and carefully analyzed data to understand a cell's response to production environment stress. She loved bioengineering experiments so much that she never thought she would work on something totally different in the future.

When she came to Cornell and joined Professor Ober's group, she didn't even know what lithography was. Yet she was never afraid of learning everything from zero as her family always encouraged her since childhood. However, this was one of the toughest times in her life. She struggled with culture shock, language disadvantages and the lack of relevant background. Almost nothing worked out in the beginning. Luckily she met some church friends in the cleanroom and they not

Lam Research Ex. 1013 - Page 5
Lam Research Corp. v. Inpria Corp.
IPR2025-00256 - U.S. Patent No. 11,537,048

only helped her with many techniques but also gave her help and suggestions in life and career.

During the past five years, she encountered a lot of frustration not only in research but also in the funding situation. However, she always counted the blessings she received and knew God always opens a way. As time passed, she became mature under the guidance of Professor Ober. She gave presentations in many occasions, meeting people from both academia and industry. Finally, she completed her degree and is looking forward to start a thrilling life on yet another continent.

Lam Research Ex. 1013 - Page 6
Lam Research Corp. v. Inpria Corp.
IPR2025-00256 - U.S. Patent No. 11,537,048

To the memory of my late grandfather

and my family.

Lam Research Ex. 1013 - Page 7
Lam Research Corp. v. Inpria Corp.
IPR2025-00256 - U.S. Patent No. 11,537,048

ACKNOWLEDGMENTS

All praise, honor and glory to my Lord Jesus Christ for His richest grace and mercy for bringing me from China to the US and the accomplishment of Ph.D. study.

I would like to acknowledge the individuals who have loved, supported and guided me throughout the journey of pursuing Ph.D.

First and foremost, I would like to thanks my grandfather Qiwen Jiang and grandmother Peifen Li for their unconditional love and encouragements to live up my dreams, my parents Shaoming and Zhihong for their love and support. I also thank my uncle Shaoyi Jiang for helping me to find college and grad school.

Second, I would like to thank my thesis advisor Professor Christopher Ober, who accepted me into his group and has been very patient especially when I first came and was struggling to adjust myself to American cultures and to become professional in academia. I would also like to give sincere thanks to Professor Michael Thompson, as my project co-adviser as well as Professor Archer and Professor Cohen as my committee members, for valuable suggestions.

I am very grateful to receive financial support from Intel, Semiconductor Research Corporation, GLOBALFOUNDRIES, SEMATECH, Elia Life for various projects. I would like to thank Kenji Yoshimoto, Deniz Civay, Mark Neisser, JunSung Chun particularly for their guidance in my research. I also gratefully acknowledge the staff of CNF, CCMR, NBTC, CHESS and LBNL for their assistance in running tools and experiments.

Then I thank all the colleagues in the Ober group. It is a pleasure to work with such a group of smart and friendly people. I give my special thanks to Byungki Jung as

Lam Research Ex. 1013 - Page 8
Lam Research Corp. v. Inpria Corp.
IPR2025-00256 - U.S. Patent No. 11,537,048

my mentor when I first joined the group, to helping me to start my research. I would also like to mention Christine Ouyang, Brandon Wenning, Lin Chen and Yefei Zhang who are great friends and are always there when I need help. I also want to thank those postdocs who taught me a lot of things including Clemens Liedel, Yisheng Xu, Kui Xu, Ben Zhang, Li Li, Myungwoong Kim, Souvik Chakrabarty, Yoojin Choo, Yosuke Hoshi, Youyong Xu, Youngjin Cho and Yeon Sook Chung.

I am truly blessed to meet Lianwee Luo and Yih Lin Goh and Edwin and Jyying Kan couple in my first year. They helped in every way they can selflessly. Since I just moved to a totally different culture, their love and encouragement meant a lot during that time and throughout these years. To Lieh-Ting Tung, you are an angel. Thank you for always being there, helping me every time I was desperate, and providing me sincere suggestions when I need guidance in career and life. Finally, I would like to express my appreciation to brothers and sisters in First Ithaca Chinese Christian Church and Cornell Chinese Christian Fellowship. Without the love and support from all friends and Christian family, I would not have survived grad school.

Lam Research Ex. 1013 - Page 9
Lam Research Corp. v. Inpria Corp.
IPR2025-00256 - U.S. Patent No. 11,537,048

TABLE OF CONTENTS

CHAPTER 1 Introduction to lithography and laser spike annealing

1.1. Nanolithography 1

1.2. The current status and prospects of next generation nanolithography 3

1.3. DUV lithography 5

1.3.1. Chemically amplified photoresist 8

1.3.2. Photoacid generator (PAG) and acid diffusion 9

1.4. Directed self-assembly of block copolymer 15

1.4.1. Block copolymer 15

1.4.2. Thermal annealing vs. solvent annealing 17

1.4.3. Directed self-assembly for nanopatterning 18

1.5. EUV lithography 23

1.5.1. EUV scanner and mask 23

1.5.2. EUVL resist 24

1.6. Laser Spike Annealing 27

1.6.1. Shallow Junction Annealing and Diffusion Control 27

Lam Research Ex. 1013 - Page 10
Lam Research Corp. v. Inpria Corp.
IPR2025-00256 - U.S. Patent No. 11,537,048

1.6.2. Laser spike annealing of organic systems 29

1.6.3. Cornell Laser system and temperature calibration 31

CHAPTER 2 Millisecond laser peak temperature calibration by platinum thermistor

2.1. Introduction 44

2.2. Experimental methods 45

2.2.1. Platinum thermistor fabrication 45

2.2.2. Temperature calibration by Si Au melting experiment 48

2.2.3. Resistivity data acquisition 49

2.3. Results and discussion 55

CHAPTER 3 Small-molecule driven chemical reaction and diffusion kinetics during laser-induced sub-millisecond heating for patterning applications

3.1. Introduction 64

3.2. Results and discussion 66

3.2.1. Ultrafast laser spike annealing and temperature calibration 66

3.2.2. The interplay of photopolymer and photoacid generator 66

3.2.3. Characterization of deprotection during millisecond PEB 73

Lam Research Ex. 1013 - Page 11
Lam Research Corp. v. Inpria Corp.
IPR2025-00256 - U.S. Patent No. 11,537,048

3.2.4. Characterization of acid diffusivity 77

3.2.5. E-beam pattering and line width roughness of the resists 80

3.3. Conclusions 84

3.4. Materials and methods 85

3.4.1. Materials and reagent 85

3.4.2. Synthesis 85

3.4.3. Methods 87

3.4.4. Heat treatment 88

CHAPTER 4 Ultrafast self-assembly of sub-10 nm block copolymer nanostructures by solvent-free laser annealing at high temperature

4.1. Introduction 92

4.2. Results and discussion 94

4.2.1. Microphase separation by laser spike annealing 94

4.2.2. Influence of laser power and dwells on BCP ordering 97

4.2.3. The influences of substrate surface modification on thin film BCP morphology during laser annealing 102

4.2.4. Graphoepitaxy assisted self-assembly by laser annealing 103

Lam Research Ex. 1013 - Page 12
Lam Research Corp. v. Inpria Corp.
IPR2025-00256 - U.S. Patent No. 11,537,048

4.3. Conclusions 104

4.4. Experimental Section 105

CHAPTER 5 Mechanism studies of carboxylic acid ligand stabilized metal oxide nanoparticle EUV (ONE) resist

5.1. Introduction and motivation 111

5.2. Experimental 115

5.2.1. Materials 115

5.2.2. Nanoparticles synthesis 115

5.2.3. Physical characterization 116

5.3. Results and discussion 119

5.3.1. Synthesis 119

5.3.2. Structural characterization 119

5.3.3. Organic content and ligand strength measurement by TG/DTA studies 123

5.3.4. Effects of post-exposure bake on negative tone development process 129

Lam Research Ex. 1013 - Page 13
Lam Research Corp. v. Inpria Corp.
IPR2025-00256 - U.S. Patent No. 11,537,048

5.3.5. Mechanism for the solubility switch for the cases of exposure only and of exposure with PEB 133

5.4. Conclusion 139

CHAPTER 6 New ligand compositions for metal oxide nanoparticle EUV resist

6.1. Introduction 144

6.2. Experimental 145

6.2.1. Materials 145

6.2.2. Nanoparticles synthesis 145

6.2.3. Physical characterization 147

6.3. Results and discussion 149

6.3.1. Synthesis 149

6.3.2. Characterization 150

6.3.3. Ligand binding strength measured by TG/DTA 152

6.3.4. Effect of ligand on nanoparticle solubility 158

6.3.5. DUV patterning of nanoparticle resist 160

6.3.6. The effects of base quenchers on EUV patterning of ZrO_2-MAA ... 163

Lam Research Ex. 1013 - Page 14
Lam Research Corp. v. Inpria Corp.
IPR2025-00256 - U.S. Patent No. 11,537,048

6.3.7. Shelf life studies of nanoparticles. 164

6.3.8. Development process 167

6.4. Conclusion 169

Lam Research Ex. 1013 - Page 15
Lam Research Corp. v. Inpria Corp.
IPR2025-00256 - U.S. Patent No. 11,537,048

LIST OF FIGURES

Figure 1.1 The evolution of photolithography. The number of transistors produced by Intel increased from 2,300 to 1,400,000,000 between 1970's and 2010's. The wavelength for imaging tool shift from 436 nm to 193nm. The photoresist materials also changed from DNQ type resist to ESCAP and polymethacrylate as shown.

Figure 1.2 The International Technology Roadmap for Semiconductors, 2013 edition. Reprinted with permission from reference [23]. Copyright 2013 ITRS.

Figure 1.3 Typical lithographic processes.

Figure 1.4 Photoresist structures for (a) 248 nm and (b) 193 nm lithography.

Figure 1.5 Typical (a) ionic and (b) nonionic PAG structures.

Figure 1.6 Typical chemically amplification reaction during PEB.

Figure 1.7 Acid generation mechanism of triphenylsulfonium salt PAGs. Reprinted with permission from ref.29. Copyright 2005 Springer.

Figure 1.8 Acid diffusion length measurement by bilayer method.

Figure 1.9 Morphology changes as the volume fraction of polystyrene in polystyrene-polyisoprene (PS-*b*-PI) changes. Spherical, cylindrical, ordered bicontinuous double diamond and lamellar structures were found in PS-*b*-PI. Reprinted with permission from ref. 35, copyright 1990 Annual Reviews Inc.

Lam Research Ex. 1013 - Page 16
Lam Research Corp. v. Inpria Corp.
IPR2025-00256 - U.S. Patent No. 11,537,048

Figure 1.10 Theoretical phase diagram for diblock copolymer melts using self-consistent field theory. Phases are labeled D (disordered), C (cubic), H (hexagonal), G (gyroid) and L (lamellar). Dashed lines are extrapolated phase boundaries and the dot denotes the critical point. Reprinted with permission from ref. 36, copyright 1994 American Physical Society.

Figure 1.11 Semilog plot of annealing time as a function of inverse temperature for the minimum time observed for defect free assembly (solid square) and the maximum time for which abundant defects (open circle) still persisted. Reprinted with permission from ref.40, copyright 1994 American Physical Society.

Figure 1.12 Common IC patterns that are self-assembled from block copolymers. Reprinted with permission from ref.48, copyright 2007 American Institute of Physics.

Figure 1.13 Graphoepitaxy makes uses of confinement effects. ref.71, copyright 2007 American Chemical Society.

Figure 1.14 Alignment mechanism. Lines begin to locate from the edge to the entire trench width (e) 9 h, (f) 14 h, (g) 19 h, (h) 24 h, and (i) 33h at 130 °C. Reprinted with permission from ref.58, copyright 2004 American Chemical Society.

Figure 1.15 EUV radiation generation mechanism. Reprinted with permission from ref.6, copyright 2010 Macmillan Publishers Limited.

Lam Research Ex. 1013 - Page 17
Lam Research Corp. v. Inpria Corp.
IPR2025-00256 - U.S. Patent No. 11,537,048

Figure 1.16 Gate structure of CMOS device. Dopant diffusion into depletion region during thermal process after ion implantation limit the use of ultra-shallow junction.

Figure 1.17 Dopant concentration near the surface under different annealing conditions. Dopant diffusion length decrease as the annealing time decrease. Reprinted from ref.109, copyright 1987 American institute of Physics.

Figure 1.18 Thermal stability of PS-b-PDMS. a) thickness decreases as a function of increasing temperature for various dwell times. The shorter the dwell time, the higher the temperature that a polymer can withstand under transient heating. b) Decomposition rate of PS-b-PDMS as a function of temperature during laser annealing in an Arrhenius plot and the slope is the thermolysis activation energy. Reprinted from ref.[122] copyright © 2014 Byungki Jung.

Figure 1.19 Cornell laser systems: diode laser and CO_2 laser. Reprinted from ref.121 copyright © 2014 Byungki Jung.

Figure 1.20 Incident laser intensity profile at the sample of a) the CO_2 laser and b) the diode laser.

Figure 2.1 Platinum thermistor design: a) detailed schematic plot of the platinum measurement resistor. b) circuit patterns of the thermistor of the Pt layer. Six squares shown here are used as contacts to the center platinum resistor. The zoom in images shows the structures of the platinum resistor. c) mask for the thick of the Ni layer.

Lam Research Ex. 1013 - Page 18
Lam Research Corp. v. Inpria Corp.
IPR2025-00256 - U.S. Patent No. 11,537,048

Figure 2.2 Schematic figure of thermistor stack cross-section.

Figure 2.3 Image of platinum thermistor for temperature calibration.

Figure 2.4 Images of Si and Au melting. Reprinted from ref.12.

Figure 2.5 Schematic of thermistor measurement.

Figure 2.6 Platinum thermistor design a) detailed schematic plot of the platinum measurement resistor. b) circuit patterns of the thermistor of the Pt layer. Six squares shown here are used as contacts to the center platinum resistor. Part a) reflects the structures of the platinum resistor. c) mask for the thick of the Ni layer.

Figure 2.7 Output from the oscilloscope. Channel 1 shows the voltage change across the thermistor and Channel 2 shows the voltage across the 50 Ω resistor, which measured the current.

Figure 2.8 Orientation of the diode laser across the thermistor device.

Figure 2.9 Peak resistivity change as a function of lateral beam position. The center of the scanning laser 2.8 mm in this example, with a relatively constant temperature zone approximately 1 mm wide. (This data was obtained before laser reinstall on 2011.11)

Figure 2.10 Time dependent Pt resistivity change during a 10ms dwell laser scan at 40W.

Lam Research Ex. 1013 - Page 19
Lam Research Corp. v. Inpria Corp.
IPR2025-00256 - U.S. Patent No. 11,537,048

Figure 2.11 Pt thermistor resistivity as a function of power for dwell times from 2 ms to 20 ms.

Figure 2.12 Measured and extrapolate ΔR/R as a function of the incident laser power for a dwell of 10 ms. Extrapolating curve to the Si melting power provides an absolute temperature calibration. (This data was obtained before laser reinstall at 2011.11)

Figure 2.13 Peak resistivity for several dwell times and their quadric fits.

Figure 2.14 Temperature as functions of laser power for 5, 10, 20 ms dwells during diode laser annealing.

Figure 2.15 Temporal temperature profile.

Figure 2.16 Spatial temperature profile.

Figure 3.1 Schematic Arrhenius plot of ideal resist system for laser spike annealing. Both deprotection rate and diffusivity increase with increasing temperature and the slopes are their activation energy. An ideal resist system for laser PEB should have (a) a high deprotection activation energy and (b) a low diffusion activation energy.

Figure 3.2. Chemical structures of the three resists studied in this work. The photoresists were built on the same molecular weight polyhydroxystyrene with selectively varied side chains.

Lam Research Ex. 1013 - Page 20
Lam Research Corp. v. Inpria Corp.
IPR2025-00256 - U.S. Patent No. 11,537,048

Figure 3.3 Method to determine the deprotection temperature at given reaction time. For thermolysis measurement, the resist film without PAG is scanned by a laser at a set velocity but with increasing powers. For the acid deprotection measurement, the PAG containing resist is exposed at a fixed dose before laser PEB. As the peak temperature is increased, film transit from no dissolution to full dissolution in TMAH solution during development. The lowest temperature required for full development is recorded as a function of heating duration, yielding an Arrhenius plot of the reaction rate versus temperature.

Figure 3.4 Arrhenius thermolysis plot of t-BOC, t-BOCM and AD under laser PEB.

Figure 3.5 Chemical structure of the PAGs. These two PAGs have the same UV absorbing unit, the cation. TPS-nf is a common single activation site 248 nm PAG with a fluorinated counter ion, while 3P3A has three activation sites with three counter ions bound to a molecule glass core.

Figure 3.6 The Arrhenius deprotection plot of *t*-BOC, *t*-BOCM and AD under laser PEB. The resists were loaded with 5 wt. % TPS-nf and exposed at 248 nm for 3.4 mJ/cm^2.

Figure 3.7 Arrhenius deprotection plot of AD with (a) TPS-nf and (b) 3P3A at three doses under laser PEB. At lower dose, fewer acids are generated and hence higher temperature are required to increase the diffusion to complete the deprotection within given annealing time. However, the deprotection activation energy is

Lam Research Ex. 1013 - Page 21
Lam Research Corp. v. Inpria Corp.
IPR2025-00256 - U.S. Patent No. 11,537,048

primarily dependent on the resist chemistry and only weakly dependent on UV dose or PAG molecule.

Figure 3.8 Arrhenius plot of acid diffusivity, determined with bilayer technique, of TPS-nf in three resist resins *t*-BOC, *t*-BOCM and AD under laser PEB. The resist film is flood exposed at 248 nm for 34 mJ/cm^2, activating 90% of the PAG.

Figure 3.9 Arrhenius plot of acid diffusivity of TPS-nf and 3P3A in AD resist resin under laser PEB. The resist film was flood exposed at 248 nm for 34 mJ/cm^2.

Figure 3.10 SEM images of e-beam lithography showing the highest resolution obtained under each condition. Images on the left are under hotplate PEB and images on the right are under laser PEB. Patterning condition and results are summarized in Table 3.2.

Figure 4.1 In situ measured temperature profiles for dwell times of 5 ms, 10 ms and 20 ms. The time origin in each condition is set to when the peak temperature is reached.

Figure 4.2 Structures of PS-b-PMDS used in this work.

Figure 4.3 Microphase separation of PS-b-PDMS by laser annealing for 3 ms at approximately 200 °C (50W).

Figure 4.4 SEM images of laser annealed films composed of PS-*b*-PDMS on Si wafers that have previously been modified with PS brushes. The annealing temperature for each sample is indicated in each image.

Lam Research Ex. 1013 - Page 22
Lam Research Corp. v. Inpria Corp.
IPR2025-00256 - U.S. Patent No. 11,537,048

Figure 4.5 GISAXS of laser annealed film composed of PS-*b*-PDMS on top of PS brush modified Si wafers. (a) GISAXS of sample annealed at 250 °C (45 W) for 10ms. (b) GISAXS of the same sample etched; a secondary peak is now clearly observed. (c) GISAXS traces from non-etched samples as a function of annealing temperature (power).

Figure 4.6 Schematic plot of the ordering process for different conditions. (a) Time temperature profiles for three annealing conditions. (b) Ordering characteristic as a function of time for these conditions. Between Tg and T_{ODT}, the ordering increases while above T_{ODT} the ordering decrease. The ultimate ordering depends critically on the time above T_{ODT} and the cooling rate to Tg.

Figure 5.1 ONE resist scheme.

Figure 5.2 Atomic EUV absorbance cross section.

Figure 5.3 HfO_2-MAA nanoparticle size distribution measured by DLS.

Figure 5.4 SAXS of HfO_2-MAA powders.

Figure 5.5 FTIR of ZrO_2-MAA (top) and free MAA (bottom).

Figure 5.6 XPS spectrum of ZrO_2-MAA. a) a full scan of hybrid nanoparticles b) Zr 3d region c) C 1s region d) O 1s region.

Figure 5.7 DTA curves of HfO_2-MAA.

Figure 5.8 TGA of ZrO_2-MAA hold at 154 °C and 341 °C for 20 mins.

Lam Research Ex. 1013 - Page 23
Lam Research Corp. v. Inpria Corp.
IPR2025-00256 - U.S. Patent No. 11,537,048

Figure 5.9 Dissolution rate of nanoparticles in 4M2P before and after annealed at 154 °C.

Figure 5.10 FTIR of nanoparticles sample for non-thermal treatment, nanoparticles heated to 154 °C or 341 °C.

Figure 5.11 Contrast curves of ZrO_2-MAA under different PEB conditions.

Figure 5.12 Effects of PEB on the pattern width and negative tone resist thickness.

Figure 5.13 Dissolution rate of ZrO_2-MAA after PEB.

Figure 5.14 Contact aligner line space patterns of HfO_2-2-methyl-2-pentenoic acid at various PEB temperatures and developed in 4M2P (250 mJ/cm^2, 254 nm).

Figure 5.15 TGA of ZrO_2-MAA with 5 wt. % PAG heated at 110 °C 130 °C for 20 mins before and after 150 mJ/cm^2 DUV exposure.

Figure 5.16 FTIR absorbance spectra of PEB and developed ONE resist film on Si

Figure 5.17 XPS spectra of ZrO_2-MAA. a) O1s region is convoluted into 3 components b) O1s region of non-expose, exposed and PEB films.

Figure 5.18 FTIR of ZrO_2-MAA exposed and non-expose samples. Zr-OH absorbance between 3600 cm^{-1} -3800 cm^{-1} increase after exposure.

Figure 5.19 Nanoparticle hydrodynamic size distribution with and without exposure.

Lam Research Ex. 1013 - Page 24
Lam Research Corp. v. Inpria Corp.
IPR2025-00256 - U.S. Patent No. 11,537,048

Figure 5.20 Schematic plot of negative tone patterning mechanism of ONE resist.

Figure 6.1 Chemical structures of ligands for solubility tests.

Figure 6.2 FTIR spectra of HfO_2 nanoparticles with 12 different ligands.

Figure 6.3 TGA of HfO_2 nanoparticles with 12 different ligands.

Figure 6.4 TG/DTA/DTG analysis of nanoparticles with aliphatic and aromatic ligands.

Figure 6.5 Dissolution rate of HfO_2-IBA, HfO_2-MAA, HfO_2-IPA, HfO_2-SA, HfO_2-MVA and HfO_2-MPA in 4M2P without and with exposure.

Figure 6.6 DUV patterning results of nanoparticles with various ligands.

Figure 6.7 Effects of mixing nanoparticles with different solubility on the patterning

Figure 6.8 Chemical structures of base quencher DBU.

Figure 6.9 EUV patterning of ZrO_2-MAA with DBU.

Figure 6.10 Nanoparticle size change in solution after aging samples for 3 weeks.

Figure 6.11 EUV patterning of aged solution. a) 10 days b) 45 days c) 80 days

Figure 6.12 Schematic plot of two development processes

Lam Research Ex. 1013 - Page 25
Lam Research Corp. v. Inpria Corp.
IPR2025-00256 - U.S. Patent No. 11,537,048

Figure 6.13 Comparison of ZrO_2-MAA using dip-blow and puddle-spin development. Resist residue was found to redeposit on the patterns.

Figure 6.6.14 Effects of development recipe for 248 nm DUV patterning of ZrO_2-MAA. The first row is a bright field sparse line space patterns; second row is dark field sparse patterns; third row is bright field dense patterns; fourth row is dark field dense patterns.

Lam Research Ex. 1013 - Page 26
Lam Research Corp. v. Inpria Corp.
IPR2025-00256 - U.S. Patent No. 11,537,048

LIST OF TABLES

Table 1.1 Summary of various polymer thermal decomposition temperature for a 60 s hot plate heating and laser annealing for 50 μs. Reprinted from ref.122 copyright © 2014 Byungki Jung.

Table 2.1 Fitting parameters of second order polynomial equation for 5, 10, 20 ms.

Table 2.2 Au and Si melting power for 10, 20 ms diode laser annealing.

Table 3.1 The deprotection and diffusion activation energy of the resist systems.

Table 3.2. Patterning conditions and results using e-beam lithography.

Table 5.1 Elemental ratio of ZrO_2-MAA films by XPS

Table 6.1 First ligand loss onset temperature of nanoparticles.

Table 6.2 Maximum ligand loss temperature of nanoparticles.

Lam Research Ex. 1013 - Page 27
Lam Research Corp. v. Inpria Corp.
IPR2025-00256 - U.S. Patent No. 11,537,048

CHAPTER 1 INTRODUCTION TO LITHOGRAPHY AND LASER SPIKE ANNEALING

Abstract

Lithography is a key process for microelectronic fabrication. In this thesis different materials for lithography, including chemically amplified photoresists, block copolymers and ligand stabilized metal oxide nanoparticles were studied. Ultrafast laser annealing was used to study aspects of resist behavior including reactions, diffusion and phase separation at high temperatures. In this chapter, a background of lithography and previous research achievements of these materials will be discussed. In the concluding section, we will review the applications of laser annealing in photoresist processing.

1.1. Nanolithography

The word “lithography” combines two terms: “lithos” meaning stone and “grapho” meaning writing; lithography literally means writing on stone. Nanolithography is a patterning method used by the semiconductor industry, which writes integrated circuit (IC) patterns on silicon substrates. Instead of directly engraving structures on Si substrates, patterns are first generated on sacrificial materials coated on the substrate. These sacrificial materials that act as temporary resist layers during reactive ion etching (pattern transfer steps), and are eventually stripped away. The ability to generate patterns with a reduced minimum feature size or critical dimension (CD) is one driving force for the evolution of microelectronic

Lam Research Ex. 1013 - Page 28
Lam Research Corp. v. Inpria Corp.
IPR2025-00256 - U.S. Patent No. 11,537,048

devices. The year by year trend of reducing CD to boost the device performance and increasing the transistor density is the basis of the famous “Moore’s Law”.

The co-founder of Intel, Gordon E. Moore published an article in *Electronics* on April 19, 1965 where he predicted that circuit densities of semiconductors would continuously double on a regular basis according to his observation for the previous five years.[1] Since then “Moore’s law” has provided a roadmap for the advance of microelectronics and has remained valid for 50 years.

Photolithography has made major contributions to this advancement. Lithography employs photons and masks to create patterns on light sensitive films (also known as photoresists). Light that is projected through a mask enables chemical reactions of the light sensitive materials, transferring patterns from masks to the photoresist thin film. Mid ultraviolet 436 nm (g-line) and 365 nm (i-line), and deep ultraviolet (DUV) 248 nm (KrF) radiation have been used previously for photolithography.[2–4] Currently, DUV 193 nm (ArF) lithography is the workhorse for the semiconductor industry[5] and extreme ultraviolet (EUV) lithography 13.5 nm has been extensively explored in recent years as a successor to DUV photolithography.[6,7] All these methods are so called masked lithography which also includes other forms such as nanoimprint[8–10] and soft lithography.[11]

The alternative to masked lithography is maskless lithography. Maskless lithography uses computers to control the scanning path of beams and reactions occurs where the beam has scanned. E-beam lithography[12,13], scanning probe lithography[14,15] and focused ion beam lithography[16,17] are forms of maskless lithography. In recent years, directed self-assembly of block copolymers (DSA) has emerged as a bottom up maskless lithography option, where the

Lam Research Ex. 1013 - Page 29
Lam Research Corp. v. Inpria Corp.
IPR2025-00256 - U.S. Patent No. 11,537,048

patterns are determined by polymer composition, the chemistry and substrate topography.[18–20] After selective removal of one phase or one block, the other phase then serves as patterned resist. All these techniques mentioned above together drive advances in the semiconductor industry.

1.2. The current status and prospects of next generation nanolithography

The history of lithography is the continuous size diminution of the pattern sizes. Scaling down transistors dimension not only increases the densities of circuits and the manufacturing throughput, but also improves circuit speed and power efficiency. To achieve smaller features, both optics and materials must evolve.

The minimum resolution is established theoretically by Rayleigh's equation,

$$\mathrm{R} = \frac{\mathrm{k} \cdot \lambda}{NA}$$

where, R is the minimum resolution, k is a process constant, λ is the exposure wavelength and NA is the optic systems numerical aperture. In order to achieve smaller resolution, the exposure wavelength has evolved for several generations from g-line (436 nm), i-line (365 nm), KrF (248 nm) to ArF (193nm) (Figure1.1). In 2002, Dr. Burn Lin proposed immersing the optics into purified water. [21] Since the numerical aperture of the lens NA is the product of n and sin θ, where n is the refractive index of the medium and θ is one-half the angular aperture, increasing refraction index from 1 of air to 1.44 of water successfully enhanced the resolution of 193 nm lithography by 30-40%.[22] As the lithography wavelength evolved, photoresist materials also need to adapt to these changes. (Figure 1.1).

Lam Research Ex. 1013 - Page 30
Lam Research Corp. v. Inpria Corp.
IPR2025-00256 - U.S. Patent No. 11,537,048

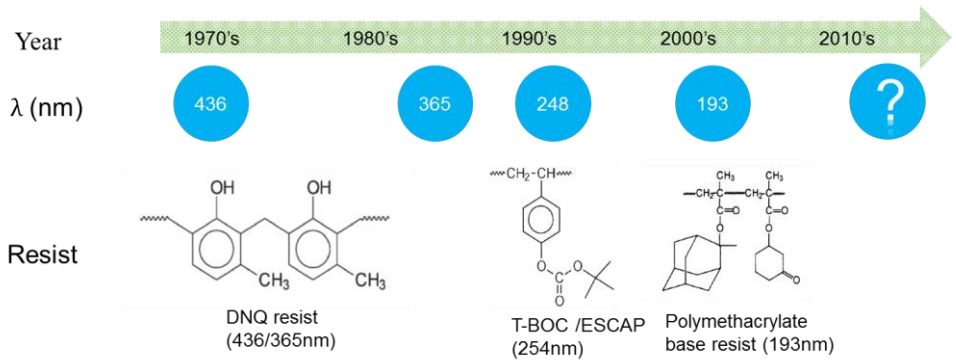

Figure 1.1 The evolution of photolithography. The number of transistors produced by Intel increased from 2,300 to 1,400,000,000 between the 1970's and 2010's. The wavelength for imaging tool shift from 436 nm to 193nm. The photoresist materials also changed from DNQ type resist to ESCAP and polymethacrylate as shown.

The semiconductor industry currently used 193 nm immersion lithography with double patterning techniques. However, continuing to decrease the resolution using current technologies is difficult, and as a result we are at a turning point to decide the next generation of photolithography. The latest International Roadmap for Semiconductors (ITRS) released at 2014, shown in Figure 1.2, lists 193 nm immersion lithography with quadric patterning (using chemically amplified resists), EUVL and DSA as the choices to be narrowed by 2015.[23] The background, advantages and drawbacks of each technology will be discussed in detail in this chapter. In this thesis, the author made efforts to understand the fundamentals of these technologies by using ultrafast laser annealing at high temperature and exploring the potential of these techniques to form finer patterns.

Lam Research Ex. 1013 - Page 31
Lam Research Corp. v. Inpria Corp.
IPR2025-00256 - U.S. Patent No. 11,537,048

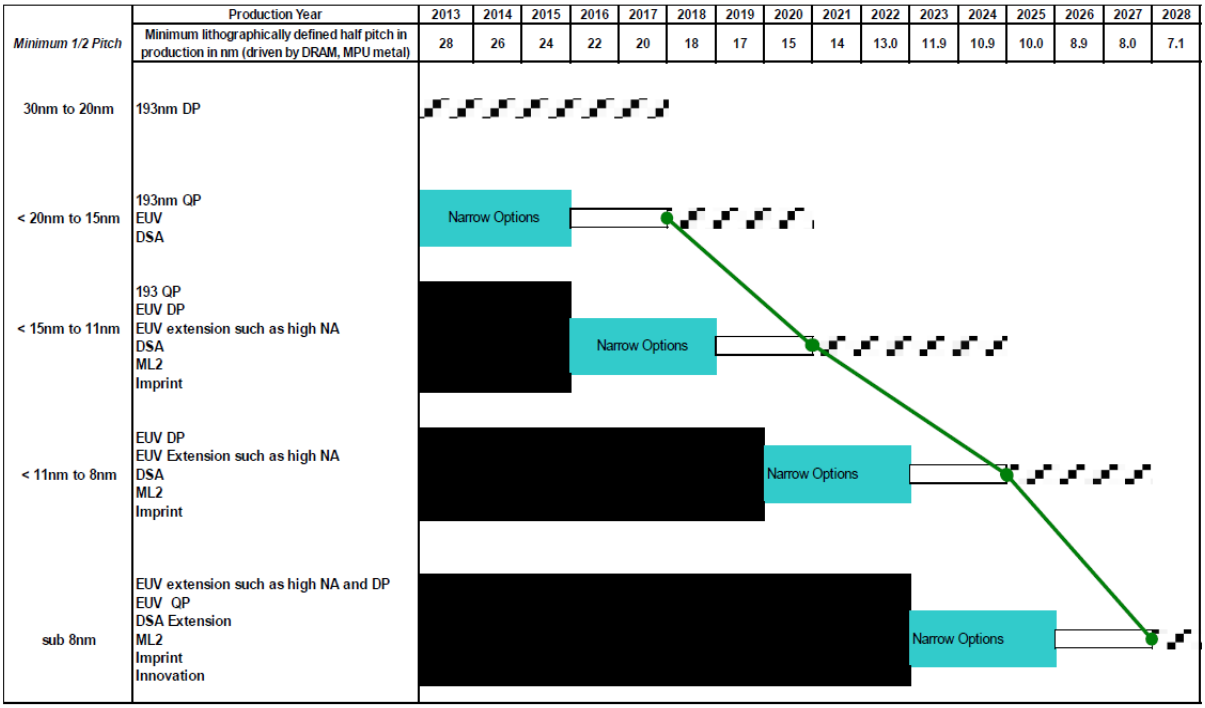

Figure 1.2 The International Technology Roadmap for Semiconductors, 2013 edition. Reprinted with permission from reference [23]. Copyright 2013 ITRS.

1.3. DUV lithography

The typical lithographic process is depicted in Figure 1.3. First, a photoresist solution loaded with photoacid generator (PAG) is spun coated onto the substrates, followed by a post-apply bake (PAB) step to remove residual solvents. Afterwards, photoresist is exposed to ultraviolet (UV) light through a patterned mask. Protons are generated from the decomposition of PAG in the exposed region, catalyzing reactions during the subsequent post-exposure bake (PEB) process. As a result, the compositions of the exposed photoresist changes, leading to a solubility switch in the developer. If the exposed resist become soluble in developer, it is a

Lam Research Ex. 1013 - Page 32
Lam Research Corp. v. Inpria Corp.
IPR2025-00256 - U.S. Patent No. 11,537,048

positive tone process; if the exposed resist become insoluble in the developer, it is a negative tone process. Patterns are transferred from masks to the resist by these means. During reactive ion etching (RIE), remaining photoresist films provides etch resistance and thus patterns are transferred to the substrates. After etching, the resist can be stripped away by wet etching and ashing.

Lam Research Ex. 1013 - Page 33
Lam Research Corp. v. Inpria Corp.
IPR2025-00256 - U.S. Patent No. 11,537,048

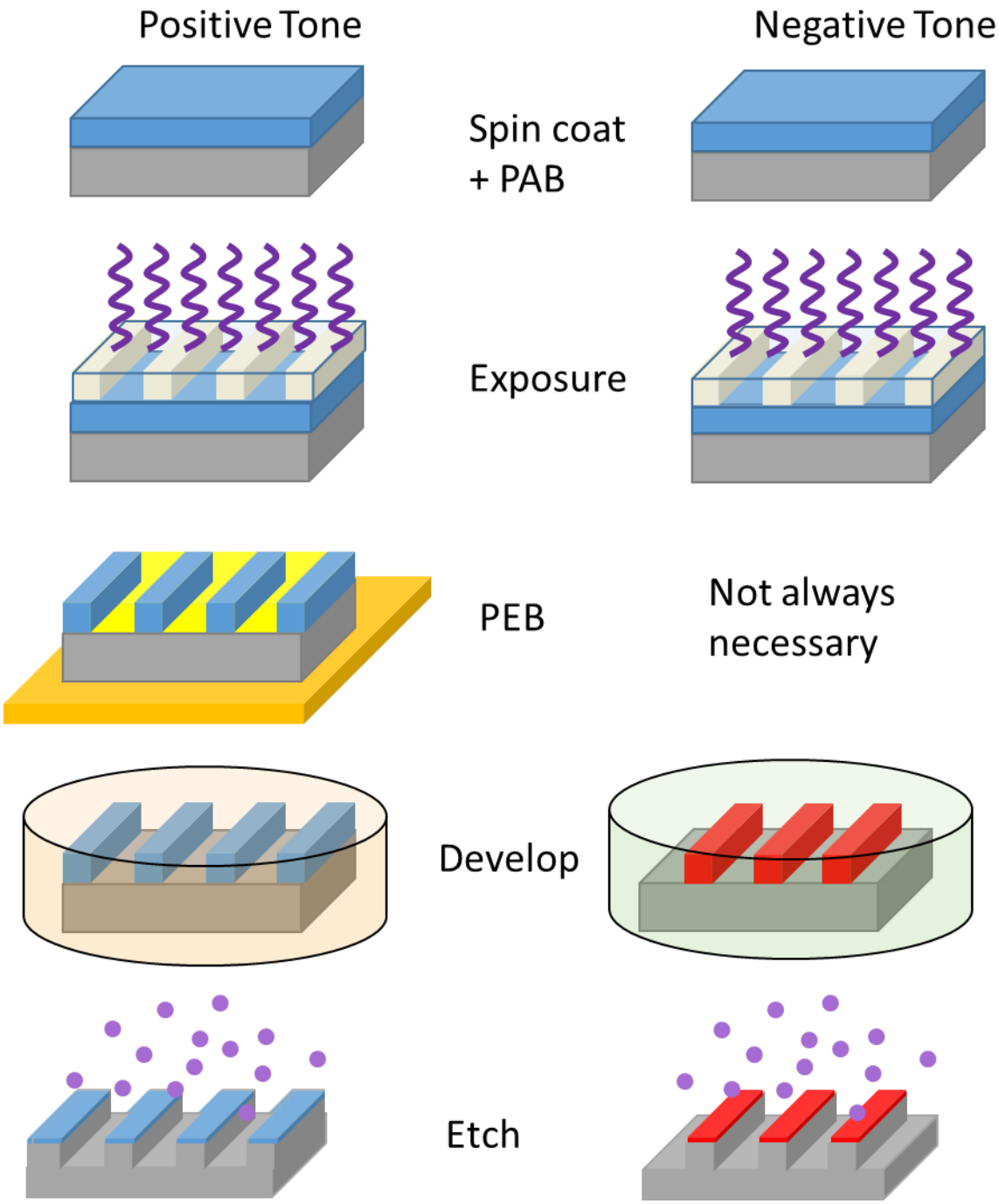

Figure 1.3 Typical lithographic processes.

Lam Research Ex. 1013 - Page 34
Lam Research Corp. v. Inpria Corp.
IPR2025-00256 - U.S. Patent No. 11,537,048

1.3.1. Chemically amplified photoresist

Photoresist material must satisfy several process attributes. First, a photoresist must explicit a chemical change leading to a solubility switch in the selective developer. Second, a photoresist must have sufficient etching selectivity especially when the film is very thin for high-resolution patterning. Third, the photoresist must be transparent to UV radiation, allowing light to pass to the bottom of the film so that PAGs throughout the film has the same absorption.

Typical model photoresists structures for 248 nm and 193 nm exposure are shown in Figure 1.4. Resists with *tert*-butyloxylcarbonate (*t*-boc) protecting groups on a polyhydroxystyrene (PHS) backbone are widely used for 248 nm exposures. However since PHS strongly absorbs at 193 nm[24], polymethylmethacrylate (PMMA) type resists, which are transparent at 193 nm, replaced PHS type resist for positive tone processes. The backbones of polymers determine the mechanical strength and glass transition temperature (T_g) of the film, while the acid labile groups are responsible for solubility change. In Figure 1.4a, *t*-boc groups protect PHS type resist and in Figure 1.4b methyladamantyl groups protect PMMA type resists. These acid labile groups can be cleaved from the backbone by protons at elevated temperatures during the PEB step. Usually the PEB temperature is around or slightly below the T_g of the photoresist.

Resist structures normally contain more than one functional group. For example, polyhydroxystyrene is not 100% protected by t-boc to adjust resist polarity in order for the

Lam Research Ex. 1013 - Page 35
Lam Research Corp. v. Inpria Corp.
IPR2025-00256 - U.S. Patent No. 11,537,048

resist to adhere to the hydrophilic Si-OH surface. Styrene monomer or methylmethacrilic lactone monomer is similarly added to increase etch resistance.[25–27]

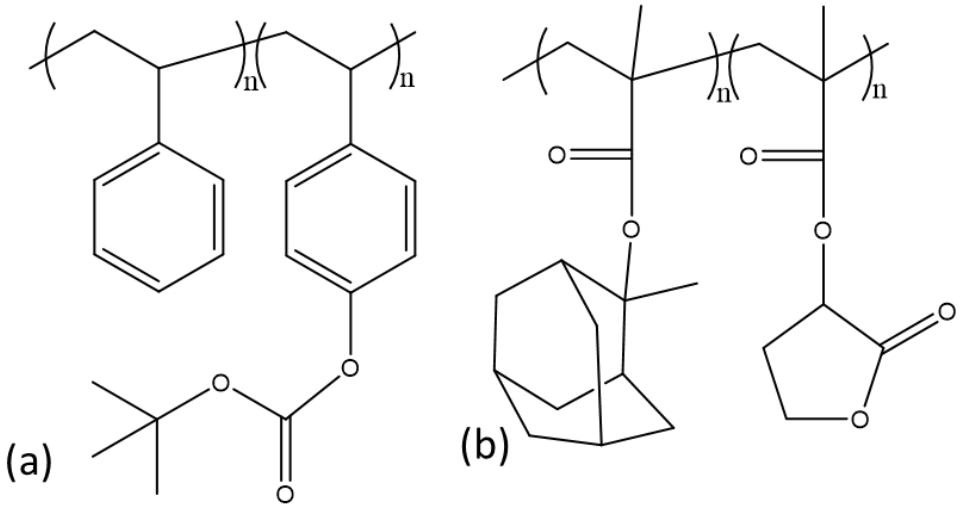

Figure 1.4 Typical photoresist structures for (a) 248 nm and (b) 193 nm lithography.

1.3.2. Photoacid generator (PAG) and acid diffusion

The selection of PAG structures must satisfy the following aspects. First, PAGs should have high absorption in the desire wavelength and be able to release protons after decomposition. Quantum yield is an important parameter to evaluate the efficiency of PAGs at the target wavelength. Second, PAGs need to be miscible with photoresist to enable uniform distribution. Finally, the thermal stability, acid strength, toxicity and outgassing are also important considerations for PAG designs.

Typical structures of PAGs are shown in Figure 1.5. PAGs absorb UV light, decompose and release a proton. During the PEB step, protons act as catalysts in the cleavage of acid labile groups from the backbone (deprotection). After each deprotection event, a proton is

Lam Research Ex. 1013 - Page 36
Lam Research Corp. v. Inpria Corp.
IPR2025-00256 - U.S. Patent No. 11,537,048

regenerated, diffuses to the next reaction site, and initiates a subsequent deprotection event. Therefore one photon generated acid can catalyze multiple deprotection events resulting in chemical amplification. After reaction, the photoresists switch from nonpolar to polar and become soluble in an aqueous base developer such as tetramethylammonium hydroxide (TMAH) solution. This chemical amplification mechanism, proposed by Ito, Willson, and Fréchet in 1982, greatly improves the sensitivity of a photoresist and has became dominant for positive tone resist.[28]

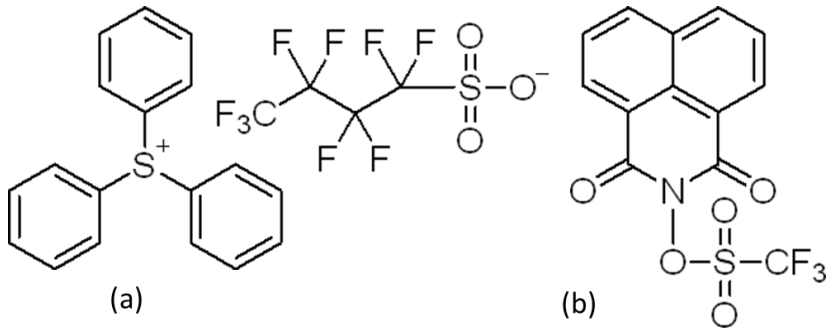

Figure 1.5 Typical (a) ionic and (b) nonionic PAG structures.

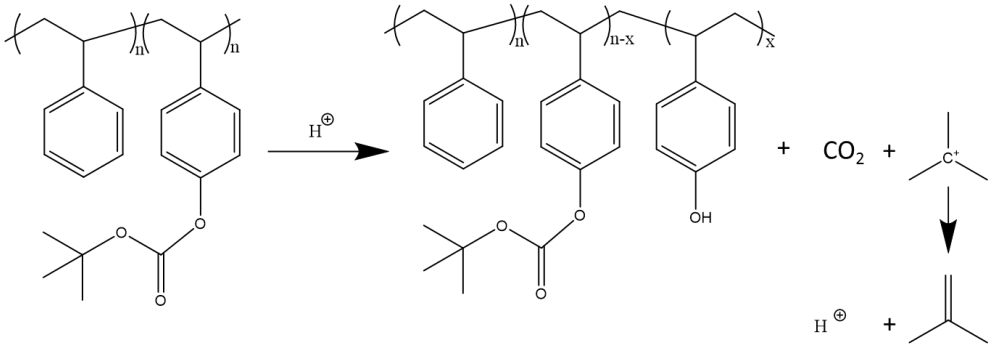

Lam Research Ex. 1013 - Page 37
Lam Research Corp. v. Inpria Corp.
IPR2025-00256 - U.S. Patent No. 11,537,048

Figure 1.6 Typical chemically amplification reaction during PEB.

PAGs can be categorized into two groups: the ionic and the non-ionic. The non-ionic PAGs are typically based on sulfone or sulfonate esters, while ionic PAGs are typically based on onium salts, such as triphenylsulfonium.[29] When the counterions contain fluorine atoms, they may become super acids. After photodecomposition of the cation in an ionic PAG (Figure 1.7), a proton is released and catalyzes reactions; fragments of cation (Figure 1.7) are not involved in deprotection but they act as plasticizers in polymeric resist films.[30]

Proton concentration as a function of exposure dose can be calculated by Dill's equation,

$$[H^+] = PAG_0 * (1 - \exp(-C * E))$$

where $[H^+]$ is the acid concentration upon exposure, PAG_0 is the initial PAG loading, C is the Dill C parameter which is determined for each different photoresist system, and E is the exposure dose. Dill C parameters for some PAGs in model resist systems have been measured. In the polyhydroxystyrene matrix, Dill C parameter of TPS-tf, TPS-nf, ND-tf are 0.045, 0.039, and 0.018 cm^2/mJ respectively. These numbers are very useful in modeling of the acid distribution and acid diffusion.

Lam Research Ex. 1013 - Page 38
Lam Research Corp. v. Inpria Corp.
IPR2025-00256 - U.S. Patent No. 11,537,048

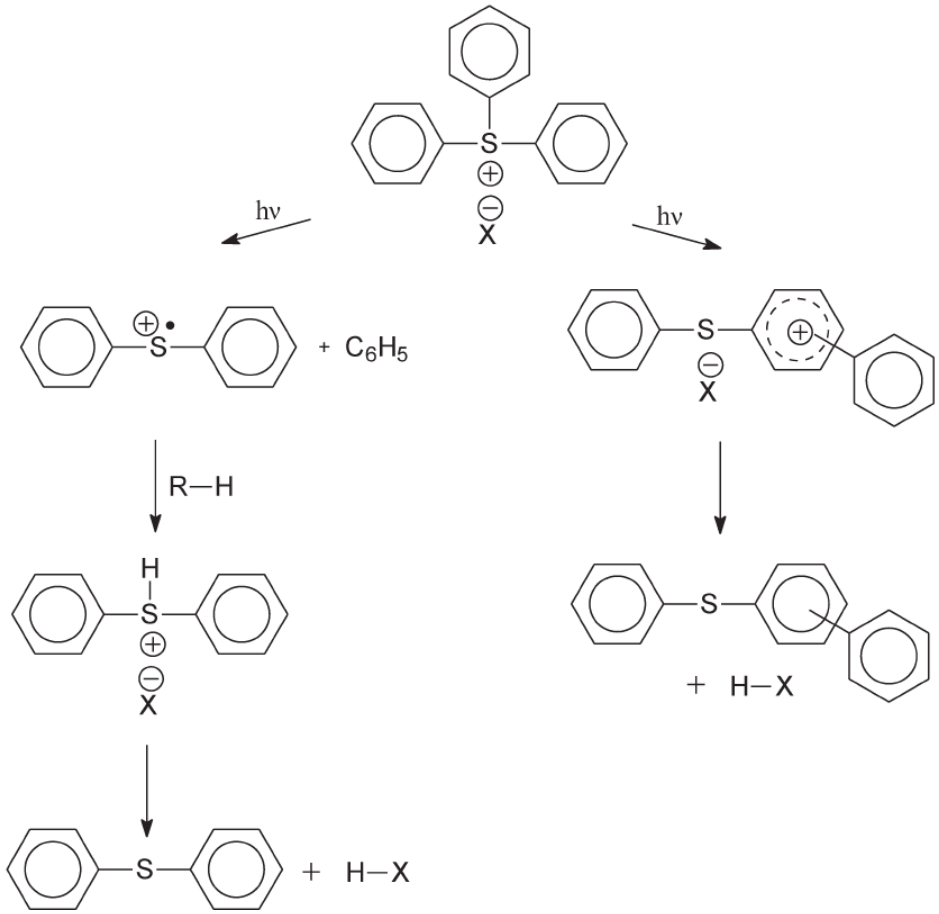

Figure 1.7 Acid generation mechanism of triphenylsulfonium salt PAGs. Reprinted with permission from ref.29. Copyright 2005 Springer.

After one deprotection event, acids are regenerated and diffuse to catalyze another deprotection, so acid diffusion is important to chemical amplification. Acid diffusion is a random walk of protons and can be quantified using Fick's Law and simplified to this equation,

$$\partial C_A / \partial t = D \nabla^2 C_A - k_3 C_A \gamma$$

Lam Research Ex. 1013 - Page 39
Lam Research Corp. v. Inpria Corp.
IPR2025-00256 - U.S. Patent No. 11,537,048

where C_A is the local acid concentration, t is time, D is the acid diffusivity in the resist matrix, k_3 is the acid quenching rate and γ is the acid quencher concentration. To simplify the system in our study, acid quenching is neglected leaving for a 1D system

$\partial C_A / \partial t = D \partial^2 C_A / \partial x^2$

The solution to this equation exhibits a characteristic diffusion length

$$L_d = \sqrt{4Dt}$$

allowing the diffusion constant to be established from measurements. This yield $D = L_d^2/4t$

where L_d is the diffusion length, and D, a function of temperature.

The acid diffusivity in resist resin can be obtained by measuring the diffusion length in a given period of time. This acid diffusion length can be obtained by using the "bilayer method" as shown in Figure 1.8.[32] The top layer is a PAG-containing resist, while the bottom layer is an equivalent resist resin with no PAG loading. The bilayers are flood exposed to UV, generating acids in the top layer. During PEB, deprotection occurs in the top layer and at the same time acids diffuse into the PAG-free bottom layer. As the acid diffuse, deprotection also occurs in the bottom layer near the interface, which leads to a thickness loss of the bottom layer after development in TMAH solution. This thickness loss of the bottom layer is quantified as the acid diffusion length which is converted to acid diffusivity. Measuring the thickness loss of a bilayer structure at different temperature, we can obtain acid diffusivity as a function of temperature.

Lam Research Ex. 1013 - Page 40
Lam Research Corp. v. Inpria Corp.
IPR2025-00256 - U.S. Patent No. 11,537,048

Excessive acid diffusion can result in line edge roughness (LER) or line width roughness (LWR). As the critical dimension of lithographic patterns shrink, LER and LWR does not scale down in the same proportion. The large value of LER or LWR compared to small line width could also potentially lead to the bridging of two lines or the opening of lines. It can affects each circuit's performance and performance uniformity between two circuits. It also cause electric leakage and affects power efficiency. Therefore for high resolution patterning, controlling the LWR of patterns is critical. Because acid diffusion is one of the main reasons for image blurring, the quantification of acid diffusion is a first step to learn the ultimate limits of LWR in a chemically amplified photoresist.

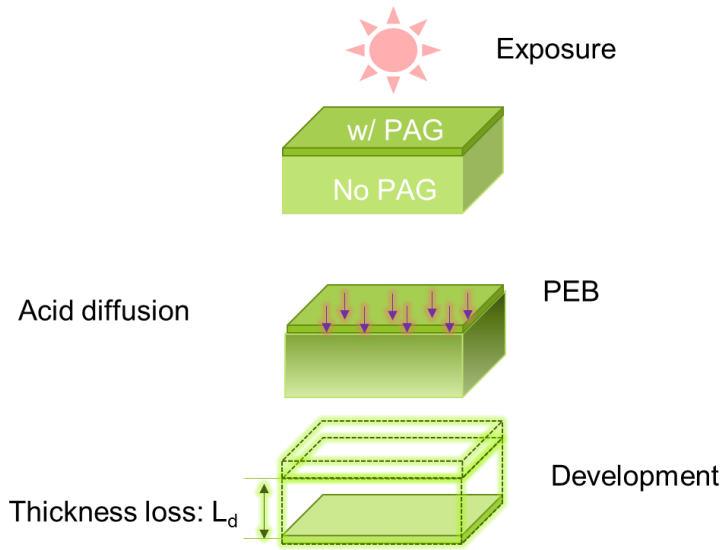

Figure 1.8 Acid diffusion length measurement by bilayer method.

Lam Research Ex. 1013 - Page 41
Lam Research Corp. v. Inpria Corp.
IPR2025-00256 - U.S. Patent No. 11,537,048

1.4. Directed self-assembly of block copolymer

1.4.1. Block copolymer

Block copolymers consist of two or more covalently bound immiscible monomer blocks in a single chain. The incompatibility of different blocks provides short range repulsive polymer-polymer interactions, which drives phase segregation into microdomains with mesoscopic length scales between 10–100nm (microphase separation). However, a macroscopic phase separation is prohibited due to the covalent bond between the blocks. The product of the repulsive polymer-polymer interaction χ and the degree of polymerization N dictates the polymer phase behavior. $\chi N << 1$ is referred as the weak segregation regime (WSL), while $\chi N >> 10$ is referred as the strong segregation regime (SSL).

In WSL, block copolymers domains are miscible. In SSL, block copolymers tend to self-assemble into various morphologies.[33,34] The simplest form of a block copolymer, linear diblock copolymer, is able to self-assemble into C (cubic), H (Hexagonal), G (gyroid) and L (lamellar) morphologies as shown in Figure 1.9.[35] The phase behavior of (A-B) block copolymers is determined by three polymer properties: N, χ and the volume fraction of the A block as shown in Figure 1.10.[36] For example, in the polystyrene-b-polyisoprene (PS-b-PI) block copolymer, the approximate volume fraction of PS for the spheres, the hexagonally-packed cylindrical morphology, the gyroid and the lamellar morphology are 0-17%, 17 – 28%, 28-34% and 34-62% respectively.[37] For the polybutadiene-block-polystyrene (PB-b-PS) block copolymer, the approximate PS volume fraction for spheres, hexagonally-packed cylindrical morphology, and lamellar phases are 0-25%, 25 – 40% and 40-60% respectively.[38]

Lam Research Ex. 1013 - Page 42
Lam Research Corp. v. Inpria Corp.
IPR2025-00256 - U.S. Patent No. 11,537,048

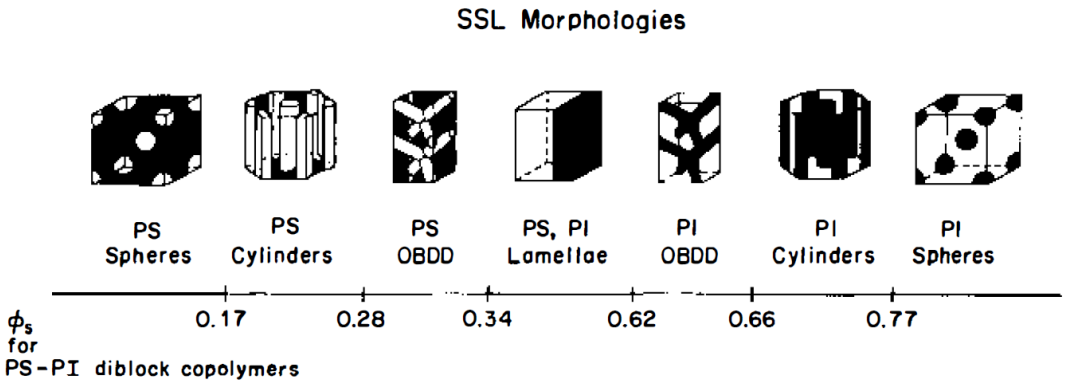

Figure 1.9 Morphologies changes as the volume fraction of polystyrene in polystyrene-polyisoprene (PS-*b*-PI) changes. Spherical, cylindrical, ordered bicontinuous double diamond and lamellar structures were found in PS-*b*-PI. Reprinted with permission from ref. 35, copyright 1990 Annual Reviews Inc.

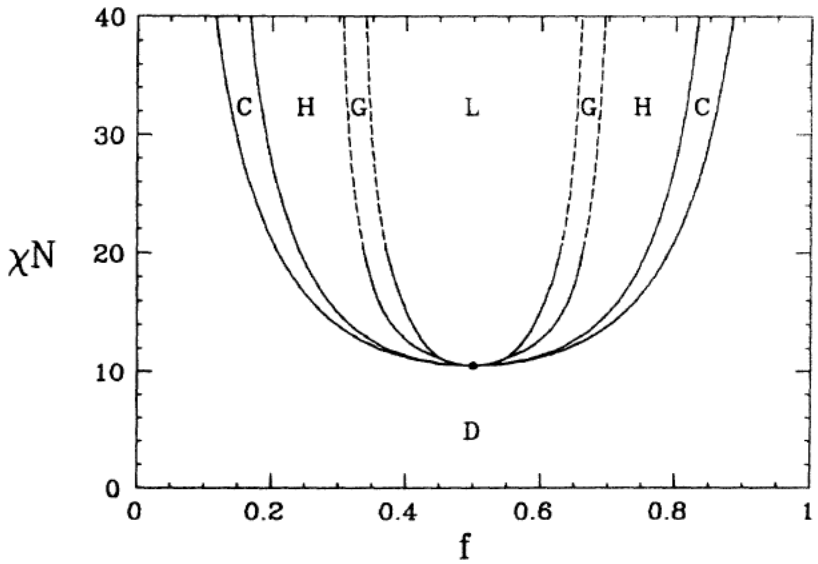

Figure 1.10 Theoretical phase diagram for diblock copolymer melts using self-consistent field theory. Phases are labeled D (disordered), C (cubic), H (hexagonal), G (gyroid) and L (lamellar). Dash lines are extrapolated phase boundaries and the dot denotes the critical point. Reprinted with permission from ref. 36, copyright 1994 American Physical Society.

Lam Research Ex. 1013 - Page 43
Lam Research Corp. v. Inpria Corp.
IPR2025-00256 - U.S. Patent No. 11,537,048

1.4.2. Thermal annealing vs. solvent annealing

Even though phase segregation is thermodynamically preferred, its kinetic rate is very slow unless the polymer chains are given sufficient mobility. Raising the temperature above the glass transition temperature (T_g) of block copolymers greatly increases the chain mobility.[39] However, the thermal decomposition set upper temperature. Nealey and coworkers studied the kinetics of thermal annealing for polystyrene-b-poly(methyl methacrylate) (PS-b-PMMA).[40] A chemically modified substrate was used to direct self-assembly during thermal annealing. The time required for each annealing temperature is plotted against 1000/K as shown in Figure 1.11. The diffusivity of block copolymers were fitted into the Arrhenius equation and the activation energy was derived from the slope of the plot. Kramer and coworkers found that by raising temperature above the order disorder transition (T_{ODT}) and slowly cooling the film to below T_{ODT}, the block copolymer grain size increased.[41] This results from the polymers mixing above T_{ODT}, removing all stubborn defects removed. Annealing at lower temperature allows for phase separation and the formation of sharp interfaces between blocks.

Other than thermal annealing, solvent vapor annealing has also been shown to increase the chain mobility. Solvents swell the film and act as plasticizers, effectively decreasing the T_g.[42,43] However, the choice of solvents can shift block copolymer's phase behavior. An order-order transition has been observed.[43] Although solvent annealing is a very effective method to anneal high T_g block copolymers, integrating solvents into a semiconductor fabrication process might pose integration and environmental concerns.

Lam Research Ex. 1013 - Page 44
Lam Research Corp. v. Inpria Corp.
IPR2025-00256 - U.S. Patent No. 11,537,048

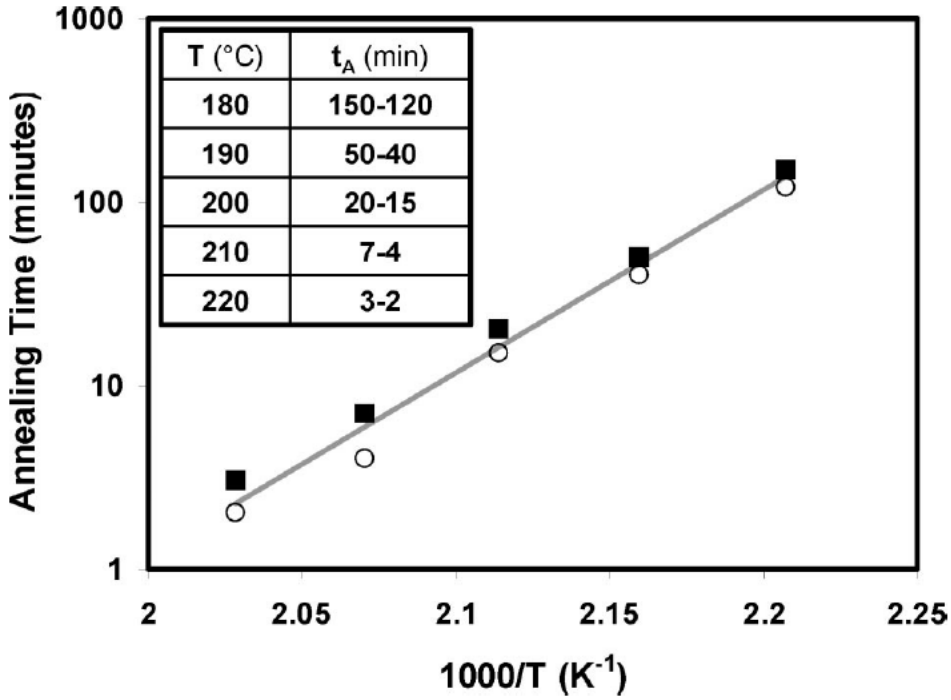

Figure 1.11 Semilog plot of annealing time as a function of inverse temperature for the minimum time observed for defect free assembly (solid square) and the maximum time for which abundant defects (open circle) still persisted. Reprinted with permission from ref.[40], copyright 1994 American Physical Society.

1.4.3. Directed self-assembly for nanopatterning

The periodicities of microdomains are proportional to $N^{2/3}\chi^{1/6}$.[38] Typical molecular weight of block copolymer range from 20 K-100 Kg/mol enabling microdomains in the range of 10-100 nanometers. Since phase separation occurs only when the product of Flory-Huggins interaction parameter (χ) and the degree of polymerization (N) is above a certain value, lower molecular weights require a higher χ. Therefore directed self-assembly (DSA) of high χ

Lam Research Ex. 1013 - Page 45
Lam Research Corp. v. Inpria Corp.
IPR2025-00256 - U.S. Patent No. 11,537,048

materials has attracted great interest as a potential candidate for a high resolution patterning.[44–46]

The χ parameter also affects the polymer-polymer interfacial width Δ.[39] If block copolymers are used for lithographic patterns formation, Δ affects the LER of patterns after selectively removal of one block by etching. The interfacial width is given by,

$$\Delta_\infty = \frac{2a}{\sqrt{6\chi}}$$

$$\Delta = \Delta_\infty[1 + \ln 2(\frac{1}{\chi N_A} + \frac{1}{\chi N_B})]$$

where Δ is the interfacial width, a is the statistical monomer segment length, and N_A and N_B are the numbers of molecules in each block. Higher χ leads to smaller Δ, thus smaller LWR.

As block copolymers self-assemble into various morphologies, they provide many possibilities to convert these dense repetitive structures to complex lithographic patterns such as jogs, T-junctions or blends. This can be achieved by using template patterns with appropriate periodicity and arrangement as shown in Figure 1.12.[47–49]

Controlling the surface energy of substrates or adding a topcoat to avoid polymer-air interface formation can change the orientation of ordered morphologies. Symmetric PS-b-PMMA tends to form parallel lamellar structures on bare SiO_2 surface, as PMMA preferentially wets SiO_2 to balance the surface energy and interfacial tension. Therefore, in order to achieve perpendicular lamellae, controlling the neutrality of the surface to both blocks is necessary.[50] Grafting random copolymers to surface is one option.[51] However, the use of random

Lam Research Ex. 1013 - Page 46
Lam Research Corp. v. Inpria Corp.
IPR2025-00256 - U.S. Patent No. 11,537,048

copolymers does not always ensures perpendicular lamellae alignment.[52,53] The high χ of PS-PDMS results in $\Delta\gamma_{Top} >> 0$ with air, which inevitably drives the orientation of surface domain parallel to the substrate.[54] Even in the presence of neutral substrate surface treatments, they cannot be aligned perpendicularly by thermal annealing alone. Hence, a top coat from aqueous solution that is neutral to both block sandwich block copolymers is required to change the orientation of lamellae.[53]

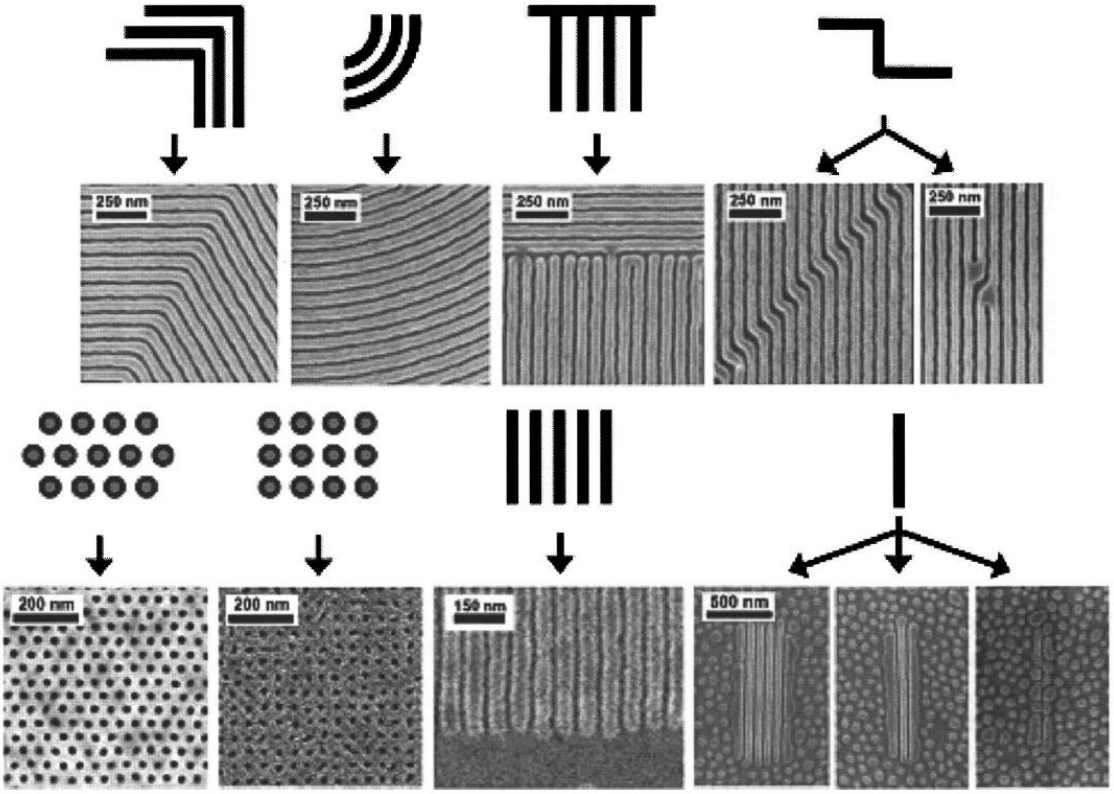

Figure 1.12 Common IC patterns that are self-assembled by block copolymers. Reprinted with permission from ref.48, copyright 2007 American Institute of Physics.

Lam Research Ex. 1013 - Page 47
Lam Research Corp. v. Inpria Corp.
IPR2025-00256 - U.S. Patent No. 11,537,048

Although using thermal or solvent vapor annealing can help phase separation, it is hard to reach equilibrium or long range order by simply using these methods. In order to achieve long range order, some tricks must be employed together with annealing. Graphoepitaxy,[55–58] chemoepitaxy,[59–61] shear force,[62–64] electric field [65–68] or magnetic field [69,70] are used as secondary method to help drive long range ordering.

Graphoepitaxy makes use the confinement effects by creating a topography on the substrates. For the example, C.T Black and colleagues[71] used a tapered trench to align perpendicular lamellae since narrow trenches imposes higher free-energy penalty for defect formation than wider trenches (Figure 1.13).

Defects are hard to remove especially from cylindrical structures. However, with graphoepitaxy and thermal annealing, perfect alignment of monolayer cylinders can be achieved. As shown in Figure 1.14, using thermal annealing with graphoepitaxy, cylinders start to align first along the side walls as time passes, the size of ordered domain continues to increase. After 33 hour, perfect alignment was finally achieved, while finger prints patterns still persists on planar substrate under the equivalent annealing condition.[58]

Lam Research Ex. 1013 - Page 48
Lam Research Corp. v. Inpria Corp.
IPR2025-00256 - U.S. Patent No. 11,537,048

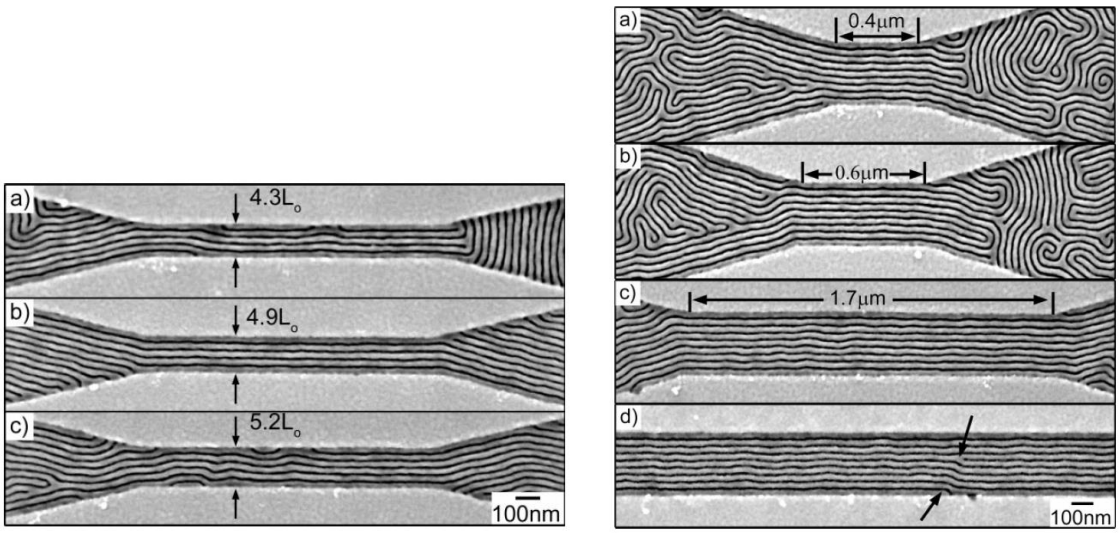

Figure 1.13 Graphoepitaxy makes uses of confinement effects. ref.71, copyright 2007 American Chemical Society.

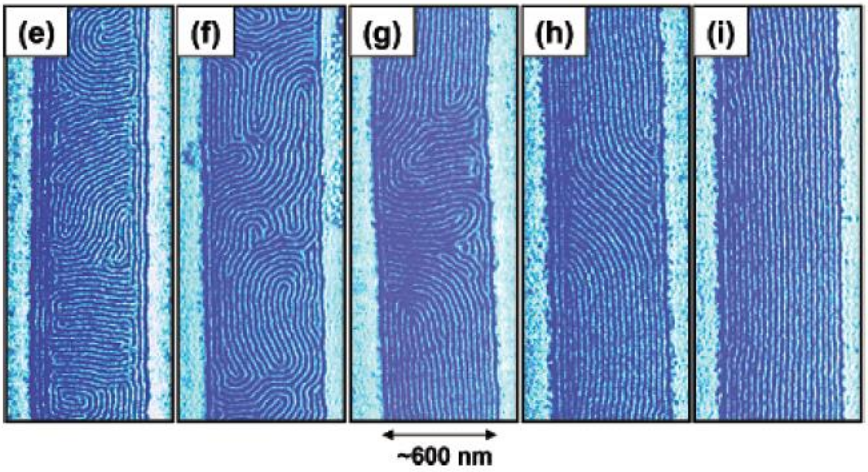

Figure 1.14 Alignment mechanism. Lines begins to locate from the edge to the whole trench width (e) 9 h, (f) 14 h, (g) 19 h, (h) 24 h, and (i) 33h at 130 °C. Reprinted with permission from ref.58, copyright 2004 American Chemical Society.

Lam Research Ex. 1013 - Page 49
Lam Research Corp. v. Inpria Corp.
IPR2025-00256 - U.S. Patent No. 11,537,048

1.5. EUV lithography

1.5.1. EUV scanner and mask

During the past few decades, the wavelength for lithography has evolved for several generations from 436 nm in the 1970's to 193 nm in the 2010's. According to Rayleigh's equation, the minimum resolution is proportional to the wavelength. As a results, reduction in the exposure wavelength gave rise to the reduction in the critical dimension of microelectronic devices. Extreme ultraviolet lithography (EUVL), with a wavelength of 13.5 nm, theoretically has great potential to extend resolution of optical lithography. Therefore the official hope for the industry to continue "Moore's law" is EUVL despite many challenges that need to be overcome.[4,7,23,72–74]

EUV light can be generated from different sources such as a synchrotron or gas plasma. A commercial EUV scanner uses a CO_2 laser at 10.6 μm wavelength beam and this beam is used to excite tin drops into charged plasma. Electrons in this positively charged plasma emit bursts of broadband EUV radiation. This broadband EUV radiation is then collected and filtered by a high-reflectivity ellipsoidal molybdenum–silicon multilayer mirror to output the 13.5 nm wavelength as shown in Figure 1.15.

Lam Research Ex. 1013 - Page 50
Lam Research Corp. v. Inpria Corp.
IPR2025-00256 - U.S. Patent No. 11,537,048

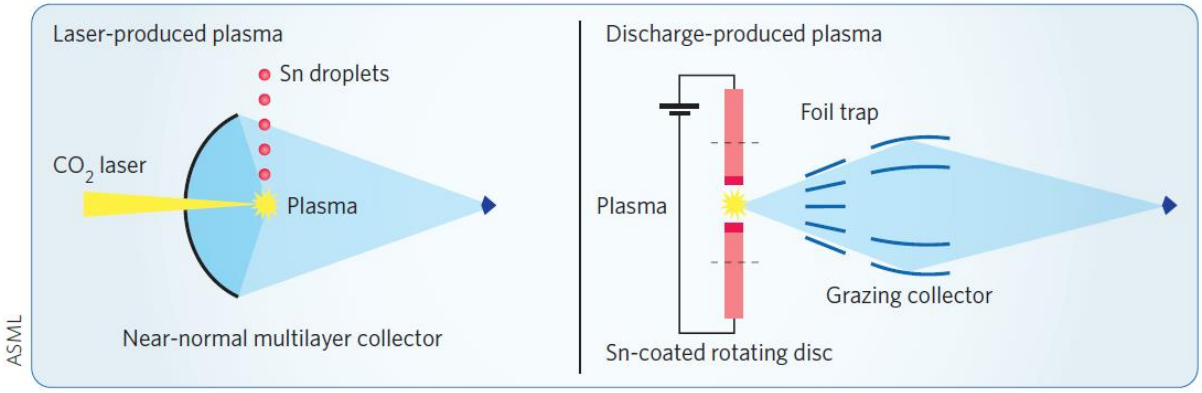

Figure 1.15 EUV radiation generation mechanism. Reprinted with permission from ref.6, copyright 2010 Macmillan Publishers Limited.

EUV light at 13.5 nm is highly absorbed by all matter including air. As a consequence, reflective instead of refractive optics and mirrors must be used throughout entire optical pathway has to be in near-vacuum. Since only reflective mirror can be used, the materials and design of the mask is very different from conventional lithography.

1.5.2. EUVL resist

Each EUV scanner and associated mask have a high cost of ownership, thus EUVL will not be brought into manufacturing unless EUVL can improve current throughput and the minimum resolution of a resist can achieved. Although EUVL was initially planned to be ready for manufacturing in 2010 for the 22 nm node, EUV light source and tool integration

Lam Research Ex. 1013 - Page 51
Lam Research Corp. v. Inpria Corp.
IPR2025-00256 - U.S. Patent No. 11,537,048

issues prevented adoption. Integration of EUVL into high volume manufacturing (HVM) has been delayed and is now expected to be used at the "7 nm node" in 2017.[23]

High sensitivity, high resolution and low edge roughness (LER) are required for EUV resists. Currently, there are three main types of resist platforms: chemically amplified resist (CAR) [77–80], metal sulfonium resist (HfSOX) [81–84] and ligands stabilized metal oxide nanoparticle resist[85–94].

The patterning mechanism of chemically amplified resist is well understood and its process is mature. However, there are many challenges for CAR including pattern collapse[95] and excessive acid diffusion still remain challenges for EUVL.[96,97] Additional challenges for EUV includes secondary electrons which are generated when EUV hits the film. Resist materials is ionized by EUV, generating photoelectrons and secondary electrons.[98,99] Secondary electrons bounce around in the film and cause reactions randomly superimposed to the intended aerial patterns. Furthermore, thermal effects of EUV radiation may cause the decomposition of PAG which adds to image blur.[100] All these effects contributes to high LWR below 20nm. Unless LWR can be lowered, resolutions below 14 nm HP cannot be achieved. Other challenges for CAR include poor sensitivity due to film absorption of EUV radiation and inadequate etch resistance of thin organic film.[101–103]

Metal sulfonium resist were first developed by Oregon State University. $HfOCl_2$, H_2SO_4 and H_2O_2 water solution are directly spun cast onto a HDMS primed wafer, followed by post apply bake (PAB) at 80 °C for 3 mins. After EUV exposure in near-vacuum, films were subjected to a PEB at 80 °C. Developed in 25% tetramethyl ammonium hydroxide (TMAH) solution, negative-tone patterning was obtained.[84] This resist platform has shown

Lam Research Ex. 1013 - Page 52
Lam Research Corp. v. Inpria Corp.
IPR2025-00256 - U.S. Patent No. 11,537,048

extraordinary resolution and low roughness. However, the tradeoff is sensitivity. Their best images show 12 nm half pitch line space patterns with 4.4 nm LWR at a e-beam dose of 163 mJ/cm^2.[104] This dose is at least 10 times higher than the sensitivity required for EUVL resist. Despite the good patterning ability demonstrated, the sensitivity is far from satisfactory. The dose is so high that line width roughness caused by out of band radiation (OOB) and shot noise is not significant under these conditions. If the dose of this type of resist can be reduced to less 10 mJ/cm^2, then the effects of OOB and short noise would become non-negligible. Furthermore, this low sensitivity is due to the photoreaction mechanism. EUV exposure induces decomposition of the peroxide species to produce water and O_2 gas while catalyzing polymerization.[105] Because of high energy required for peroxide decomposition, it may be difficult to reduce the dose to a the required values.

Ligands stabilized metal oxide nanoparticle resists, developed by Ober *et al.* at Cornell University have shown the highest EUV sensitivity to date.[86,88] These resists consist of metal oxide cores, such as hafnium oxide or zirconium oxide, with carboxylic acid ligands to stabilize the nanoparticles, such as methacrylic acid and benzoic acid. The nanoparticles sizes are less than 5 nm and can be dispersed in common spin coating solvents such as propylene glycol monomethyl ether acetate (PGMEA). They are formulated with PAGs, although patterning is through a non-chemical amplification mechanism. PAGs are responsible for generating anions as stronger ligands to replace initial ligands. These ligands exchange cause particle condensation and the solubility switch. Exposed resists become insoluble in organic developer and negative tone patterns down to 18 nm have been demonstrated. Hafnium oxide nanoparticles with methacrylic acid ligands can form 22 nm patterns with EUV exposure dose of only 4.2 mJ/cm^2.[86] Due to the high sensitivity of this EUV resist system, it is a potential

Lam Research Ex. 1013 - Page 53
Lam Research Corp. v. Inpria Corp.
IPR2025-00256 - U.S. Patent No. 11,537,048

EUV resist for manufacturing. Furthermore, below the 22 nm node, resist films are very thin and it is hard to provide enough etch resistance during pattern transfer. The metal content in these nanoparticle resists give them an extra benefit of high etch resistance.

However, the resolution and LWR still need to be further improved. This requires a clearer understanding of the patterning mechanism and the source of LWR, especially from a material perspective. In this thesis, patterning mechanism is further investigated and the structure-property relationship of ligands and resist performance were studied. We believe the ligands stabilized metal oxide nanoparticles are very promising for their high sensitivity, high resolution, high etch resistance and process compatibility with previous CAR systems.

1.6. Laser Spike Annealing

1.6.1. Shallow Junction Annealing and Diffusion Control

The fabrication of p-n junction for a MOS devices require ion implantation for dopant introduction. Thermal annealing process is typically required after ion implantation to heal lattice damage and remove defects that caused by the high energetic ions during implantation.[106] However, due to the presence of these defects, enhanced dopant diffusion is observed which extend dopant boundaries.[107] In shallow junctions below 20 nm, this diffusion could short circuit the source and the drain. Rapid thermal annealing (RTA) was introduced to control dopant diffusion during thermal annealing. [108]A.E Michel and colleagues showed that this anomalous diffusion was reduced by annealing for short times at high temperatures.[109]

Lam Research Ex. 1013 - Page 54
Lam Research Corp. v. Inpria Corp.
IPR2025-00256 - U.S. Patent No. 11,537,048

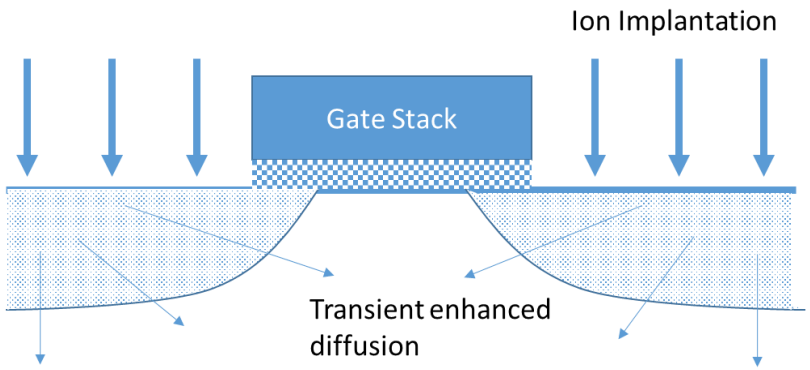

Figure 1.16 Gate structure of a CMOS device. Dopant diffusion into the channel during thermal annealing after ion implantation limits the channel length.

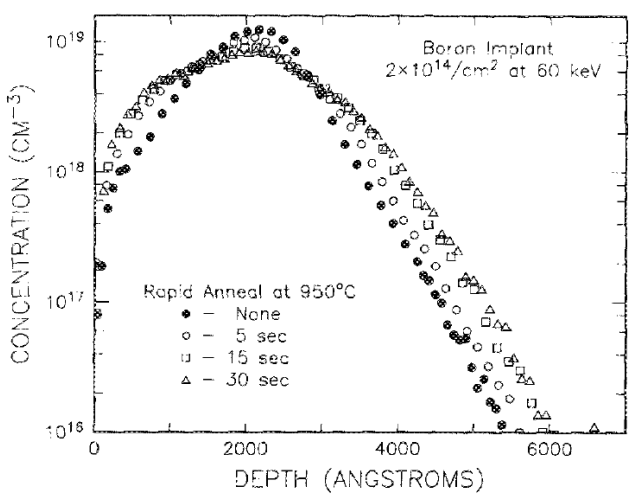

Figure 1.17 Dopant concentration near the surface under different annealing conditions. Dopant diffusion length decrease as the annealing time decrease. Reprinted from ref.109, copyright 1987 American institute of Physics.

To achieve even shorter annealing times, direct surface annealing, or laser spike annealing (LSA) was developed for shallow junction annealing. Both techniques use high power

Lam Research Ex. 1013 - Page 55
Lam Research Corp. v. Inpria Corp.
IPR2025-00256 - U.S. Patent No. 11,537,048

continuous wave (CW) lasers to achieve a high temperature ramp. Initially directed surface annealing uses a diode laser (λ = 810 nm) [110], while laser spike annealing used a CO_2 gas laser (λ= 10.6 μm).[111,112] Depending on beam width and scan velocity, dwell time (τ) ranges from 10μs to 10ms can be achieved, where the dwell time is defined as the ratio of the beam width and the velocity and is a metrics of the heating time.

1.6.2. Laser spike annealing of organic systems

The idea of utilizing lasers to treat organic systems has been around for decades[113,114], but during the 1990s and 2000s only pulsed laser in the femtosecond or nanosecond pulse laser were extensively explored. Utilizing continuous-wave lasers as an alternative heat source to treat organic systems was revisited initiated by a collaboration of Thompson and Ober in 2009, used first as an alternative PEB method for positive tone chemically amplified photoresist.[115–121] This work first showed that those fragile organic molecules, such as photoresist and photoacid generator which usually decomposed at 200 °C, were thermally stable during laser annealing to temperatures above 500 °C. Jung *et al*. demonstrated that different types of polymer (e.g. photoresist, Si containing block copolymers and conjugated polymers) all showed higher thermal decomposition temperature during millisecond laser annealing (Figure 1.18). Almost independent of polymer, the thermal decomposition temperature are approach 1000 °C for 500 μs annealing.[122] The extension in thermal stability during laser annealing provides a broader temperature window for materials chemistry and physics studies. During high temperature and short time laser heating, the reaction and diffusion kinetics can be different from conventional hot plate heating.[119] In one study, it was shown the byproduct formation during PEB a different reaction path that altered the order of reaction.[115] This

Lam Research Ex. 1013 - Page 56
Lam Research Corp. v. Inpria Corp.
IPR2025-00256 - U.S. Patent No. 11,537,048

research provides a foundation for applying rapid laser heating to different systems that will be discussed later in this thesis.

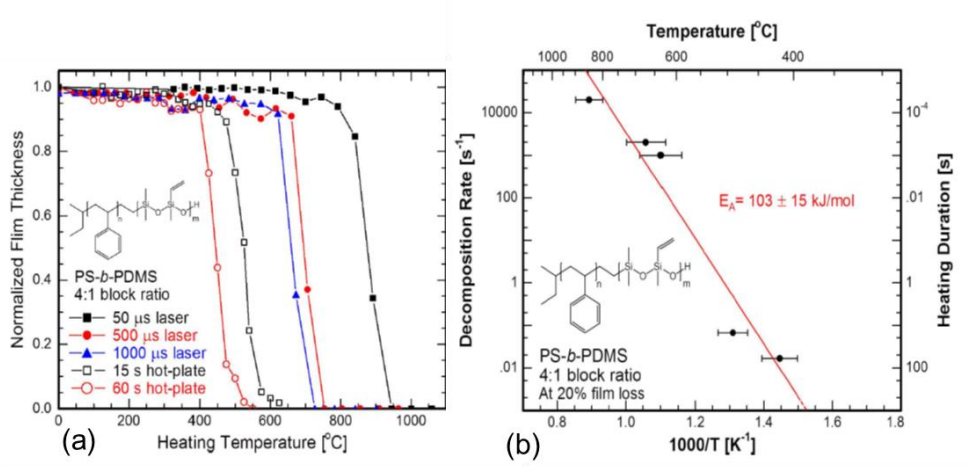

Figure 1.18 Thermal stability of PS-b-PDMS. a) thickness decrease as a function of increasing temperature for various dwell time. The shorter dwell time, the high temperature that a polymer can withstand transiently increase transiently. b) decomposition rate of PS-b-PDMS as a function of temperature during laser annealing in an Arrhenius plot and the slope is the thermolysis activation energy. Reprinted from ref.[122] copyright © 2014 Byungki Jung.

Table 1.1 Summary of various polymer thermal decomposition temperature for a 60 s hot plate heating and laser annealing for 50 μs. Reprinted from ref.122 copyright © 2014 Byungki Jung.

Polymer	T_{limit} 60 s	T_{limit} 50 μs	$\Delta T^{20\,\%\text{ film loss}}_{60\text{ s vs. }50\,\mu s}$	$E_A^{decomposition}$
MEH-PPV	550 °C	1000 °C	~510 °C	71 ± 4 kJ/mol
PS-*b*-PDMS (4:1)	550 °C	940 °C	~430 °C	103 ± 15 kJ/mol
PS-*b*-PDMS (16:13)	550 °C	940 °C	~425 °C	107 ± 19 kJ/mol
PEDOT:PSS	475 °C	~1050 °C	~420 °C	86 ± 9 kJ/mol

Lam Research Ex. 1013 - Page 57
Lam Research Corp. v. Inpria Corp.
IPR2025-00256 - U.S. Patent No. 11,537,048

The extension of thermal decomposition temperature and the thermal decomposition activation energy was also summarized in Table 1.1. Temperature processing windows are enhanced by leaser heating and the limiting temperature can be predicted using the activation energy.

1.6.3. Cornell laser system and temperature calibration

In this thesis, two CW laser were used in a benchtop LSA system. One was CO_2 laser (λ=10.6 μm) and the other a diode laser (λ=980 nm). These lasers shared a common substrate holders, moving stage, and stage control as shown in Figure 1.19.

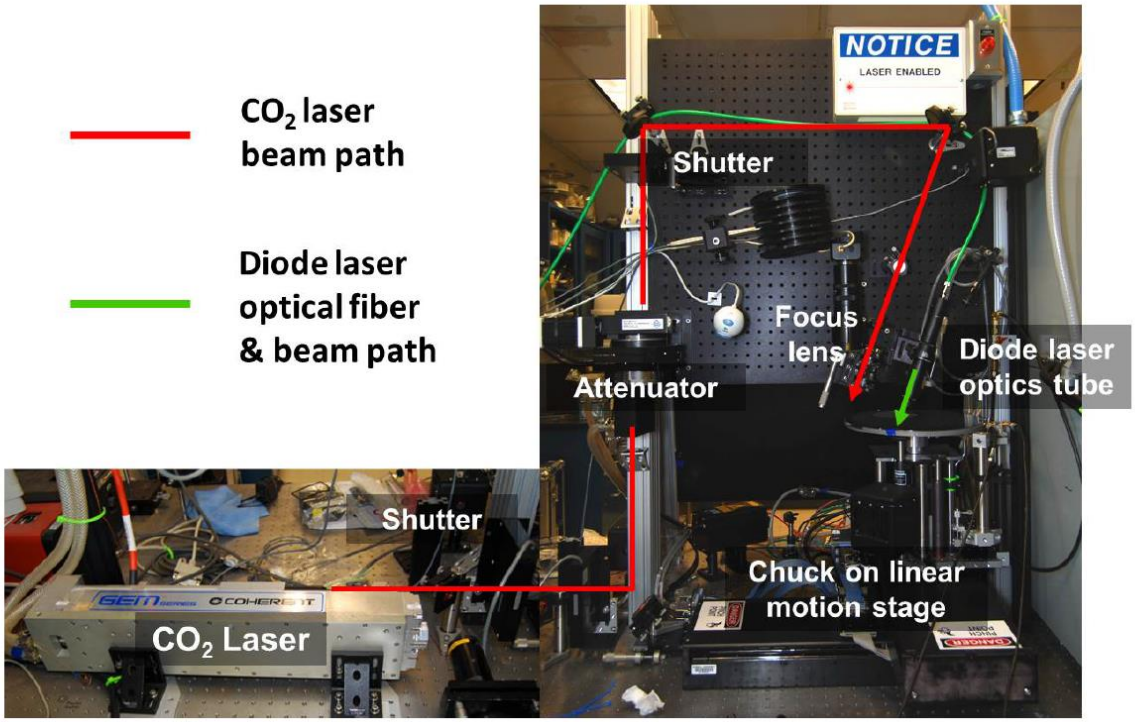

Figure 1.19 Cornell laser systems: diode laser and CO_2 laser. Reprinted from ref.121 copyright © 2014 Byungki Jung.

Lam Research Ex. 1013 - Page 58
Lam Research Corp. v. Inpria Corp.
IPR2025-00256 - U.S. Patent No. 11,537,048

For the CO_2 laser, the power is controlled using attenuator allowing energy control to 1% levels. The laser diode is controlled by changing the drive current. Both laser are shaped optically to a line beam. The dwell time is determined by the scanning velocity, and the moving stage is capable of both rotational and horizontal movement. The intensity profile of the CO_2 laser is nearly Gaussian with slightly asymmetry (Figure 1.20a). The full width at half maximum (FWHM) of long axis is 590 μm with a short axis the FWHM 90 μm. As CO_2 laser wavelength (10.6 μm) is not be directed absorbed by pure Si, a heavily p-doped Si wafer (0.02-0.05 Ω resistance) were used to introduce free carrier absorption.

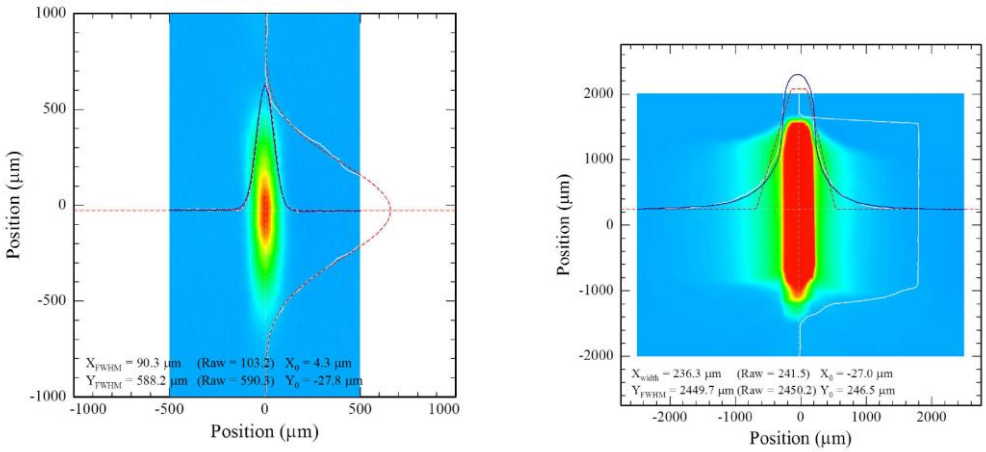

Figure 1.20 Incident laser intensity profile at the sample of a) the CO_2 laser and b) the diode laser.

The diode laser is fiber coupled into a plate quartz homogenizer and focused using cylindrical lenses to a near flat-top profile (Figure 1.20b). The intensity profile of diode laser shown in Figure 1.21b. Unlike the CO_2 laser, the long axis of diode laser is nearly flat (FWHM =2450

Lam Research Ex. 1013 - Page 59
Lam Research Corp. v. Inpria Corp.
IPR2025-00256 - U.S. Patent No. 11,537,048

μm) and the short axis still has a Gaussian profile (FWHM=240 μm). At 980 nm, diode laser is absorbed directly absorbed by Si wafers with normal doping (10-20 Ω resistance).

During laser annealing, the stage for substrate holder is moved at a constant rate, so the annealing time is defined as the ratio of beam width in the scanning direction to the scan velocity. For CO_2 laser with a beam with of 40 μm, the dwell times in the range of 50 μs-10 ms can be achieved. For the diode laser with a beam width of 240 μm, the dwell time is typically in the range of 1 ms-20 ms. Under these conditions, the laser induced heating can reach temperature ramp of 10^4-10^5 K/s, while for a conventional PEB, the substrate is heated at ~100 K/s. Laser temperature calibration will be discussed later in the thesis.

Reference

(1) Moore, G. E. Cramming More Components onto Integrated Circuits. *Proc. IEEE* 1998, *86*, 82–85.

(2) Reichmanis, E.; Houlihan, F. M.; Nalamasu, O.; Neenan, T. X.; Laboratories, T. B.; Hill, M. Chemical Amplification Mechanisms for Microlithography. 1994.

(3) Pimpin, A.; Srituravanich, W. Reviews on Micro- and Nanolithography Techniques and Their Applications. *Engineering Journal*, 2012, *16*, 37–55.

(4) Ito, T.; Okazaki, S. Pushing the Limits of Lithography. *Nature* 2000, *406*, 1027–1031.

(5) Wallraff, G. M. Single-Layer Chemically Amplified Photoresists for 193-Nm Lithography. *J. Vac. Sci. Technol. B Microelectron. Nanom. Struct.* 1993, *11*, 2783.

(6) Wagner, C.; Harned, N. EUV Lithography: Lithography Gets Extreme. *Nature Photonics* 2010, *4*, 26.

(7) Wu, B.; Kumar, A. Extreme Ultraviolet Lithography: A Review. *Journal of Vacuum Science & Technology B: Microelectronics and Nanometer Structures*, 2007, *25*, 1743.

(8) Guo, L. J. Nanoimprint Lithography: Methods and Material Requirements. *Adv. Mater.* 2007, *19*, 495–513.

Lam Research Ex. 1013 - Page 60
Lam Research Corp. v. Inpria Corp.
IPR2025-00256 - U.S. Patent No. 11,537,048

(9) Sotomayor Torres, C. M.; Zankovych, S.; Seekamp, J.; Kam, A. P.; Clavijo Cedeño, C.; Hoffmann, T.; Ahopelto, J.; Reuther, F.; Pfeiffer, K.; Bleidiessel, G.; *et al.* Nanoimprint Lithography: An Alternative Nanofabrication Approach. *Materials Science and Engineering: C*, 2003, *23*, 23–31.

(10) Chou, S. Y.; Krauss, P. R.; Renstrom, P. J. Nanoimprint Lithography. *J. Vac. Sci. Technol. B Microelectron. Nanom. Struct.* 1996, *14*, 4129.

(11) Xia, Y.; Whitesides, G. M. Soft Lithography. *Annual Review of Materials Science*, 1998, *28*, 153–184.

(12) Broers, A. N.; Hoole Andrew C.F, A. C. F.; Ryan, J. M. Electron Beam Lithography - Resolution Limits. *Microelectron. Eng.* 1996, *32*, 131–142.

(13) Chang, T. H. P.; Mankos, M.; Lee, K. Y.; Muray, L. P. Multiple Electron-Beam Lithography. *Microelectronic Engineering*, 2001, *57-58*, 117–135.

(14) Ross, C. B.; Sun, L.; Crooks, R. M. Scanning Probe Lithography . Scanning Tunneling Microscope Induced Lithography of Self-Assembled N-Alkanethiol Monolayer Resists. *Langmuir* 1993, *9*, 632–636.

(15) Nyamjav, D. Scanning Probe Lithography. *Proc. SPIE* 2003, *5037*, 162–167.

(16) Watt, F.; Bettiol, A. A.; Van Kan, J. A.; Teo, E. J.; Breese, M. B. H. Ion beam lithography and nanofabrication: a review. *International Journal of Nanoscience*, 2005, *04*, 269–286.

(17) Melngailis, J. Focused Ion Beam Lithography. *Nuclear Instruments and Methods in Physics Research Section B: Beam Interactions with Materials and Atoms*, 1993, *80-81*, 1271–1280.

(18) Tang, C.; Lennon, E. M.; Fredrickson, G. H.; Kramer, E. J.; Hawker, C. J. Evolution of Block Copolymer Lithography to Highly Ordered Square Arrays. *Science* 2008, *322*, 429–432.

(19) Bates, C. M.; Maher, M. J.; Janes, D. W.; Ellison, C. J.; Willson, C. G. Block Copolymer Lithography. *Macromolecules*, 2014, *47*, 2–12.

(20) Bratton, D.; Yang, D.; Dai, J.; Ober, C. K. Recent Progress in High Resolution Lithography. *Polymers for Advanced Technologies*, 2006, *17*, 94–103.

(21) Lin, B. J. The K[sub 3] Coefficient in Nonparaxial λ/NA Scaling Equations for Resolution, Depth of Focus, and Immersion Lithography. *Journal of Microlithography, Microfabrication, and Microsystems*, 2002, *1*, 7.

Lam Research Ex. 1013 - Page 61
Lam Research Corp. v. Inpria Corp.
IPR2025-00256 - U.S. Patent No. 11,537,048

(22) Owa, S.; Nagasaka, H. Immersion Lithography; Its Potential Performance and Issues. In *OPTICAL MICROLITHOGRAPHY XVI, PTS 1-3*; 2003; Vol. 5040, pp. 724–733.

(23) International Technology Roadmap for Semiconductors, 2013 Edition, Lithography. *ITRS*; San Jose,CA, 2014.

(24) Amplification, C. Alicyclic Polymer for ArF and KrF Excimer Resist Based on. 1992, *1672*, 66–73.

(25) Ito, H.; Breyta, G.; Hofer, D.; Sooriyakumaran, R.; Petrillo, K.; Seeger, D. Environmental Stable Chemical Amplification Positive Resist: Principle, Chemistry, Contamination Resistance, and Lithographic Feasibility. *J. Photopolym. Sci. Technol.* 1994, *7*, 433–447.

(26) Takechi, S.; Takahashi, M.; Kotachi, A.; Nozaki, K.; Yano, E.; Hanyu, I. Impact of 2-Methyl-2-Adamantyl Group Used for 193-Nm Single-Layer Resist. *J. Photopolym. Sci. Technol.* 1996, *9*, 475–488.

(27) Ito, H.; Truong, H. D.; Brock, P. J. Lactones in 193 Nm Resists: What Do They Do? 2008, *6923*, 12.

(28) Ito, H.; Grant Willson, C.; Frechet, J. H. J. New UV Resists with Negative or Positive Tone. *Digest of Technical Papers. Symposium on VLSI Technology*, 1982, 86–87.

(29) Ito, H. *Chemical Amplification Resists for Microlithography*. 2005, *172*, 245.

(30) McKean, D. R.; Schaedeli, U.; MacDonald, S. a. Acid Photogeneration from Sulfonium Salts in Solid Polymer Matrices. *J. Polym. Sci. Part A Polym. Chem.* 1989, *27*, 3927–3935.

(31) Sha, J.; Lee, J.-K.; Kang, S.; Prabhu, V. M.; Soles, C. L.; Bonnesen, P. V.; Ober, C. K. Architectural Effects on Acid Reaction-Diffusion Kinetics in Molecular Glass Photoresists. *Chem. Mater.* 2010, *22*, 3093–3098.

(32) Leibler, L. Theory of Microphase Separation in Block Copolymers. *Macromolecules* 1980, *13*, 1602–1617.

(33) Chu, H. Morphologies of Strongly Segregated Diblock Copolymers. 1995, *36*, 1569–1575.

(34) Bates, F. S.; Fredrickson, G. H. Block Copolymer Thermodynamics: Theory and Experiment. *Annu. Rev. Phys. Chem.* 1990, *41*, 525–557.

(35) Matsen, M.; Schick, M. Stable and Unstable Phases of a Diblock Copolymer Melt. *Physical Review Letters*, 1994, *72*, 2660–2663.

Lam Research Ex. 1013 - Page 62
Lam Research Corp. v. Inpria Corp.
IPR2025-00256 - U.S. Patent No. 11,537,048

(36) Kim, J. K. Volume Fraction on the Order-Disorder Transition in Low Molecular Weight Polystyrene-bZock-Polyisoprene Copolymers. 1. Order-Disorder Transition Temperature Determined by Rheological Measurements. *Transition* 1995, 5043–5062.

(37) Ohta, T.; Kawasaki, K. Equilibrium Morphology of Block Copolymer Melts. *Macromolecules* 1986, *19*, 2621–2632.

(38) Yokoyama, H. Diffusion of Block Copolymers. *Mater. Sci. Eng. R Reports* 2006, *53*, 199–248.

(39) Welander, A. M.; Kang, H.; Stuen, K. O.; Solak, H. H.; Müller, M.; de Pablo, J. J.; Nealey, P. F.; Pablo, J. J. De; Nealey, P. F. Rapid Directed Assembly of Block Copolymer Films at Elevated Temperatures. *Macromolecules* 2008, *41*, 2759–2761.

(40) Hammond, M. R.; Cochran, E.; Fredrickson, G. H.; Kramer, E. J. Temperature Dependence of Order, Disorder, and Defects in Laterally Confined Diblock Copolymer Cylinder Monolayers. *Macromolecules* 2005, *38*, 6575–6585.

(41) Sinturel, C.; Vayer, M.; Morris, M.; Hillmyer, M. a. Solvent Vapor Annealing of Block Polymer Thin Films. *Macromolecules* 2013, *46*, 5399–5415.

(42) Bosworth, J. K.; Paik, M. Y.; Ruiz, R.; Schwartz, E. L.; Huang, J. Q.; Ko, A. W.; Smilgies, D. M.; Black, C. T.; Ober, C. K. Control of Self-Assembly of Lithographically Patternable Block Copolymer Films. *ACS Nano* 2008, *2*, 1396–1402.

(43) Cheng, J.; Lawson, R. A.; Yeh, W.-M.; Jarnagin, N. D.; Tolbert, L. M.; Henderson, C. L. PS-B-PAA as a High X Polymer for Directed Self-Assembly: A Study of Solvent and Thermal Annealing Processes for PS-B-PAA. *Proc. SPIE*, 2013, *8680*, 86801V – 86801V – 4.

(44) Borah, D.; Senthamaraikannan, R.; Rasappa, S.; Kosmala, B.; Holmes, J. D.; Morris, M. a. Swift Nanopattern Formation of PS-B-PMMA and PS-B-PDMS Block Copolymer Films Using a Microwave Assisted Technique. *ACS Nano* 2013, *7*, 6583–6596.

(45) Durand, W. J.; Blachut, G.; Maher, M. J.; Sirard, S.; Tein, S.; Carlson, M. C.; Asano, Y.; Zhou, S. X.; Lane, A. P.; Bates, C. M.; *et al.* Design of High-X Block Copolymers for Lithography. *J. Polym. Sci. Part A Polym. Chem.* 2015, *53*, 344–352.

(46) Herr, D. J. C. Directed Block Copolymer Self-Assembly for Nanoelectronics Fabrication. *J. Mater. Res.* 2011, *26*, 122–139.

(47) Craig, G. S. W.; Nealey, P. F. Exploring the Manufacturability of Using Block Copolymers as Resist Materials in Conjunction with Advanced Lithographic Tools. *J. Vac. Sci. Technol. B Microelectron. Nanom. Struct.* 2007, *25*, 1969.

Lam Research Ex. 1013 - Page 63
Lam Research Corp. v. Inpria Corp.
IPR2025-00256 - U.S. Patent No. 11,537,048

(48) Stoykovich, M. P.; Kang, H.; Daoulas, K. C.; Liu, G.; Liu, C. C.; De Pablo, J. J.; Müller, M.; Nealey, P. F. Directed Self-Assembly of Block Copolymers for Nanolithography: Fabrication of Isolated Features and Essential Integrated Circuit Geometries. *ACS Nano* 2007, *1*, 168–175.

(49) Huang, E.; Pruzinsky, S.; Russell, T. P.; Mays, J.; Hawker, C. J. Neutrality Conditions for Block Copolymer Systems on Random Copolymer Brush Surfaces. *Macromolecules* 1999, *32*, 5299–5303.

(50) Russell, T. P.; Coulon, G.; Deline, V. R.; Miller, D. C. Characteristics of the Surface-Induced Orientation for Symmetric Diblock PS/PMMA Copolymers. *Macromolecules* 1989, *22*, 4600–4606.

(51) Xia, Y.; Olsen, B. D.; Kornfield, J. a; Grubbs, R. H. Efficient Synthesis of Narrowly Dispersed Brush Copolymers and Study of Their Assemblies: The Importance of Side Chain Arrangement. *J. Am. Chem. Soc.* 2009, *131*, 18525–18532.

(52) Mansky, P. Controlling Polymer-Surface Interactions with Random Copolymer Brushes. *Science*, 1997, *275*, 1458–1460.

(53) Bates, C. M.; Seshimo, T.; Maher, M. J.; Durand, W. J.; Cushen, J. D.; Dean, L. M.; Blachut, G.; Ellison, C. J.; Willson, C. G. Polarity-Switching Top Coats Enable Orientation of Sub-10-Nm Block Copolymer Domains. *Science* **2012**, *338*, 775–779.

(54) Segalman, R. A.; Yokoyama, H.; Kramer, E. J. Graphoepitaxy of Spherical Domain Block Copolymer Films. *Adv. Mater.* 2001, *13*, 1152–1155.

(55) Tiron, R.; Chevalier, X.; Couderc, C.; Pradelles, J.; Bustos, J.; Pain, L.; Navarro, C.; Magnet, S.; Fleury, G.; Hadziioannou, G. Optimization of Block Copolymer Self-Assembly through Graphoepitaxy: A Defectivity Study. *J. Vac. Sci. Technol. B Microelectron. Nanom. Struct.* 2011, *29*, 06F206.

(56) Bita, I.; Yang, J. K. W.; Jung, Y. S.; Ross, C. A.; Thomas, E. L.; Berggren, K. K. Graphoepitaxy of Self-Assembled Block Copolymers on Two-Dimensional Periodic Patterned Templates. *Science* 2008, *321*, 939–943.

(57) Sundrani, D.; Darling, S. B.; Sibener, S. J. Guiding Polymers to Perfection Macroscopic Alignment of Nanoscale Domains. *Nano Lett.* 2004, *4*, 273–276.

(58) Kim, S. O.; Solak, H. H.; Stoykovich, M. P.; Ferrier, N. J.; De Pablo, J. J.; Nealey, P. F. Epitaxial Self-Assembly of Block Copolymers on Lithographically Defined Nanopatterned Substrates. *Nature* 2003, *424*, 411–414.

(59) Ruiz, R.; Kang, H.; Detcheverry, F. a; Dobisz, E.; Kercher, D. S.; Albrecht, T. R.; de Pablo, J. J.; Nealey, P. F. Density Multiplication and Improved Lithography by Directed Block Copolymer Assembly. *Science* 2008, *321*, 936–939.

Lam Research Ex. 1013 - Page 64
Lam Research Corp. v. Inpria Corp.
IPR2025-00256 - U.S. Patent No. 11,537,048

(60) Stoykovich, M. P.; Müller, M.; Kim, S. O.; Solak, H. H.; Edwards, E. W.; de Pablo, J. J.; Nealey, P. F. Directed Assembly of Block Copolymer Blends into Nonregular Device-Oriented Structures. *Science* 2005, *308*, 1442–1446.

(61) Dair, B. J.; Avgeropoulos, A.; Hadjichristidis, N.; Capel, M.; Thomas, E. L. Oriented Double Gyroid Films via Roll Casting. *Polymer*. 2000, *41*, 6231–6236.

(62) Albalak, R. J.; Thomas, E. L.; Capel, M. S. Thermal Annealing of Roll-Cast Triblock Copolymer Films. *Polymer*, 1997, *38*, 3819–3825.

(63) Singh, G.; Yager, K. G.; Berry, B.; Kim, H.-C.; Karim, A. Dynamic Thermal Field-Induced Gradient Soft-Shear for Highly Oriented Block Copolymer Thin Films. *ACS Nano* 2012, *6*, 10335–10342.

(64) Liedel, C.; Schindler, K. A.; Pavan, M. J.; Lewin, C.; Pester, C. W.; Ruppel, M.; Urban, V. S.; Shenhar, R.; Böker, A. Electric-Field-Induced Alignment of Block Copolymer/nanoparticle Blends. *Small* 2013, *9*, 3276–3281.

(65) Amundson, K.; Helfand, E.; Quan, X.; Hudson, S. D.; Smith, S. D. Alignment of Lamellar Block Copolymer Microstructure in an Electric Field. 2. Mechanisms of Alignment. *Macromolecules* 1994, *27*, 6559–6570.

(66) Amundson Karl, H. E. Q. X. S. S. D. Alignment of Lamellar Block Copolymer Microstructure in an Electric Field: 1. Alignment Kinetics. *Macromolecules* 1993, *26*, 2698–2703.

(67) Amundson, K.; Helfand, E.; Davis, D. D.; Quan, X.; Patel, S. S.; Smith, S. D. Effect of an Electric Field on Block Copolymer Microstructure. *Macromolecules* 1991, *24*, 6546–6548.

(68) Majewski, P. W.; Gopinadhan, M.; Jang, W. S.; Lutkenhaus, J. L.; Osuji, C. O. Anisotropic Ionic Conductivity in Block Copolymer Membranes by Magnetic Field Alignment. *J. Am. Chem. Soc.* 2010, *132*, 17516–17522.

(69) Ahmed, S. R.; Kofinas, P. Magnetic Properties and Morphology of Block Copolymer-Cobalt Oxide Nanocomposites. *J. Magn. Magn. Mater.* 2005, *288*, 219–223.

(70) Ruiz, R.; Ruiz, N.; Zhang, Y.; Sandstrom, R. L.; Black, C. T. Local Defectivity Control of 2D Self-Assembled Block Copolymer Patterns. *Adv. Mater*. 2007, *19*, 2157–2162.

(71) Wagner, C.; Harned, N. EUV Lithography: Lithography Gets Extreme. *Nat. Photonics* 2010, *4*, 24–26.

(72) Tallents, G.; Wagenaars, E.; Pert, G. Optical Lithography: Lithography at EUV Wavelengths. *Nat Phot.* 2010, *4*, 809–811.

Lam Research Ex. 1013 - Page 65
Lam Research Corp. v. Inpria Corp.
IPR2025-00256 - U.S. Patent No. 11,537,048

(73) Lithography Roadmap on Track. *Nat Phot.* 2010, *4*, 20.

(74) Van den Heuvel, D.; Jonckheere, R.; Magana, J.; Abe, T.; Bret, T.; Hendrickx, E.; Cheng, S.; Ronse, K. Natural EUV Mask Blank Defects: Evidence, Timely Detection, Analysis and Outlook. In *Proc. of SPIE*; 2010; Vol. 7823, p. 78231T – 78231T – 12.

(75) Burns, J.; Abbas, M. EUV Mask Defect Mitigation through Pattern Placement. In *Proc. of SPIE*; 2010; Vol. 7823, pp. 782340–782345.

(76) Koh, C.; Georger, J.; Ren, L.; Huang, G.; Goodwin, F.; Wurm, S.; Ashworth, D.; Montgomery, W.; Pierson, B.; Park, J.; *et al.* Characterization of Promising Resist Platforms for Sub-30-Nm HP Manufacturability and EUV CAR Extendibility Study. In *Proc. SPIE*; 2010; Vol. 7636, pp. 763604–763616.

(77) Naulleau, P. P.; Anderson, C. N.; Baclea-an, L.-M.; Denham, P.; George, S.; Goldberg, K. A.; Jones, G.; McClinton, B.; Miyakawa, R.; Rekawa, S.; *et al.* Critical Challenges for EUV Resist Materials. In *Proc. of SPIE*; 2011; Vol. 7972, pp. 797202–797210.

(78) Ekinci, Y.; Vockenhuber, M.; Hojeij, M.; Wang, L.; Mojarad, N. M. Evaluation of EUV Resist Performance with Interference Lithography towards 11 Nm Half-Pitch and beyond. In *Proc. of SPIE*; 2013; Vol. 8679, pp. 867910–867911.

(79) Ekinci, Y.; Vockenhuber, M.; Mojarad, N.; Fan, D. EUV Resists towards 11nm Half-Pitch. In *Proc. of SPIE*; 2014; Vol. 9048, pp. 904804–904810.

(80) Cardineau, B.; Del Re, R.; Marnell, M.; Al-Mashat, H.; Vockenhuber, M.; Ekinci, Y.; Sarma, C.; Freedman, D. A.; Brainard, R. L. Photolithographic Properties of Tin-Oxo Clusters Using Extreme Ultraviolet Light (13.5 Nm). *Microelectron. Eng.* 2014, *127*, 44–50.

(81) Simone, D. De; Goethals, A. M.; Roey, F. Van; Zheng, T.; Foubert, P.; Hendrickx, E.; Vandenberghe, G.; Ronse, K. Progresses and Challenges of EUV Lithography Materials. *J. Photopolym. Sci. Technol.* 2014, *27*, 601–610.

(82) Cardineau, B.; Del Re, R.; Al-Mashat, H.; Marnell, M.; Vockenhuber, M.; Ekinci, Y.; Sarma, C.; Neisser, M.; Freedman, D. A.; Brainard, R. L. EUV Resists Based on Tin-Oxo Clusters. In *Proc. of SPIE*; 2014; Vol. 9051, p. 90511B – 90511B – 12.

(83) Oleksak, R. P.; Ruther, R. E.; Luo, F.; Fairley, K. C.; Decker, S. R.; Stickle, W. F.; Johnson, D. W.; Garfunkel, E. L.; Herman, G. S.; Keszler, D. A. Chemical and Structural Investigation of High-Resolution Patterning with HafSOx. *ACS Appl. Mater. Interfaces* 2014, *6*, 2917–2921.

(84) Krysak, M. E.; Blackwell, J. M.; Putna, S. E.; Leeson, M. J.; Younkin, T. R.; Harlson, S.; Frasure, K.; Gstrein, F. Investigation of Novel Inorganic Resist Materials for EUV Lithography. In *Proc. of SPIE*; 2014; Vol. 9048, pp. 904805–904807.

Lam Research Ex. 1013 - Page 66
Lam Research Corp. v. Inpria Corp.
IPR2025-00256 - U.S. Patent No. 11,537,048

(85) Krysak, M.; Trikeriotis, M.; Schwartz, E.; Lafferty, N.; Xie, P.; Smith, B.; Zimmerman, P.; Montgomery, W.; Giannelis, E.; Ober, C. K. Development of an Inorganic Nanoparticle Photoresist for EUV, E- Beam and 193 Nm Lithography. *Proc. SPIE* 2011, *7972*, 79721C – 79721C – 6.

(86) Ouyang, C. Y.; Lee, J.-K.; Ober, C. K. Negative-Tone Development of Photoresists in Environmentally Friendly Silicone Fluids. 2012, *8325*, 832524.

(87) Bae, W. J.; Trikeriotis, M.; Sha, J.; Schwartz, E. L.; Rodriguez, R.; Zimmerman, P.; Giannelis, E. P.; Ober, C. K. High Refractive Index and High Transparency HfO2 Nanocomposites for next Generation Lithography. *J. Mater. Chem.* 2010, *20*, 5186.

(88) Jiang, J.; Chakrabarty, S.; Yu, M.; Ober, C. K. Metal Oxide Nanoparticle Photoresists for EUV Patterning. *J. Photopolym. Sci. Technol.* 2014, *27*, 663–666.

(89) Chakrabarty, S.; Sarma, C.; Li, L.; Giannelis, E. P.; Ober, C. K. Increasing Sensitivity of Oxide Nanoparticle Photoresists. In *Proc. of SPIE*; 2014; Vol. 9048, p. 90481C – 90481C – 5.

(90) Chakrabarty, S.; Ouyang, C.; Krysak, M.; Trikeriotis, M.; Cho, K.; Giannelis, E. P.; Ober, C. K. Oxide Nanoparticle EUV Resists: Toward Understanding the Mechanism of Positive and Negative Tone Patterning. In *Proc. of SPIE*; 2013; Vol. 8679, pp. 867906–867908.

(91) Kryask, M.; Trikeriotis, M.; Ouyang, C.; Chakrabarty, S.; Giannelis, E. P.; Ober, C. K. Nanoparticle Photoresists: Ligand Exchange as a New, Sensitive EUV Patterning Mechanism. *J. Photopolym. Sci. Technol.* 2013, *26*, 659–664.

(92) Ouyang, C. Y.; Chung, Y. S.; Li, L.; Neisser, M.; Cho, K.; Giannelis, E. P.; Ober, C. K. Non-Aqueous Negative-Tone Development of Inorganic Metal Oxide Nanoparticle Photoresists for next Generation Lithography. In *Proc. of SPIE*; 2013; Vol. 8682, p. 86820R – 86820R – 6.

(93) Krysak, M.; Trikeriotis, M.; Schwartz, E.; Lafferty, N.; Xie, P.; Smith, B.; Zimmerman, P.; Montgomery, W.; Giannelis, E.; Ober, C. K. Development of an Inorganic Nanoparticle Photoresist for EUV, E-Beam, and 193nm Lithography. In *Proc. of SPIE*; 2011; Vol. 7972, p. 79721C – 79721C – 6.

(94) Yoshimoto, K.; Stoykovich, M. P.; Cao, H. B.; De Pablo, J. J.; Nealey, P. F.; Drugan, W. J. A Two-Dimensional Model of the Deformation of Photoresist Structures Using Elastoplastic Polymer Properties. *J. Appl. Phys.* 2004, *96*, 1857–1865.

(95) Kozawa, T.; Tagawa, S.; Oizumi, H.; Nishiyama, I. Acid Generation Efficiency in a Model System of Chemically Amplified Extreme Ultraviolet Resist. *Journal of Vacuum Science & Technology B: Microelectronics and Nanometer Structures*, 2006, *24*, L27–L30.

Lam Research Ex. 1013 - Page 67
Lam Research Corp. v. Inpria Corp.
IPR2025-00256 - U.S. Patent No. 11,537,048

(96) Brainard, R. L.; Trefonas, P.; Lammers, J. H.; Cutler, C. A.; Mackevich, J. F.; Trefonas, A.; Robertson, S. A. Shot Noise, LER, and Quantum Efficiency of EUV Photoresists. In *Proc. of SPIE*; 2004; Vol. 5374, pp. 74–85.

(97) George, S. A.; Naulleau, P. P. Out of Band Radiation Effects on Resist Patterning. In *Proc. of SPIE*; 2011; Vol. 7969, pp. 796911–796914.

(98) Inukai, K.; Sharma, S.; Nakagawa, H.; Shimizu, M.; Kimura, T. Effects of out-of-Band Radiation on EUV Resist Performance. In *Proc. of SPIE*; 2012; Vol. 8322, p. 83220X – 83220X – 7.

(99) Kozawa, T.; Tagawa, S.; Shell, M. Resolution Degradation Caused by Multispur Effect in Chemically Amplified Extreme Ultraviolet Resists. *J. Appl. Phys.* 2008, *103*.

(100) Gronheid, R.; Fonseca, C.; Leeson, M. J.; Adams, J. R.; Strahan, J. R.; Willson, C. G.; Smith, B. W. EUV Resist Requirements: Absorbance and Acid Yield. In *Proc. of SPIE*; 2009; Vol. 7273, pp. 727332–727338.

(101) Tarutani, S.; Tsubaki, H.; Takahashi, H.; Itou, T. Study on Approaches for Improvement of EUV-Resist Sensitivity. In *Proc. of SPIE*; 2010; Vol. 7639, pp. 763908–763909.

(102) Tagawa, T. K. and K. O. and J. N. and S. Feasibility Study on High-Sensitivity Chemically Amplified Resist by Polymer Absorption Enhancement in Extreme Ultraviolet Lithography. *Appl. Phys. Express* 2008, *1*, 67012.

(103) Oleksak, R. P.; Herman, G. S. Characterization of High-Resolution HafSOx Inorganic Resists. In *Proc. of SPIE*; 2014; Vol. 9048, p. 90483H – 90483H – 8.

(104) Amador, J. M.; Decker, S. R.; Lucchini, S. E.; Ruther, R. E.; Keszler, D. A. Patterning Chemistry of HafSOx Resist. In *Proc. of SPIE*; 2014; Vol. 9051, p. 90511A – 90511A – 6.

(105) Kim, Y.; Massoud, H. Z.; Fair, R. B. The Effect of Ion-Implantation Damage on Dopant Diffusion in Silicon during Shallow-Junction Formation. *J. Electron. Mater.* 1989, *18*, 143–150.

(106) Cho, K.; Numan, M.; Finstad, T. G.; Chu, W. K.; Liu, J.; Wortman, J. J. Transient Enhanced Diffusion during Rapid Thermal Annealing of Boron Implanted Silicon. *Appl. Phys. Lett.* 1985, *47*, 1321.

(107) Michel, A. E.; Rausch, W.; Ronsheim, P. A.; Kastl, R. H. Rapid Annealing and the Anomalous Diffusion of Ion Implanted Boron into Silicon. *Appl. Phys. Lett.* 1987, *50*, 416–418.

Lam Research Ex. 1013 - Page 68
Lam Research Corp. v. Inpria Corp.
IPR2025-00256 - U.S. Patent No. 11,537,048

(108) Michel, A. E.; Rausch, W.; Ronsheim, P. A.; Kastl, R. H. Rapid Annealing and the Anomalous Diffusion of Ion Implanted Boron into Silicon. *Appl. Phys. Lett.* 1987, *50*, 416–418.

(109) Bachmann, F. Industrial Applications of High Power Diode Lasers in Materials Processing. *Appl. Surf. Sci.* 2003, *208-209*, 125–136.

(110) Bahir, G.; Kalish, R.; Nemirovsky, Y. Electrical Properties of Donor and Acceptor Implanted $Hg_{1-10}Cd_xTe$ Following Cw CO2 Laser Annealing. *Appl. Phys. Lett.* 1982, *41*.

(111) Sedgwick, T. O. Short Time Annealing. *J. Electrochem. Soc.* 1983, *130* , 484–493.

(112) Nagarkar, P. V; Sichel, E. K. XPS Study of Polyimide H-Film after Heat-Treatment and Laser Processing. *J. Electrochem. Soc.* 1989, *136* , 2979–2982.

(113) Rischel, C.; Rousse, A.; Uschmann, I.; Albouy, P.-A.; Geindre, J.-P.; Audebert, P.; Gauthier, J.-C.; Froster, E.; Martin, J.-L.; Antonetti, A. Femtosecond Time-Resolved X-Ray Diffraction from Laser-Heated Organic Films. *Nature* 1997, *390*, 490–492.

(114) Jung, B.; Satish, P.; Bunck, D. N.; Dichtel, W. R.; Ober, C. K.; Thompson, M. O. Laser-Induced Sub-Millisecond Heating Reveals Distinct Tertiary Ester Cleavage Reaction Pathways in a Photolithographic Resist Polymer. *ACS Nano* 2014, *8*, 5746–5756.

(115) Krysak, M.; Jung, B.; Thompson, M. O.; Ober, C. K. Investigation of Acid Diffusion during Laser Spike Annealing with Systematically Designed Photoacid Generators. *Proc. SPIE* 2012, *8325*, 83250M – 83250M.

(116) Jung, B.; Sha, J.; Paredes, F.; Chandhok, M.; Younkin, T. R.; Wiesner, U.; Ober, C. K.; Thompson, M. O. Kinetic Rates of Thermal Transformations and Diffusion in Polymer Systems Measured during Sub-Millisecond Laser-Induced Heating. *ACS Nano* 2012, *6*, 5830–5836.

(117) Sha, J.; Jung, B.; Thompson, M. O.; Ober, C. K.; Chandhok, M.; Younkin, T. R.; Sha, J.; Paredes, F.; Ober, C. K.; Thompson, M. O.; *et al.* Submillisecond Post-Exposure Bake of Chemically Amplified Resists by CO_2 Laser Spike Annealing. *J. Vac. Sci. Technol. B* 2009, *27*, 3020–3024.

(118) Jung, B.; Ober, C. K.; Thompson, M. O.; Science, M.; Hall, B. Deprotection Reaction Kinetics in Chemically Amplified Photoresists Determined by Sub-Millisecond Post Exposure Bake. *Proc. SPIE* 2012, *8325*, 83250N.

(119) Jiang, J.; Jung, B.; Thompson, M. O.; Ober, C. K. Line Edge Roughness of High Deprotection Activation Energy Photoresist by Using Sub-Millisecond Post Exposure Bake. In *Proc. of SPIE*; 2013; Vol. 8682, p. 86821N – 86821N – 7.

Lam Research Ex. 1013 - Page 69
Lam Research Corp. v. Inpria Corp.
IPR2025-00256 - U.S. Patent No. 11,537,048

(120) Jiang, J.; Thompson, M. O.; Ober, C. K. Line Width Roughness Reduction by Rational Design of Photoacid Generator for Sub-Millisecond Laser Post-Exposure Bake. In *Proc. of SPIE*; 2014; Vol. 9051, p. 90510H – 90510H – 6.

(121) Jung, B. Laser-Induced Millisecond Heating of Polymers and Small Molecules for Pattern Development. Ph.D. Dissertation, Cornell University, Ithaca, NY, 2014.

Lam Research Ex. 1013 - Page 70
Lam Research Corp. v. Inpria Corp.
IPR2025-00256 - U.S. Patent No. 11,537,048

CHAPTER 2 MILLISECOND LASER PEAK TEMPERATURE CALIBRATION BY PLATINUM THERMISTOR

2.1. Introduction

Laser spike annealing of polymers was studied in this thesis to determine for reaction kinetics and phase separation behavior studies. For kinetics studies, precise temperature calibrations were critical to obtain quantitative results and to control processing conditions. However, simple thermometer or thermalcouple[1] cannot monitoring of *in situ* temperature changes, since heating and cooling rates are in the range 10^4-10^5 K/s range. In addition, the laser beam size is less than 2 mm, smaller than the sizes of most thermocouples; thus locating the peak position is challenging.

To measure *in situ* temperatures during laser annealing, we fabricated thin film platinum resistors on a Si wafer to monitor the temperature dependent resistance change. Resistance changes were captured using an oscilloscope with limited cutoff frequency, which can be designed for the MHz range. Spatial limitation can be solved by using high resolution photolithography, which can easily resolve 100 nm features.[2,3]

The resistivity of metal increase approximately linearly with temperature in the temperature range of interest, $\rho(T) = \rho_0 + \alpha(T - T_0)$, where $\rho(T_0)$ is the resistivity at a reference temperature T_0 and α is the temperature coefficient of resistivity. When the laser scans across the platinum thermistor, the resistance of the thermistor responds to the temperature change. By measuring the resistance change, we can determine the temperature.

Lam Research Ex. 1013 - Page 71
Lam Research Corp. v. Inpria Corp.
IPR2025-00256 - U.S. Patent No. 11,537,048

The melting temperatures of platinum and silicon are 1768 °C and 1414 °C respectively, so theoretically a Pt thermistor fabricated on Si can measure up to 1414 °C. However, as the strength of a silicon wafer decreases significantly from 750 °C to 800 °C.[4,5] Slip dislocation defects generally limits processing temperature. With Pt resistors, temperatures are generally maintained below 800 °C to avoid changes in Pt resistor structures. Resistance changes above 800 °C were extrapolated from resistance-power functions obtained in the low temperature regime. Absolute temperatures were further established using the known melting point of Au and Si.

Temperature calibration of the Cornell CO_2 laser system was previously performed by Byungki Jung[6] and simulation of heat diffusion into Si was performed by K. Iyengar.[7] Diode laser temperature calibration will be discussed in this chapter.

2.2. Experimental methods

2.2.1. Platinum thermistor fabrication

There are three potential mechanisms for the optical absorption of light on silicon: band gap absorption, lattice absorption and free carrier absorption.[8–11] The bandgap of Si corresponds to photons with λ = 1.15 μm at room temperature. Incident photon with higher energy greater than this value can be absorbed by band to band transition. The wavelength of the diode laser (980 nm) is in this regime. Free carrier absorption can be ignored in this bandgap absorption regime.[7,12] Consequently, lightly doped Si wafers with resistivity of 10-20 Ω·cm were for laser diode experiments and for Pt thermistor fabrication for diode laser temperature measurements.

Lam Research Ex. 1013 - Page 72
Lam Research Corp. v. Inpria Corp.
IPR2025-00256 - U.S. Patent No. 11,537,048

A 4-point probe for resistivity measurement was used to enable within the heated zone. The thin film platinum thermistor structure is shown in Figure 2.1a. The actual measurement resistor in the center is 2 μm wide and located 10 μm between the top contact wires, while the bottom contacts are 30 μm apart. The two top contacts measure the voltage drop of the platinum resistor, with current flowing through (or voltage drop over known system resistance). The bottom contacts can be used as backup for the voltage measurements.

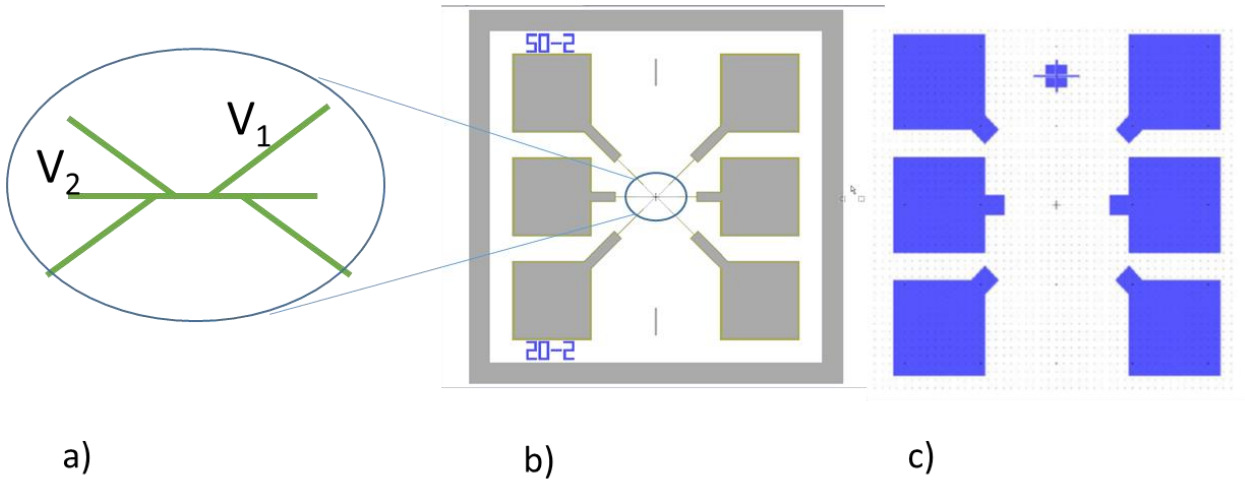

Figure 2.1 Platinum thermistor design a) detailed schematic plot of the platinum measurement resistor. b) circuit patterns of the thermistor of the Pt layer. Six squares shown here are used as contacts to the center platinum resistor. The zoom in images shows the structures of the platinum resistor. c) mask for the thick of the Ni layer.

Two masks were used for Pt (Figure 2.1b) and Ni layers (Figure 2.1b). The Pt layer defined the circuits of the 4-point measurement circuit, while the Ni layer was designed to reduce contact resistivity to provide a thick layer for bonding wires. Si wafers were thermally oxidized in a furnace to grow a 100 nm thick SiO_2 layer as a uniform dielectric layer. LOR5A

Lam Research Ex. 1013 - Page 73
Lam Research Corp. v. Inpria Corp.
IPR2025-00256 - U.S. Patent No. 11,537,048

and Shipley1805 resist were applied on the SiO_2 and patterned using the mask shown in Figure 2.1c. Subsequently, a 250 nm Ni layer was deposited using physical vapor deposition. Shipley 1165 stripper was used to remove the lift-off resist for the Pt pads. Another layer of lift-off photoresist was applied and patterned using the mask shown in Figure 2.1b. A 2 nm Cr layer was then deposited as an adhesion layer before deposition of a 40 nm Pt layer. After stripping resist, these wafers were diced into 9 mm x 9 mm dies. The device stack cross-section is shown schematically in Figure 2.2. Each die was glued and wire bonded in a dual in-line package as shown in Figure 2.3.

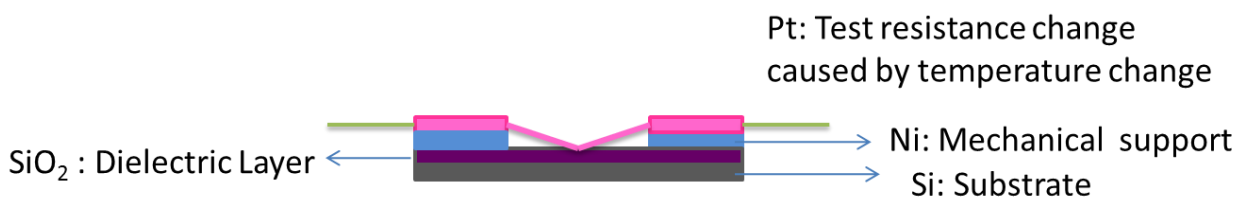

Figure 2.2 Schematic figure of thermistor stack cross-section.

Lam Research Ex. 1013 - Page 74
Lam Research Corp. v. Inpria Corp.
IPR2025-00256 - U.S. Patent No. 11,537,048

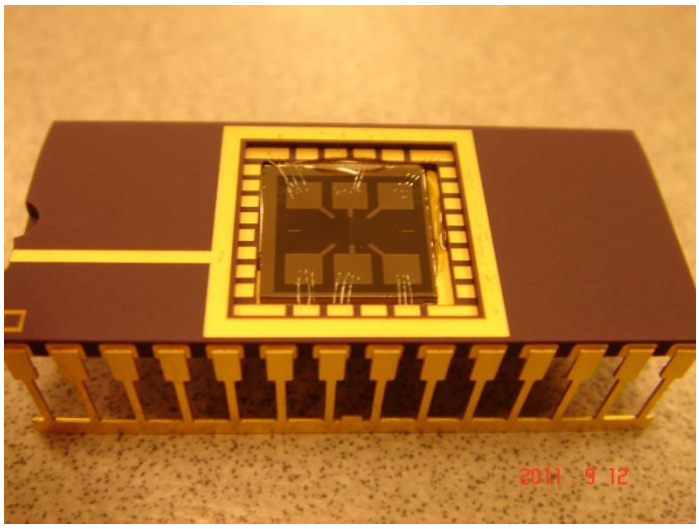

Figure 2.3 Image of platinum thermistor for temperature calibration.

2.2.2. Temperature calibration by Si Au melting experiment

Gold and silicon melting points were used as absolute calibration points for the following reasons: 1) Au and Si melting temperatures do not change with annealing time or temperature ramp rate, and 2) these elements are not oxidized in air during heating before melting.

The laser powers required to reach the Si melt at various dwell times were measured by a single laser scan across a wafer. Upon melting, wafer surfaces along laser track became rough and this change could be readily observed by light scattering using optical dark field microscopy as (Figure 2.4a). The lowest temperatures that caused these changes was defined to be the melting power.

To measure the laser power to reach Au melting, 60 nm thin Au films were deposited on a Si wafer and patterned as 2, 5, 10 μm squares with 20 μm spacing using lift-off photolithography.

Lam Research Ex. 1013 - Page 75
Lam Research Corp. v. Inpria Corp.
IPR2025-00256 - U.S. Patent No. 11,537,048

A single layer of 3-mercaptopropyltrimethoxysilane was deposited before Au deposition to promote adhesion. The Au films were designed to cover only small area to avoid significant modification of the heat flow. The laser was scanned across these Au patterns at various powers and dwell times. At the melting point, gold squares collapse into small spheres to minimize their surface energy in the liquid state, and were easily observed by optical microscopy (Figure 2.4 b). The lowest powers resulting in these changes were defined as melting powers.

Figure 2.4 Dark field images of Si and bright field images of Au melting. Reprinted from ref.12

2.2.3. Resistivity data acquisition

The electrical setup used for resistivity measurements is shown in Figure 2.5. The top probes of the Pt thermistor were connected to an oscillator measuring the voltage drop, V_1, of the resistor. The voltage drop across the thermistor was amplified 10 times using a Tectronics AM502 differential amplifier, with a low pass filter at 3 MHz used to reduce noise. The center probes of the Pt thermistor were connected to a pulse generator to produce currents with the

Lam Research Ex. 1013 - Page 76
Lam Research Corp. v. Inpria Corp.
IPR2025-00256 - U.S. Patent No. 11,537,048

current measured across a through the resistor 50 Ω resistor (or voltage drop V_2). A +1V bias pulse was given to the thermistor after the moving stage accelerated to the desired speed but before the laser reach the thermistor device. Then oscilloscope voltages were logged from channel 1 and channel 2 with minimum delay. These timing cycles are schematically shown in figure 2.6. The oscilloscope traces are shown in Figure 2.7 as an example. Channel 1 recorded the voltage drop across the thermistor (V_1) and channel 2 recorded the voltage drop (V_2) across a 50 Ω resistor (R_0), monitoring the current. The Pt resistivity can be calculated by $R=V_1/V_2 \cdot R_0 \cdot$Amplification. After conversion, time dependent Pt resistivity during a laser scan was obtained.

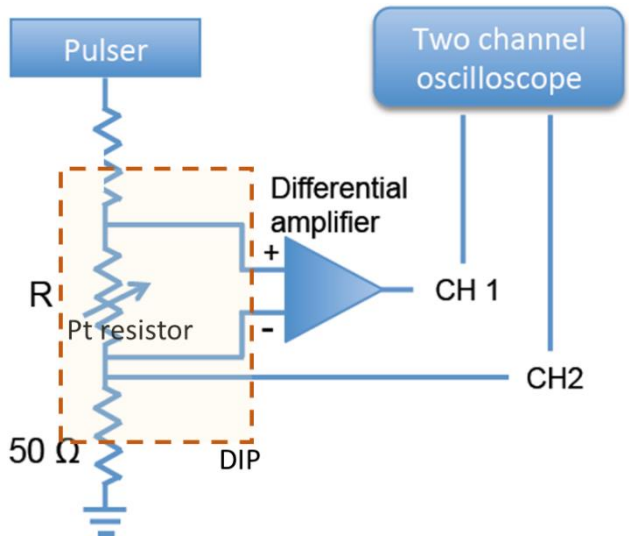

Figure 2.5 Schematic of thermistor measurement.

Lam Research Ex. 1013 - Page 77
Lam Research Corp. v. Inpria Corp.
IPR2025-00256 - U.S. Patent No. 11,537,048

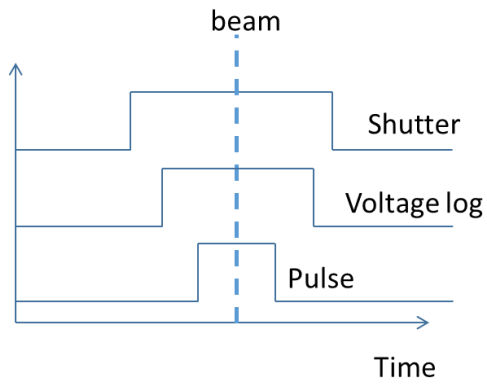

Figure 2.6 Time setting for resistivity measurement. Shutter first opens after the stage reach a constant velocity. The oscilloscope is triggered to capture the entire pulse transient which is centered on the beam passing over the thermistor.

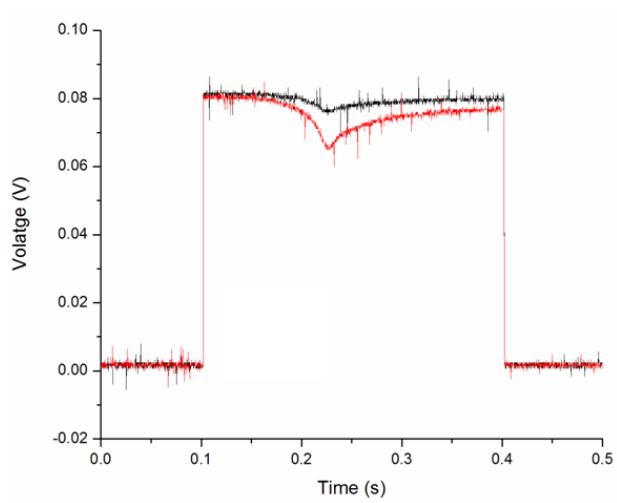

Figure 2.7 Output from the oscilloscope. Channel 1 shows the voltage change across the thermistor and Channel 2 shows the voltage across the 50 Ω resistor, which measured the current.

Lam Research Ex. 1013 - Page 78
Lam Research Corp. v. Inpria Corp.
IPR2025-00256 - U.S. Patent No. 11,537,048

The laser beam is 1460 μm by 375 μm, while the Pt resistor is only 2 μm by10 μm. In order to precisely locate the laser peak position, we scanned the laser across the Pt thermistor along its short axis over a 5 mm width with 0.2 mm spacing as shown in Figure 2.8. Spatial resistivity change profiles were obtained as shown in Figure 2.9 and the peak position was used for peak resistivity measurement.

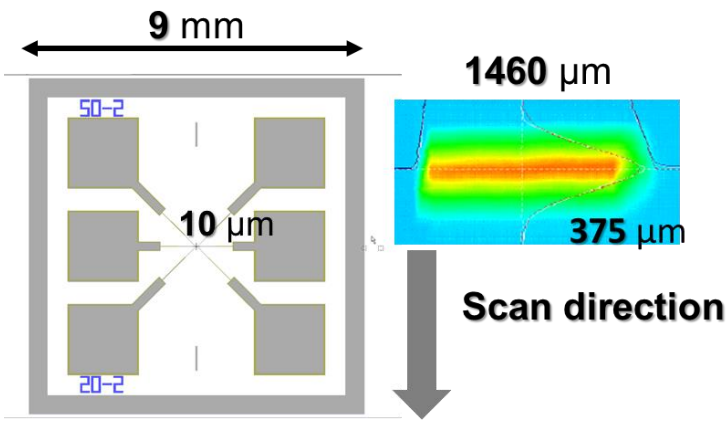

Figure 2.8 Orientation of the diode laser across the thermistor device.

Lam Research Ex. 1013 - Page 79
Lam Research Corp. v. Inpria Corp.
IPR2025-00256 - U.S. Patent No. 11,537,048

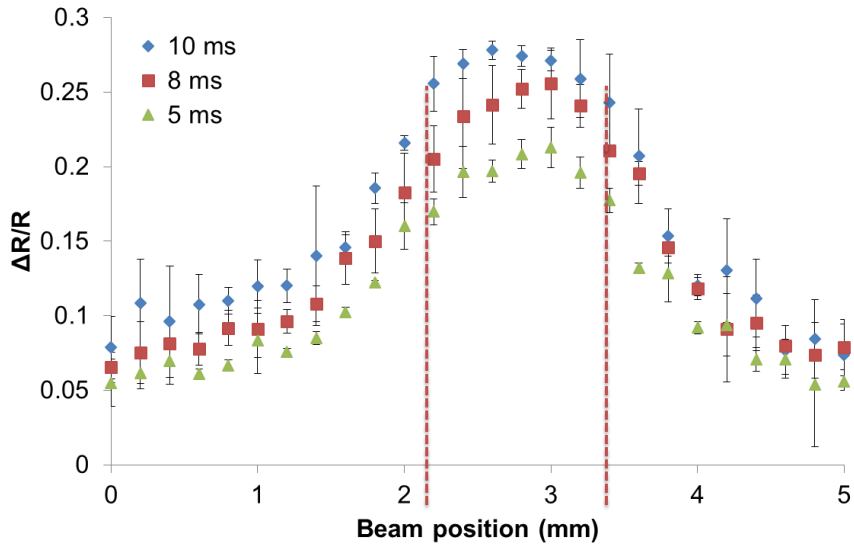

Figure 2.9 Peak resistivity change as a function of lateral beam position. The center of the scanning laser 2.8 mm in this example, with a relatively constant temperature zone approximately 1 mm wide. (This data is obtained before laser reinstall at 2011.11)

Resistivity changes during scans at the laser center position were measured for various dwell times. After subtracting the baseline Pt resistivity (at room temperature), the time dependent resistivity change was obtained (Figure 2.10). The measured ΔR_{max} was plotted as a function of power for various dwell times (Figure 2.11). These data were fit into quadratic form to extrapolate the resistivity to the gold and Si melting temperatures (Figure 2.12). By correlating the extrapolated thermistor resistivity at the Au and Si melting powers with melting temperatures, the peak temperature as a function of the laser power and dwell was obtained.

Lam Research Ex. 1013 - Page 80
Lam Research Corp. v. Inpria Corp.
IPR2025-00256 - U.S. Patent No. 11,537,048

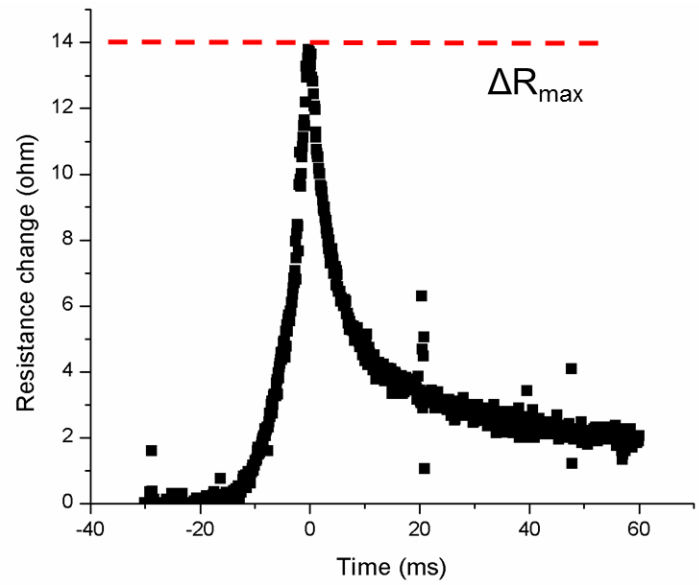

Figure 2.10 Time dependent Pt resistivity change during a 10ms dwell laser scan at 40W.

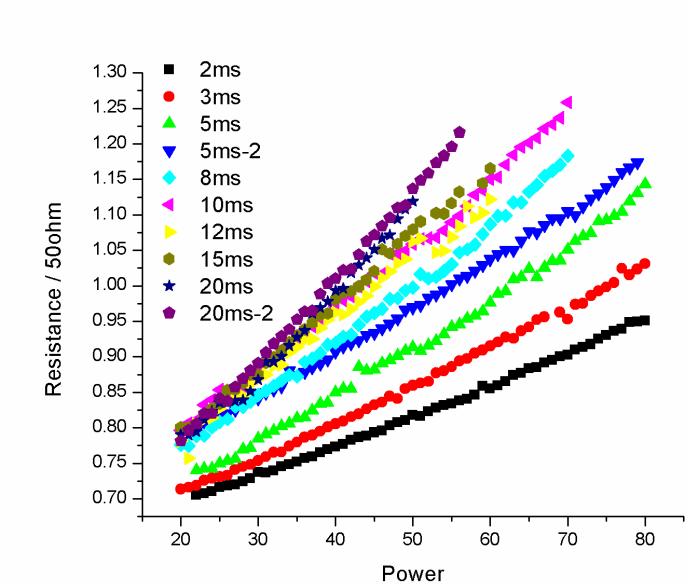

Figure 2.11 Pt thermistor resistivity as a function of power for dwell times from 2 ms to 20 ms.

Lam Research Ex. 1013 - Page 81
Lam Research Corp. v. Inpria Corp.
IPR2025-00256 - U.S. Patent No. 11,537,048

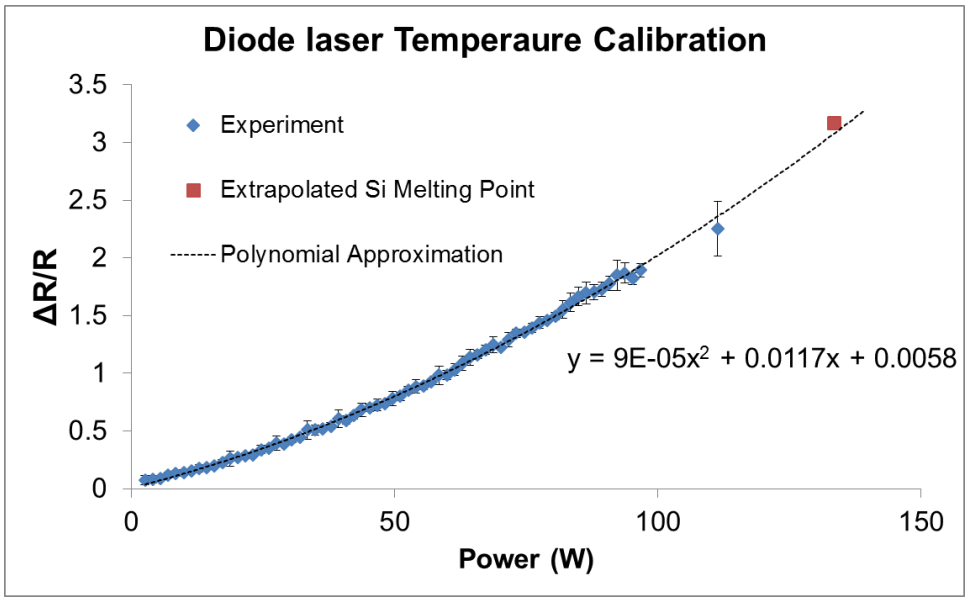

Figure 2.12 Measured and extrapolated ΔR/R as a function of the incident laser power for a dwell of 10 ms. Extrapolating curve to the Si melting power provides an absolute temperature calibration. (This data is obtained before laser reinstall at 2011.11)

2.3. Results and discussion

The results of laser peak temperature calibration shown here was obtained after laser reinstall at June 2014. The peak resistivity as a function of laser powers during 5 ms, 10 ms and 20 ms diode laser scans were measured (Figure 2.13) and fit into a secondary order polynomial quadric. Coefficients are given in Table 2.1. The coefficients increase with increasing dwell time as expected; longer dwell at a given laser power will result in a higher temperature.

Lam Research Ex. 1013 - Page 82
Lam Research Corp. v. Inpria Corp.
IPR2025-00256 - U.S. Patent No. 11,537,048

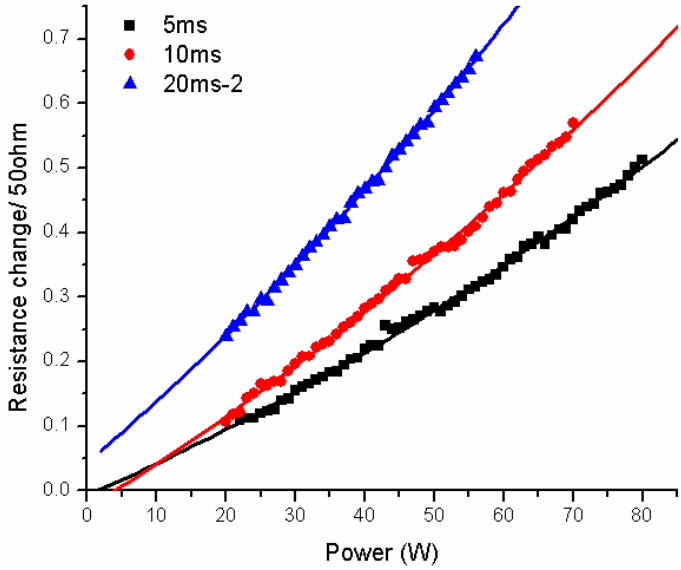

Figure 2.13 Peak resistivity for several dwell times and their quadric fits.

Au and Si melting were obtained for 10 and 20 ms dwells as listed in Table 2.2.The laser power was insufficient to reach either Au or Si melt with a 5 ms dwell and hence this data is not available. The average resistivity at Au and Si melt were used for the absolute temperature calibration. Resistance change at each melting power was calculated from the quadratic fits in table 2.2. Given Au and Si melt temperatures of 1064 °C and 1414 °C, the temperature as a function of resistivity was determined to be T (°C) = R*494.3+147. Power-temperature relationship were thus obtained for each dwell time (Figure 2.14).

Lam Research Ex. 1013 - Page 83
Lam Research Corp. v. Inpria Corp.
IPR2025-00256 - U.S. Patent No. 11,537,048

Table 2.1 Fitting parameters of second order polynomial equation for 5, 10, 20 ms.

Dwell		Value	Standard Error
5 ms	a	-6.78E-03	7.73E-03
	b	4.68E-03	3.25E-04
	c	2.10E-05	3.15E-06
10 ms	a	-2.73E-02	9.18E-03
	b	6.63E-03	4.36E-04
	c	2.49E-05	4.80E-06
20 ms	a	-0. 04384	9.32E-03
	b	9.05E-03	5.16E-04
	c	3.76E-05	6.74E-06

Table 2.2 Au and Si melting power for 10, 20 ms diode laser annealing.

Dwell	Au power/ W	Si power/ W	Resistivity at Au melts /Ω	Resistivity at Au melts /Ω
10 ms	173	216	1.866	2.567
20 ms	134	169	1.844	2.560

Lam Research Ex. 1013 - Page 84
Lam Research Corp. v. Inpria Corp.
IPR2025-00256 - U.S. Patent No. 11,537,048

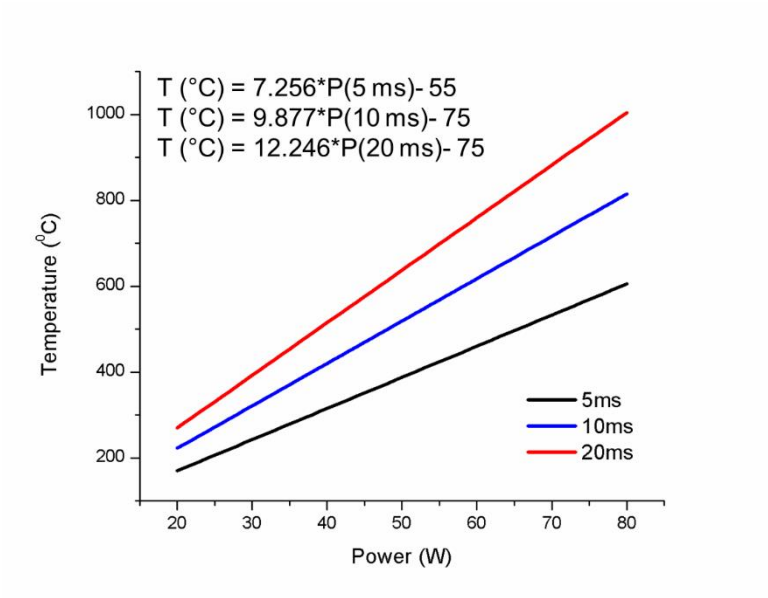

Figure 2.14 Temperature as a function of laser power for 5, 10, 20 ms dwells during diode laser annealing.

Temperature profiles as a function of dwell for 5, 10 and 20 ms diode laser annealing are shown in Figure 2.15. As the laser approaches the resistor, the temperature spikes up with a ramp rates on the order of 10^4- 10^5 K/s. As the laser beam passes, the temperature drops rapidly initially and then slowly returns to room temperature. The total time to cool to room temperature is about five times the dwell time.

The spatial temperature profile of the diode laser is shown in Figure 2.16. The highest temperature in this profile is defined as the center of the beam (0 mm). From the position of -0.6 mm to +0.6 mm, the temperature drops roughly 18% across this 1.2 mm distance corresponding to the laser FWHM length in long axis. From the position -0.6 mm to -1.8 mm to +0.6 mm to +1.8 mm, the temperature drops an additional 60% across the 1.2 mm distance.

Lam Research Ex. 1013 - Page 85
Lam Research Corp. v. Inpria Corp.
IPR2025-00256 - U.S. Patent No. 11,537,048

With the spatial laser temperature profile, a laser scan track spacing of 1.2 mm was used to ensure heating uniformity and to minimize stitching effects. The thermal gradient along each axis is between laterally ranges from 20-100 K/mm.

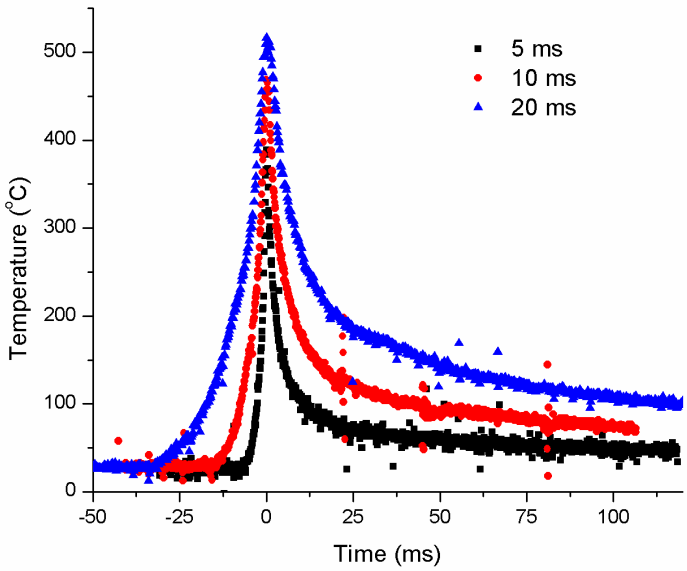

Figure 2.15 Temporal temperature profile

Lam Research Ex. 1013 - Page 86
Lam Research Corp. v. Inpria Corp.
IPR2025-00256 - U.S. Patent No. 11,537,048

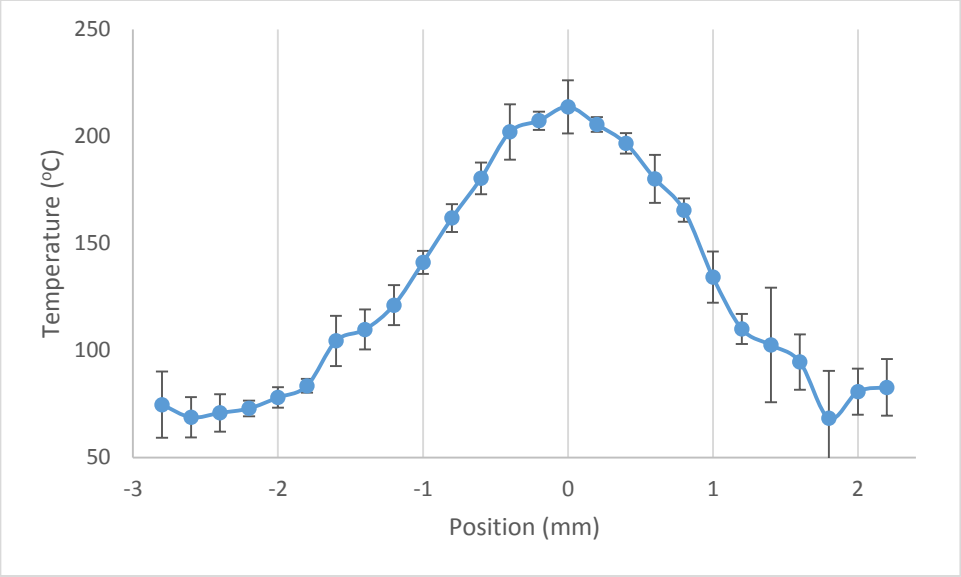

Figure 2.16 Spatial temperature profile.

Reference

(1) Kreider, K. G.; Gillen, G. High Temperature Materials for Thin-Film Thermocouples on Silicon Wafers. *Thin Solid Films* 2000, *376*, 32–37.

(2) Rajagopal, A.; Walavalkar, S.; Chen, S.; Guo, L.; Gwinn, T.; Scherer, A. Microscaled and Nanoscaled Platinum Sensors. *Appl. Phys. Lett.* 2010, *97*.

(3) Kittl, J. A.; Reitano, R.; Aziz, M. J.; Brunco, D. P.; Thompson, M. O. Time-Resolved Temperature Measurements during Rapid Solidification of Si-As Alloys Induced by Pulsed-Laser Melting. *J. Appl. Phys.* 1993, *73*, 3725–3733.

Lam Research Ex. 1013 - Page 87
Lam Research Corp. v. Inpria Corp.
IPR2025-00256 - U.S. Patent No. 11,537,048

(4) Moslehi, M. M. Process Uniformity and Slip Dislocation Patterns in Linearly Ramped-Temperature Transient Rapid Thermal Processing of Silicon. *IEEE Trans. Semicond. Manuf.* 1989, *2*, 130–140.

(5) Queisser, H. J. Slip Patterns on Boron-Doped Silicon Surfaces. *J. Appl. Phys.* 1961, *32*, 1776.

(6) Iyengar, K.; Jung, B.; Willemann, M.; Clancy, P.; Thompson, M. O. Experimental Determination of Thermal Profiles during Laser Spike Annealing with Quantitative Comparison to 3-Dimensional Simulations. *Appl. Phys. Lett.* 2012, *100*, 211915.

(7) Philipp, H. R.; Taft, E. A. Optical Constants of Silicon in the Region 1 to 10 Ev. *Phys. Rev.* 1960, *120*, 37–38.

(8) Sproul, A. B.; Green, M. A. Intrinsic Carrier Concentration and Minority-Carrier Mobility of Silicon from 77 to 300 K. *J. Appl. Phys.* 1993, *73*, 1214–1225.

(9) Green, M. A.; Keevers, M. J. Optical-Properties of Intrinsic Silicon at 300 K. *Prog. Photovoltaics* 1995, *3*, 189–192.

(10) Dash, W. C.; Newman, R. Intrinsic Optical Absorption in Single-Crystal Germanium and Silicon at 77 K and 300 K. *Phys. Rev.* 1955, *99*, 1151–1155.

(11) Iyengar, K. A. Modeling Sub-Millisecond Laser Spike Annealing Processes. Ph.D. Dissertation, Cornell University, Ithaca, NY, 2012.

Lam Research Ex. 1013 - Page 88
Lam Research Corp. v. Inpria Corp.
IPR2025-00256 - U.S. Patent No. 11,537,048

CHAPTER 3 SMALL-MOLECULE DRIVEN CHEMICAL REACTION AND DIFFUSION KINETICS DURING LASER-INDUCED SUB-MILLISECOND HEATING FOR PATTERNING APPLICATIONS

Abstract

Reactions in solid-state chemistry are controlled by the diffusion of reactants, with the apparent rate determined by the temperature dependent rates of each individual process. Due to different activation energies for each distinct process, the rate limiting step and overall reaction rate may shift with temperature. In this work, we studied the acid catalyzed deprotection of acid labile groups of chemically amplified photopolymers to understand the effects of temperature on the diffusion-coupled reaction. In this system, acids formed during exposure of photoacid generators (PAGs) to ultraviolet radiation diffuse and act as catalyst for the deprotection reaction. By using very short time laser induced heating for a post-exposure bake (PEB) step, the potential reaction temperature range is extended by one hundred degrees to several hundred degrees compared to traditional thermal processing. Thermal degradation during laser heating is avoided by simultaneously reducing the time from minutes to sub-millisecond time frames. Both diffusion and reaction rates were measured in the high temperature region for three different photoresists and two PAGs and their activation energies were extracted. The diffusion or reaction limiting effects were also examined by comparing the patterning results. We find that photopolymers with high deprotection activation energies and PAGs with low diffusion activation energies show the best imaging qualities under this

Lam Research Ex. 1013 - Page 90
Lam Research Corp. v. Inpria Corp.
IPR2025-00256 - U.S. Patent No. 11,537,048

laser PEB. The results provide a path to rational design of photopolymer systems for future high resolution, low line edge roughness lithography [1].

3.1. Introduction

In solid-state chemistry, reactions are almost always coupled to the diffusion of one or more reactant species. For example, electrochemiluminescence is limited by the transport of light-emitting molecules (ions) through an electrolyte between electrodes.[1] Similarly, charge transfer in the solid electrolyte of a lithium ion battery is dependent on the diffusion of lithium ions.[2] In photolithography, photopolymer side-chain cleavage reactions occur via diffusion of acid catalysts generated during deep UV (DUV) exposure.[3] However the observed reaction rate is often determined by the relative rates of multiple kinetic processes. As an example, one might consider the diffusion of reactants to an active site versus the fundamental chemical reaction rate. These rates generally increase with increasing temperature and are described by the Arrhenius equation. Depending on their activation energies, the rate of increase with temperature is different and hence the rate limiting steps may change from low to high temperature regimes. In this study, we use acid diffusion in a photopolymer as a model system where acid diffusion is necessary for the reaction but diffusion must be minimized to achieve high resolution patterns in lithography.[4]

Understanding the fundamental temperature dependence of acid diffusion in polymer matrices and acid catalyzed deprotection during photolithography is critical for photoresist design, especially as engineering resist systems capable of achieving sub-14nm dimensions has

[1] This Chapter has been submitted for peer review.

Lam Research Ex. 1013 - Page 91
Lam Research Corp. v. Inpria Corp.
IPR2025-00256 - U.S. Patent No. 11,537,048

become increasingly challenging. One key reason for this challenge is acid diffusion during the post-exposure bake step (PEB) required to complete the reaction underlying pattern formation.[5] While acid diffusion is crucial for these chemically amplified reactions, excessive acid diffusion leads to image blur and diminished patterning fidelity. In this work, we determined reaction rate and diffusivity during this PEB using laser induced heating.

Heating for many chemical reactions is most commonly performed on time scales from seconds to minutes. However heating times can be reduced using other techniques. For example, rapid thermal annealing (RTA) heats at rates up to 100 °C/s with temperature held for 5-12 seconds before cooling.[6] However, RTA is rarely used for organic materials such as polymers due to the temperature sensitivity of organic systems. If the time is shortened to the millisecond regime, as in laser spike annealing (LSA), polymers can withstand much higher temperatures, up to 800 °C for some molecules.[7] In recent work, LSA has been applied to the PEB process of conventional chemically amplified photoresists.[8] To achieve rapid heating and cooling, a focused continuous wave (CW) laser beam is scanned across thin film geometries. This technique allows us to explore the effects of competing processes with different activation energies at high temperature.

In this study, we designed three different photoresists based on a common polymer backbone with different acid labile groups to tune their deprotection activation energies. We also designed a large photoacid generator (PAG) molecule to lower the acid diffusivity and compared it with a more commonly used small PAG. The activation energies of deprotection and diffusion were measured separately and the apparent behavior of these two competing processes were demonstrated by evaluating the line width roughness using e-beam

Lam Research Ex. 1013 - Page 92
Lam Research Corp. v. Inpria Corp.
IPR2025-00256 - U.S. Patent No. 11,537,048

lithography. By correlating kinetic parameters with roughness, we not only gain an understanding of the high temperature kinetics of organic systems, but more importantly provide a path for the rational design of photoresist to meet new pattern formation challenges.

3.2. Results and discussion

3.2.1. Ultrafast laser spike annealing and temperature calibration

Laser induced heating is a useful tool in the study of reaction and diffusion kinetics over a broad temperature range. Previous studies by Jung *et al.* have shown that the stability of photoresists may be extended to 600 °C under 500 μs heating, compared to normal decomposition at ≈ 170 °C in TGA studies.[9] They later found that the deprotection in the high temperature regime is a first order reaction. NMR analysis was used to prove that a rate limiting byproduct forming reaction that occurred at low temperature was suppressed at high temperature, leading to a change in overall kinetics.[10] A continuous-wave CO_2 laser scans were used to induce transient millisecond heating in this study. Since the wavelength of CO_2 laser (λ =10.6 μm) falls in the free-carrier absorption regime, heavily doped Si substrates ($\rho \sim$ 0.01-0.02 Ω·cm) were used during laser spike annealing. The laser beam, focused to 90 μm by 700 μm Gaussian profiles, was scanned along its short axis with a step space of 110 μm. The local heating durations or dwells, controlled by laser scan velocity (20~2000 mm/s), ranged from 50 μs to 5000 μs.

3.2.2. The interplay of photopolymer and photoacid generator

Lam Research Ex. 1013 - Page 93
Lam Research Corp. v. Inpria Corp.
IPR2025-00256 - U.S. Patent No. 11,537,048

Photopolymers in general contain an acid labile group which can be thermally cleaved, but which can also be cleaved at lower temperature in the presence of acid.[11–13] For lithography, this acid arises from the decomposition of a photoacid generator (PAG), a small molecule which decomposes upon DUV exposure releasing a proton. Generally, PAGs are uniformly distributed in the photopolymer. During the PEB step, protons generated by UV exposure act as catalysts to cleave the acid labile group, in a process referred to as deprotection. After each deprotection event, a proton is regenerated, diffuses to the next reaction site and initiates a subsequent deprotection event. Thus one photogenerated acid can catalyze multiple deprotection events resulting in chemical amplification. This repeated chain of reactions and acid diffusion is critical to the deprotection step.

Both acid diffusion and the acid-catalyzed side chain deprotection are thermally activated processes expected to follow Arrhenius behavior, but with different activation energies. Hence the relative rate of diffusion and deprotection will change with temperature. An idea resist system should have should have a high deprotection activation energy so that the deprotection rate is fast enough to achieved desired deprotection extent within milliseconds. In order to suppress excessive diffusion with high temperature laser annealing, the ideal resist should also have a low diffusion activation energy so that the diffusivity only increase mildly at high temperature. For high-resolution resist patterning, the limited diffusion process is preferred as excessive acid diffusion leads to high value of line width roughness (LWR).

Lam Research Ex. 1013 - Page 94
Lam Research Corp. v. Inpria Corp.
IPR2025-00256 - U.S. Patent No. 11,537,048

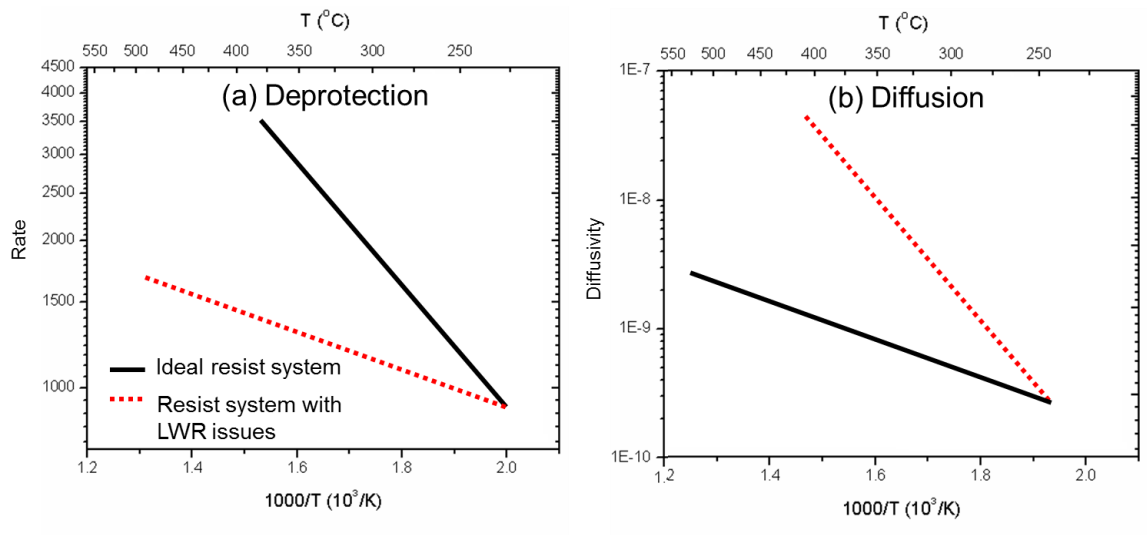

Figure 3.1 Schematic Arrhenius plot of idea resist system for laser spike annealing. Both deprotection rate and diffusivity increase with increasing temperature and the slopes are their activation energy. An idea resist system for laser PEB should have (a) a high deprotection activation energy and (b) a low diffusion activation energy.

In order to study the high temperature effects on deprotection, we synthesized several photoresists with a range of deprotection activation energies. Poly(hydroxystyrene) (PHS) of the same molecular weight was used as a backbone in all cases as it has been extensively studied for 248nm lithography[14] and can be potentially used in 13.5 nm (EUV) lithography.[15] Unlike methacrylate backbones used for 193nm lithography, PHS has the possibility to form both a carbonate and a carboxylate ester. The leaving groups were varied to cover a range of activation energies. Three different structures were built for this study using *tert*-butyl oxycarboxylate, *tert*-butyl methyloxycarboxylate, and methyl adamantane (referred to as *t*-BOC, *t*-BOCM, and AD respectively) as protecting groups (Figure 3.2). Photoresist *t*-BOC was chosen for its wide use in model chemically amplified photoresists over the past 20 years. The structure of *t*-BOCM is similar to t-BOC with the addition of a methylene group that

Lam Research Ex. 1013 - Page 95
Lam Research Corp. v. Inpria Corp.
IPR2025-00256 - U.S. Patent No. 11,537,048

separates the oxygen and carboxyl groups and decreases the electronegativity of the leaving group and increases the energy barrier to deprotection.[16] AD was chosen as an alternative protecting group containing a carboxylate ester, but the methyl adamantyl carbocation is less stable than the *t*-butyl carbocation increasing the stability of the leaving group and deprotection activation energy.

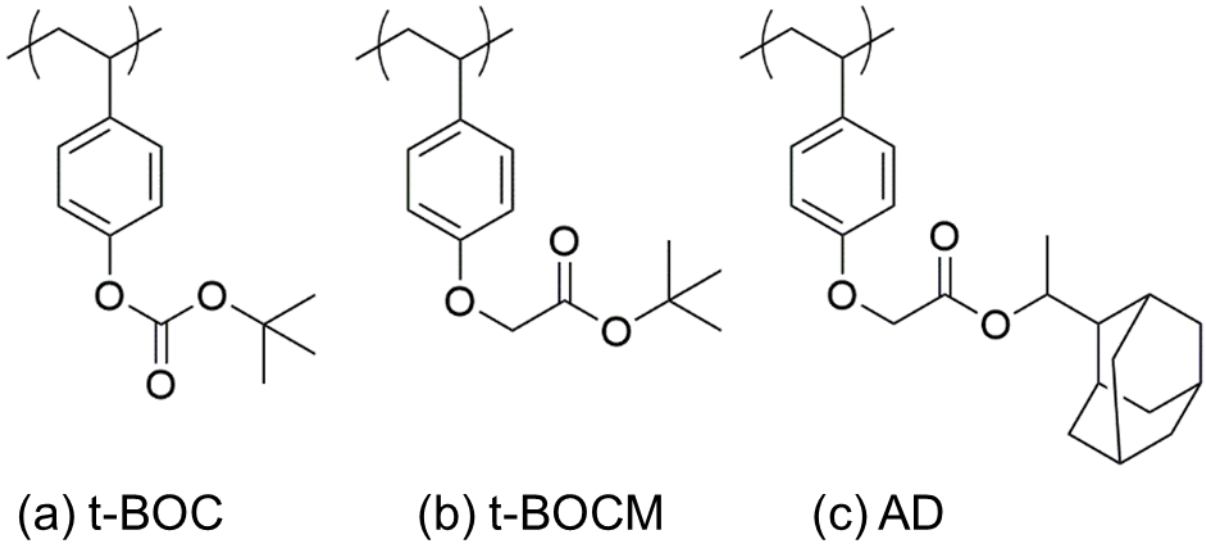

Figure 3.2. Chemical structures of the resists. The photoresists were built on the same molecular weight polyhydroxystyrene with selectively varied side chains.

The leaving groups can be cleaved from the backbone either thermally at high temperature or catalyzed by acid. There are two pathways for both thermolysis and acid-catalyzed deprotection: the *t*-butyl channel and the *t*-butoxy channel. These two pathways compete at different exposure and temperature conditions although the branching ratio is not known well.

Lam Research Ex. 1013 - Page 96
Lam Research Corp. v. Inpria Corp.
IPR2025-00256 - U.S. Patent No. 11,537,048

Depending on the protonation sites, the activation energy of acid deprotection reaction can be different between the two pathways.

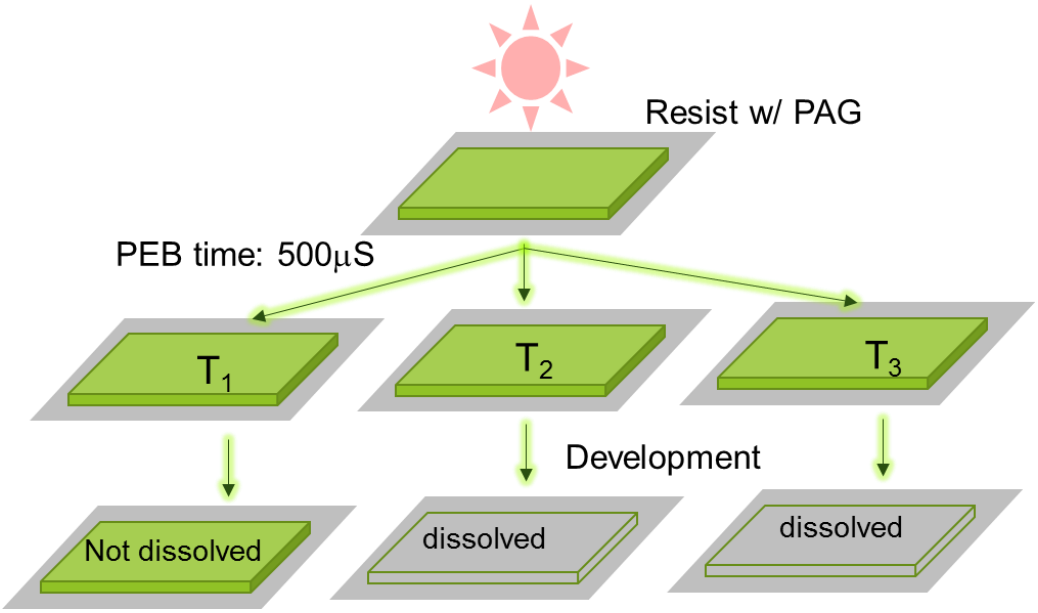

Figure 3.3 Method to determine the deprotection temperature at given reaction time. For thermolysis measurement, the resist film without PAG is scanned by a laser at a constant velocity but with increasing powers. For the acid deprotection measurement, the PAG containing resist is exposed to UV radiation at a fixed dose before laser PEB. As the peak temperature is increased, film transit from no dissolution to full dissolution in TMAH solution during development. The lowest temperature required for full development is recorded as a function of heating duration, yielding an Arrhenius plot of the reaction rate versus temperature.

The thermal stability of all three photoresists was investigated by measuring the resist film (without PAG) thickness remaining after laser heating and development. The cleavable side groups are expected to thermally deprotect before the backbone begins to decompose, resulting in a film thickness decrease due to thermolysis alone.

Lam Research Ex. 1013 - Page 97
Lam Research Corp. v. Inpria Corp.
IPR2025-00256 - U.S. Patent No. 11,537,048

The thermolysis kinetics were monitored by characterizing the dissolution of the photoresist after laser heating. As thermolysis reaches a critical level, the solubility of the polymer is altered sufficiently that it can be removed by a developer medium. At higher temperatures, shorter heating times are required to reach its solubility switch level (Figure 3.3). The effective reaction rate (1/dwell time) is plotted on an Arrhenius scale to determine the activation energy (Figure 3.4).

The activation energies for thermolysis are summarized in Table 3.1. We found that the relative thermolysis activation energy is consistent with predicted trend. AD and *t*-BOCM have higher thermolysis activation energies, 95 kJ/mol and 86 kJ/mol respectively, while *t*-BOC has lower thermolysis activation energy of 75 kJ/mol. We believe that the thermolysis activation energy is likely correlated with the acid deprotection activation energies since both thermolysis and acid deprotection share many elements of the reaction pathways.

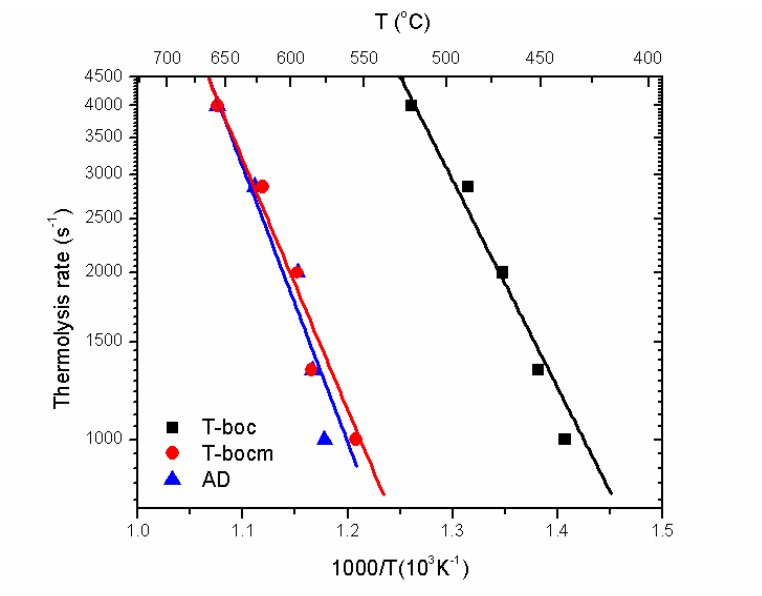

Figure 3.4. Arrhenius thermolysis plot of *t*-BOC, *t*-BOCM and AD under laser PEB.

Lam Research Ex. 1013 - Page 98
Lam Research Corp. v. Inpria Corp.
IPR2025-00256 - U.S. Patent No. 11,537,048

Two PAGs were also investigated, a conventional triphenyl sulfonium nonaflate (TPS-nf) as shown in Figure 3.5a and a synthesized large PAG molecule sodium 2-(4-{1,1-bis[4-(1,1,2,2-tetrafluoro-2-sulfinoethoxy)phenyl]ethyl}phenoxy)-1,1,2,2-tetrafluoroethane-1-sulfinate, referred to as 3P3A (Figure 3.5b). While, 3P3A utilized the same triphenylsulfonium (TPS) as the acid generating component, the counter ion, has three anions bounded to a single trisphenol core. To make the PAG more environmental friendly, the long fluorinated counter ions were partially replaced by phenol groups.[17] By increasing the total molecular weight of counter ions, acid diffusion should be more limited. The molecular weight per acid of the 3P3A was purposely chosen to be similar to TPS-nf. Consequently, a 5 wt. % of PAG loading resulting in the same amount of acid in the system. Quantum yield analysis also showed that both TPS-nf and 3P3A have similar acid yields from the same exposure dose in acetonitrile solution, thus confirming comparable initial concentration of acid-catalyst before laser PEB.

Lam Research Ex. 1013 - Page 99
Lam Research Corp. v. Inpria Corp.
IPR2025-00256 - U.S. Patent No. 11,537,048

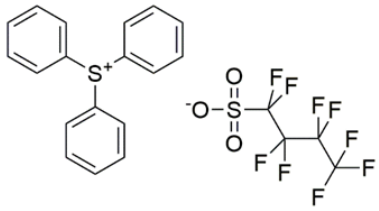

(a) TPS-nf

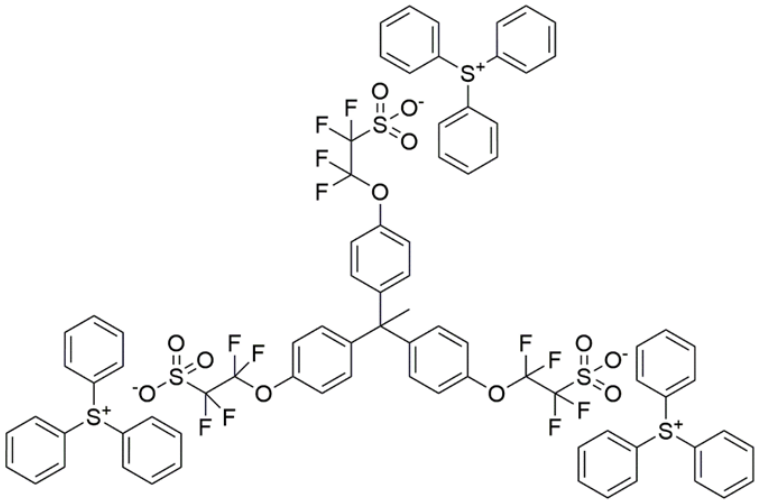

(b) 3P3A

Figure 3.5. Chemical structure of the PAGs. These two PAGs have same UV absorbing unit, the cation. TPS-nf is a common singe activation site 248 nm PAG with a fluorinated counter ion, while 3P3A has three activation sites with three counter ions bound to a molecular glass core.

3.2.3. Characterization of deprotection during millisecond PEB

During PEB, acid labile groups are cleaved from the polymer backbone, shifting the solubility of the polymer such that it can be dissolved in a developing medium such as tetramethylammonium hydroxide (TMAH) in water. Acids generated by UV decomposition of the PAG cations act as catalysts for this deprotection reaction. Acids attack the carbonyl group and are regenerated during stabilization of the reaction byproducts. Each photoacid can induce hundreds of deprotection reactions in the chemical amplification process.

Lam Research Ex. 1013 - Page 100
Lam Research Corp. v. Inpria Corp.
IPR2025-00256 - U.S. Patent No. 11,537,048

The acid deprotection kinetics were measured using the method described in Scheme 1. The acid deprotection rate is plotted on an Arrhenius scale versus inverse temperature to determine the deprotection activation energy, as shown in Figure 3.6. The deprotection activation energies of three resists with TPS-nf was summarized in Table 3.1 The deprotection and diffusion activation energy of the resist systems.

Photoresist *t*-BOC, *t*-BOCM and AD samples with 5 wt. % TPS-nf loading were exposed at dose of 3.4 mJ/cm^2 and deprotection activation energies were extracted from Figure 3.6. This UV dose was chosen to remain in the dilute acid regime (14% PAG decomposes). As summarized in Table 1, deprotection activation energies for *t*-BOC, *t*-BOCM and AD are 58±8, 72±5, and 83±8 kJ/mol respectively. Compared to thermolysis, the presence of acid lowered the bond breaking activation energy of carboxylate ester by 20 kJ/mol and that of the carbonate ester by 12 kJ/mol. As we anticipated, the resist system with the AD protecting group showed the highest deprotection activation energy and could be among the most promising candidates for laser PEB.

Lam Research Ex. 1013 - Page 101
Lam Research Corp. v. Inpria Corp.
IPR2025-00256 - U.S. Patent No. 11,537,048

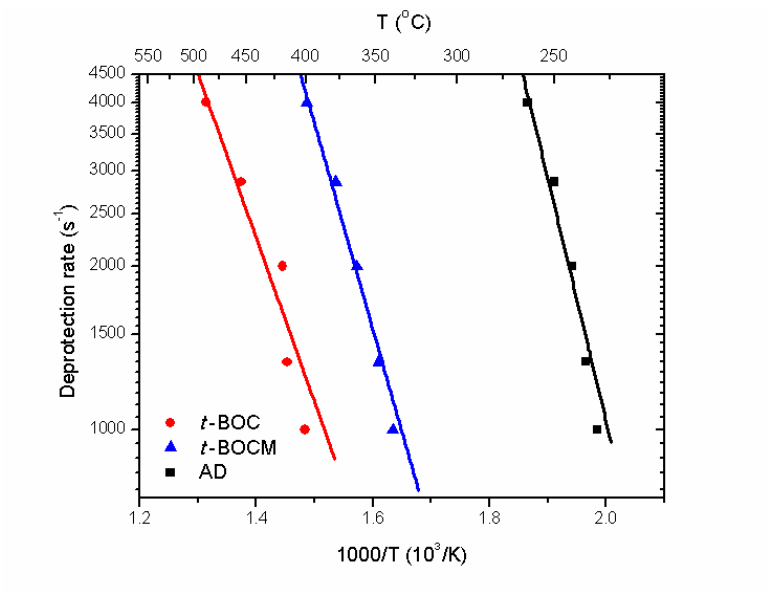

Figure 3.6. Arrhenius deprotection plot of *t*-BOC, *t*-BOCM and AD under laser PEB. The resists were loaded with 5 wt. % TPS-nf and exposed at 248 nm for 3.4 mJ/cm^2.

Table 3.1 The deprotection and diffusion activation energies of the resist systems. Activation energies are given in kJ/mol.

Resist	Thermolysis (w/o PAG)	PAG	Deprotection	Diffusion
t-BOC	77±7	TPS-nf	58±8	400±80
t-BOCM	86±9	TPS-nf	72±5	302±6
AD	95±10	TPS-nf	83±8	280±57
AD	95±10	3P3A	83±8	195±10

*PAG loading for all the systems was 5 wt. % of the solid. *t*-BOC and *t*-BOCM films with TPS-nf were exposed at 3.4 mJ/cm^2, while the AD films with TPS-nf and 3P3A were exposed at 3.4, 6.8 and 17.7 mJ/cm^2. Uncertainty in deprotection activation energies where listed, and are the standard deviation of multiple measurements obtained at various doses.

Lam Research Ex. 1013 - Page 102
Lam Research Corp. v. Inpria Corp.
IPR2025-00256 - U.S. Patent No. 11,537,048

We varied the exposure dose to study the effects of the initial acid concentration. The deprotection rate, (proportional to 1/dwell) of the AD resist with TPS-nf PAG was investigated as a function of temperature at three different UV doses as shown in Figure 3.7. As the UV exposure dose increased from 3.4 mJ/cm^2 to 17.1 mJ/cm^2, the initial acid concentration level was calculated to increase from 14% to 53% of the total PAG loading by using Dill's equation.[147,148] When the acid concentration was doubled (14% at 3.4 mJ/cm^2, 25.3% at 6.8 mJ/cm^2 and 53% at 17.7 mJ/cm^2), the deprotection rate increased by 4 times for TPS-nf. However, the deprotection activation energy was especially independent of the exposure dose.

We also performed deprotection studies of AD with 5 wt. % 3P3A loading. Similar to AD with TPS-nf, we observed that the absolute rate increased with increases in the initial acid concentration but the deprotection activation energy changed by only 6% over a factor of 3 in exposure dose.

Comparing two different PAGs in the same resist matrix, the deprotection rate varies enormously despite similar deprotection activation energies. The activation energy extracted from the Arrhenius equation represents the energy barrier to reach a metastable state. Consequently, it is primarily related to the resist chemistry and, since AD is the common resist matrix, the activation energy is not expected to vary significantly at different exposure doses or for different PAG species, as observed.

Lam Research Ex. 1013 - Page 103
Lam Research Corp. v. Inpria Corp.
IPR2025-00256 - U.S. Patent No. 11,537,048

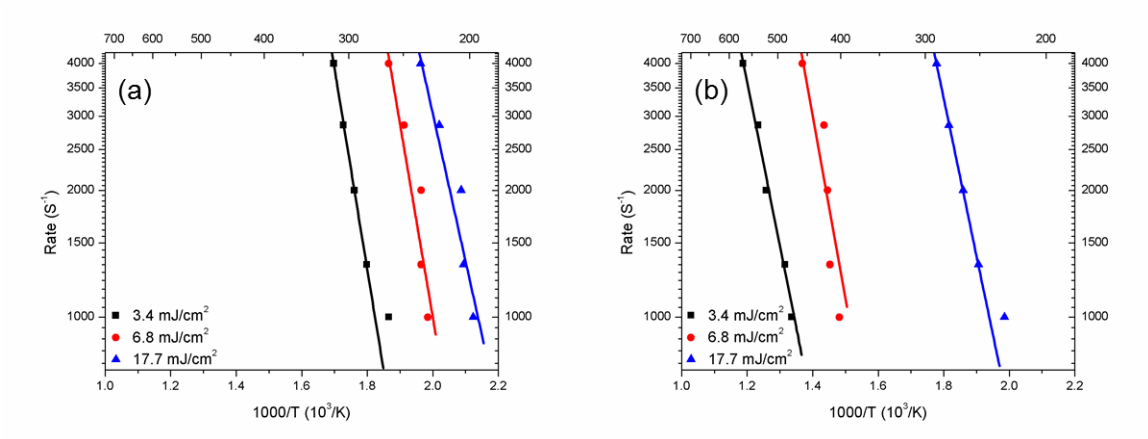

Figure 3.7. Arrhenius deprotection plot of AD with (a) TPS-nf and (b) 3P3A at three doses under laser PEB. At lower dose, fewer acids are generated and hence higher temperature are required to increase the diffusion to complete the deprotection within given annealing time. However, the deprotection activation energy is primarily dependent on the resist chemistry and only weakly dependent on UV dose or PAG molecule.

3.2.4. Characterization of acid diffusivity

During UV pattering, a large gradient in acid concentration is generated at pattern edges. Acids in the exposed areas can diffuse laterally into unexposed area through a random walk process, leading to resist blur and line edge roughness. A resist bilayer structure was used to quantify this acid diffusion.[20,21] The top layer consisted of a PAG-containing resist, while the bottom layer was PAG-free using an equivalent resist resin. The bilayers were flood exposed to generate acids in the surface layer. During PEB, deprotection and the resulting solubility change should only occur only within the PAG-containing top layer; however as acids diffuse to the PAG-free bottom layer and induce deprotection, part of bottom layer near the interface also become soluble. After development, thickness loss of the bottom layer was measured to

Lam Research Ex. 1013 - Page 104
Lam Research Corp. v. Inpria Corp.
IPR2025-00256 - U.S. Patent No. 11,537,048

determine the acid diffusion length and the effective diffusivity at different laser annealing temperatures.

The acid diffusivity of TPS-nf in AD, *t*-BOC and *t*-BOCM are plotted as a function of inverse temperature in Figure 3.8, with their activation energies were determined and are summarized in Table 3.2. The highest diffusion activation energy was observed in *t*-BOC while AD exhibited the lowest.

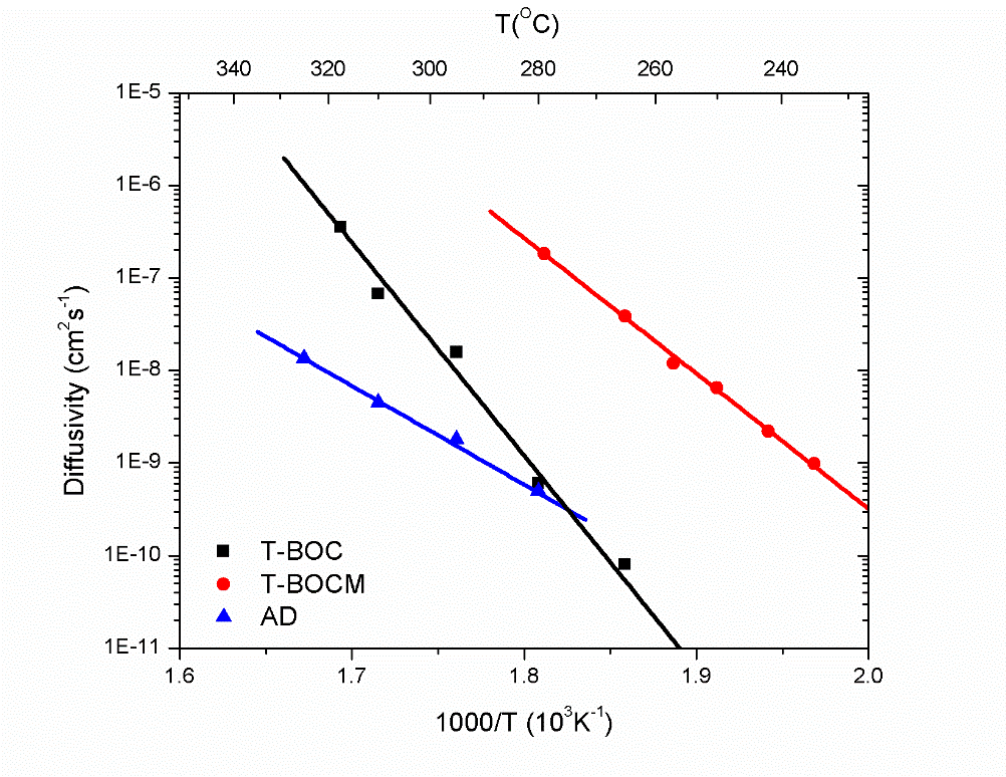

Figure 3.8. Arrhenius plot of acid diffusivity, determined with bilayer technique, of TPS-nf in three resist resins *t*-BOC, *t*-BOCM and AD under laser PEB. The resist film was flood exposed at 248 nm for 34 mJ/cm^2, activating 90% of the PAG.

Lam Research Ex. 1013 - Page 105
Lam Research Corp. v. Inpria Corp.
IPR2025-00256 - U.S. Patent No. 11,537,048

Hopping of the acids in the resist matrix is considered the principle proton transport mechanism during PEB. Therefore, acid transport is strongly dependent on concentration, the dynamic free volume, and acid trapping mechanisms.[22] In the *t*-BOC system, for example, the film density doubles after PEB due to the evaporation of volatile byproducts including carbon dioxide and isobutylene.[23] The increased film density reduces acid transport in the deprotected *t*-BOC matrix. In contrast, non-volatile byproducts such as methylene adamantine are formed by the deprotection of AD leading to minimal changes in film density during PEB. However, these remaining byproducts may act as a plasticizers, decreasing the energy barrier for acid diffusion.

Ultimately, the diffusivity of the proton is closely related to the diffusivity of the counter ions as they must diffuse in the resist resin as a pair to maintain local charge neutrality. Previous reports have shown that attaching the anion to the polymer backbone greatly reduces the acid diffusion length.[24] Our result similarly shows that anchoring three anions to a trisphenol core is effective in reducing the acid diffusivity (Figure 3.9).

Lam Research Ex. 1013 - Page 106
Lam Research Corp. v. Inpria Corp.
IPR2025-00256 - U.S. Patent No. 11,537,048

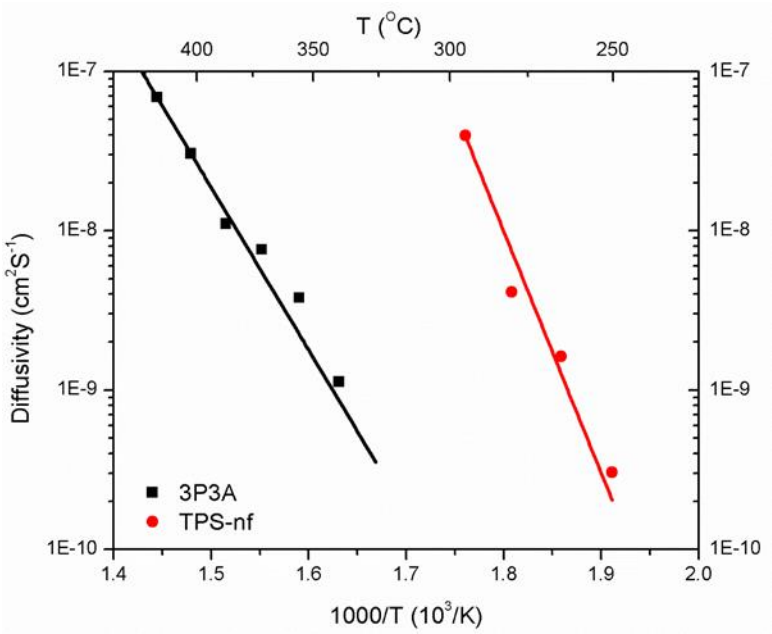

Figure 3.9. Arrhenius plot of acid diffusivity of TPS-nf and 3P3A in AD resist resin under laser PEB. The resist film was flood exposed at 248 nm for 34 mJ/cm^2.

3.2.5. E-beam pattering and line width roughness of the resists

The deprotection and diffusion of an exposed resist at the exposure edge can be quantified as the latent image log slope (LILS), which is inversely proportional to the LER.[25] LILS is affected by the acid diffusivity, the deprotection rate, and the initial acid concentration. High diffusivity leads to faster broadening of the reaction-diffusion front. In contrast, high deprotection rates not only kinetically trap acid but also modify resist polarity making diffusion more difficult.[26] Previous studies have found that within 1.2 nm of the interface, there is a highly deprotected region where the acids are kinetically trapped. Beyond this 1.2 nm zone, the acid concentration decreases to a level that the extent of deprotection is at or below the polarity switch. This long-distance deprotection is a main source of roughness. The

Lam Research Ex. 1013 - Page 107
Lam Research Corp. v. Inpria Corp.
IPR2025-00256 - U.S. Patent No. 11,537,048

extent of reaction is also strongly affected by the local acid concentration, as high initial acid concentration can induce more deprotection reactions.

Much like DUV radiation, electron beam radiation can also be used to activate and decompose PAGs. Despite reports that both deprotection and crosslinking of PHS occurs during e-beam exposure, the overall mechanism for acid-catalyzed deprotection by e-beam radiation is believed to be comparable to that produced by DUV exposure.[27] In a previous section, we reported the deprotection and diffusion behavior of selected resist and PAG systems using 254 nm exposure. In order to create a sharp acid concentration gradient and evaluate how deprotection and diffusion affects LILS and LWR, we used electron beam exposure to pattern the resists. SEM images of e-beam patterning using three resists with TPS-nf are shown in Figure 3.10 a-f and their patterning results are summarized in Table 3.2.

Each image represents the highest resolution that was achieved under given PEB conditions. Under hotplate annealing, resolution of the *t*-BOC and *t*-BOCM systems was approximately 100nm and 150nm respectively with an LWR of approximately 10nm. Under laser PEB, the resolution was 200 nm and 300 nm with LWR of 35 nm and 21 nm, respectively. We believe the increase of LWR and the failure of sub-200nm patterning is due to the accelerated acid diffusion at high temperature resulting from the high diffusion activation energy. As diffusion increases, LILS decreases and LWR becomes worse.

In contrast, AD with its high deprotection activation energy maintains a high resolution with a slight decrease in LWR during laser PEB. This is a result of maintaining the ratio of

Lam Research Ex. 1013 - Page 108
Lam Research Corp. v. Inpria Corp.
IPR2025-00256 - U.S. Patent No. 11,537,048

deprotection rate and diffusivity at high temperature. Therefore, the AD resist was further optimized to achieve better patterning results using laser PEB.

Table 3.2. Patterning conditions and results using e-beam lithography.

	Resist	PAG	Hotplate (115 °C 60 s)			Laser (500 μs)		
			Dose	CD	LWR	Dose	CD	LWR
a	*t*-BOC	TPS-nf	15	98.9	9.8	20	203.5	35
c	*t*-BOCM	TPS-nf	70	141.0	9.7	70	282.0	21.3
e	AD	TPS-nf	45	248.5	16.5	45	141.0	14.2
g	AD*	TPS-nf	30	221.6	20	60	215.9	8.67
i	AD	3P3A	120	106.4	10.2	120	123.2	3.46

*The PEB laser power for conditions was at 20W (295 °C), except h at 18W (265 °C). The units for dose, CD and LWR are $\mu C/cm^2$, nm and nm respectively.

Lam Research Ex. 1013 - Page 109
Lam Research Corp. v. Inpria Corp.
IPR2025-00256 - U.S. Patent No. 11,537,048

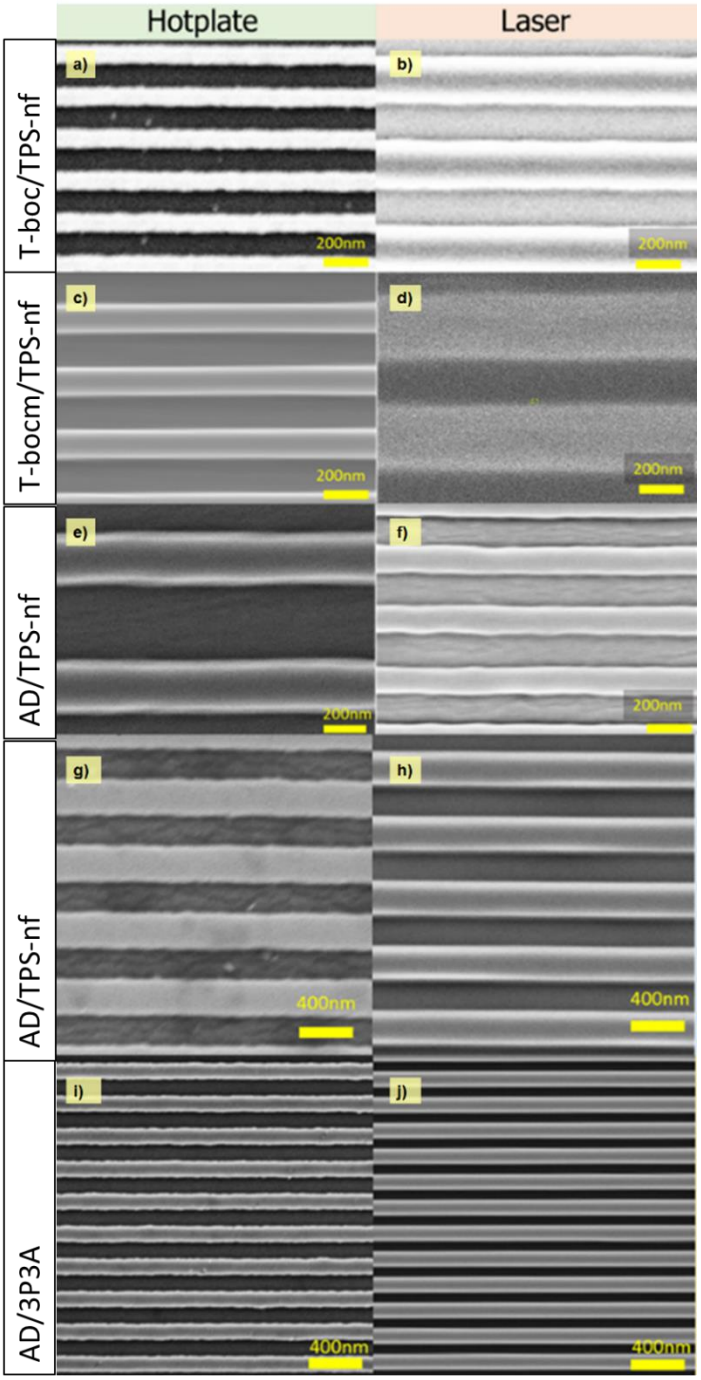

Figure 3.10. SEM images of e-beam lithography showing the highest resolution obtained under each condition. Images on the left are under hotplate PEB and images on the right are under laser PEB. Patterning condition and results are summarized in Table 3.2.

Lam Research Ex. 1013 - Page 110
Lam Research Corp. v. Inpria Corp.
IPR2025-00256 - U.S. Patent No. 11,537,048

Mixed with AD, both TPS-nf and 3P3A demonstrated reduced line width roughness using laser PEB as seen in Figure 3.10 g-j. The roughness of patterns using TPS-nf in AD is further reduced at 265 °C compared to 295 °C, but requires a higher UV dose. When the dose is fixed for AD with 3P3A, a 60% reduction in roughness is achieved using laser PEB compared to conventional PEB at 115 °C. Due to the low acid diffusivity and low diffusion activation energy, the acid generated upon exposure is mostly limited to the local area and a much higher dose is required in order to achieve the same extent of deprotection. While 3P3A has the lowest diffusivity, its diffusion activation energy is also low. Consequently, the diffusivity changes slowly with the increasing temperature during laser annealing. But the photopolymer AD has high deprotection activation energy which leads to the fast increase in the deprotection rate. Therefore LILS increases and the LWR is reduced by using laser PEB.

3.3. Conclusions

Photopolymer side chain cleavage accompanied by acid diffusion was studied as a model system. We used laser PEB to explore the high temperature effects of simultaneous competing processes with different activation energies. We synthesized three different photopolymers with different protecting groups to tune the activation energy, and a PAG with a large anion to investigate the effects of molecular size on diffusion. The deprotection-activation and diffusion-activation energies were measured and correlated to the line width roughness during e-beam patterning. Resist systems with a high deprotection activation energy and low diffusion activation energy showed the best line width roughness under laser PEB, confirming that deprotection dominates at high temperature. AD with 3P3A is the best performing combination where a 60% reduction in edge roughness was achieved when compared to the

Lam Research Ex. 1013 - Page 111
Lam Research Corp. v. Inpria Corp.
IPR2025-00256 - U.S. Patent No. 11,537,048

conventional PEB conditions at a constant UV exposure dose. This work not only demonstrates how the activation energy impacts simultaneously competing processes at high temperature, but it also provides a theory for resist design to meet the semiconductor roadmap challenges. For a resist system to show improvement under laser PEB, it must have a high deprotection activation energy and low diffusion activation energy to suppress the excessive acid diffusion at the laser-induced high temperatures. These results also demonstrate the potential in patterning performance using laser PEB, where resist systems with the appropriate activation characteristics can surpass the imaging achieved using conventional PEB methods.

3.4. Materials and methods

3.4.1. Materials and reagent

Polyhydroxystyrene (8 kg mol^{-1}), propylene glycol methyl ether acetate (PGMEA), hexamethyldisilazane (HDMS), triphenylsulfonium perfluoro-1-butanesufonate (TPS-nf), di-tert-butyl dicarbonate, tert-Butyl bromoacetate, were purchased from Sigma Aldrich and used without further purification. Ethyl acetate, actone, tetrahydrofuran, hexanes and toluene used in these reactions were HPLC grade from Fisher Scientific and used as received. Developer solution (0.26 N tetramethyl ammonium hydroxide in water, TMAH) was from AZ electronic materials. 2-methyl-2-adamantyl bromoacetate was a gift obtained from Idemitsu Chemicals U.S.A. Corporation.

3.4.2. Synthesis

Synthesis of Poly(4-(2-methyl-2-adamantyloxycarbonylmethoxy)styene-co-4-hydroxystyrene)

Lam Research Ex. 1013 - Page 112
Lam Research Corp. v. Inpria Corp.
IPR2025-00256 - U.S. Patent No. 11,537,048

2-methyl-2-adamantyl bromoacetate (1.67 g, 5.8 mmol), poly(4-vinylphenol) (1 g, 0.11 mmol) and potassium carbonate (0.8 g, 6.8mmol) were dissolved in THF (30 mL). The mixture was heated to 66℃ and refluxed for 19 hrs. After cooling to room temperature, mixture was filtered and evaporated under reduced pressure. The resulting powder was purified by silica gel column chromatography with the mixture of ethyl acetate and hexane. The resulting powder was dried at 60℃ overnight under reduced pressure.

Synthesis of Poly(4-t-butyloxycarbonylmethoxystyrene -co-4-hydroxystyrene)

tert-butyl bromoacetate (1.3 g, 6.67 mmol), poly(4-vinylphenol) (1 g, 0.125 mmol) and potassium carbonate (0.92 g, 6.67mmol) were the initial reactants. The synthesis method is similar to that for AD.

Synthesis of poly (4-t-butyloxycarbonyloxystyrene-co-4-hydroxystyrene)

The di-*tert*-butyl dicarbonate (0.64g, 2.1mmol) and dimethylaminopyridine (DMAP) (0.048g, 0.4mmol) were added to a solution of poly(4-hydroxystyrene) (1 g, 0.11 mmol) in dry acetone. The solution was stirred at room temperature overnight and partitioned between ethyl acetate, brine and 1 N HCl. The layers were separated and the organic layer was washed with aqueous $NaHCO_3$, dried in Mg_2SO_4, and concentrated. The solvent was then evaporated and dried in a vacuum oven at 50℃ overnight. 70% protection rate was achieved.

Synthesis of

sodium 2-(4-{1,1-bis[4-(1,1,2,2-tetrafluoro-2-sulfinoethoxy)phenyl]ethyl}phenoxy)-1,1,2,2-tetrafluoroethane-1-sulfinate (3P3A)

Lam Research Ex. 1013 - Page 113
Lam Research Corp. v. Inpria Corp.
IPR2025-00256 - U.S. Patent No. 11,537,048

The synthesis method is modified from Ramakrishnan Ayothi[17]. The method of synthesizing 2-Phenoxytetrafluoroethanesulfonate was used to synthesize 3P3A. 1,1,1-Tris(4-hydroxyphenyl)ethane Triphenylsulfonium was used as starting materials instead of phenol.

3.4.3. Methods

^{1}H and ^{19}F nuclear magnetic resonance (NMR) was performed in an INOVA400 spectrometer in Cornell NMR facility at room temperature. Spectra recorded in $(CD_3)_2CO$ were referenced to internal tetramethylsilane (0 ppm) for proton spectra and to CF_3COOH (76.55 ppm) for fluorine spectra. Thermal analysis was performed in a TA instrument Q500 thermal gravimetric analyzer (TGA) at the heating rate of 10 °C/min under N_2 and a Q1000 differential scanning calorimeter (DSC) at a ramp of 10 °C/min under N_2.

5 wt. % triphenylsulfonium perfluoro-1-butanesufonate (TPS-nf) or 3P3A was added to the photoresists and dissolved in propylene glycol methyl ether acetate (PGMEA). Films were spun coated onto HDMS primed wafer. The target thickness was 100 nm for DUV and E-beam exposure. The films were subjected to a post-apply bake at110 °C for 60s. DUV exposure (λ = 254 nm) was carried out using ABM contact aligner and e-beam patterning was carried out using JEOL 6300. The accelerating voltage was 100 KV with a beam current of 250 pA. After the post-exposure bake by hotplate or laser spike annealing, films were developed in 0.26 N TMAH solution for 60 s.

Film thickness was determined using a F50-EXR filmmetrics measurement system.

Lam Research Ex. 1013 - Page 114
Lam Research Corp. v. Inpria Corp.
IPR2025-00256 - U.S. Patent No. 11,537,048

Images were taken using a Zeiss Ultra scanning electron microscope (SEM) with lines parallel to the scanning direction. The resist samples were coated with a layer of Au/Pd to prevent charging. Line edge roughness (LER) and line width roughness (LWR) was calculated using SuMMIT image analysis software (EUV technology, Martinez, CA).

3.4.4. Heat treatment

After exposure to UV radiation or E-beam, resists were subjected to PEB heat treatment. Two types of treatment were used: hotplate annealing and laser heating. For hotplate annealing, wafers were placed on an isothermal hotplate in air. For laser heating, wafers were annealed using multiple laser scans of a focused CW laser in order to achieve uniformity. A CO_2 laser operating at 10.6 μm was used and the dwell time was adjusted by the scan velocity. For the reaction kinetic experiments, dwell time ranged from 250 μs to 1000 μs. The peak temperature of the laser PEB at the wafer surface is a function of both dwell and power, which were calibrated using thermistors and known Au melt and Si melt reference points [9,10].

ACKNOWLEDGMENT

We gratefully acknowledge GlobalFoundries (Kenji Yoshimoto and Deniz Civay) for helpful discussions and critical assistance. This work used of facilities in the Cornell Center for Materials Research (NSF-DMR 0520404), and in the Cornell Nanoscale Facility (NSF-ECS 0335765). Work at Cornell was supported by GlobalFoundries through the Semiconductor Research Corporation (Task IDs: 2137.001, 2137.002).

Reference

Lam Research Ex. 1013 - Page 115
Lam Research Corp. v. Inpria Corp.
IPR2025-00256 - U.S. Patent No. 11,537,048

(1) Pei, Q.; Yang, Y.; Yu, G.; Zhang, C.; Heeger, A. J. Polymer Light-Emitting Electrochemical Cells : In Situ Formation of a Light-Emitting P - N Junction. 1996, 3922–3929.

(2) Jaouen, F.; Lindbergh, G.; Sundholm, G. Investigation of Mass-Transport Limitations in the Solid Polymer Fuel Cell Cathode. *J. Electrochem. Soc.* 2002, *149*, A437.

(3) Schlegel, L.; Ueno, T.; Hayashi, N.; Iwayanagi, T. Determination of Acid Diffusion in Chemical Amplification Positive Deep Ultraviolet Resists. *J. Vac. Sci. Technol. B Microelectron. Nanom. Struct.* 1991, *9*, 278–289.

(4) Lin, E. K.; Soles, C. L.; Goldfarb, D. L.; Trinque, B. C.; Burns, S. D.; Jones, R. L.; Lenhart, J. L.; Angelopoulos, M.; Willson, C. G.; Satija, S. K.; *et al.* Direct Measurement of the Reaction Front in Chemically Amplified Photoresists. *Science* 2002, *297*, 372–375.

(5) Hinsberg, W. D.; Houle, F. a.; Sanchez, M. I.; Wallraff, G. M. Chemical and Physical Aspects of the Post-Exposure Baking Process Used for Positive-Tone Chemically Amplified Resists. *IBM J. Res. Dev.* 2001, *45*, 667–682.

(6) Narayan, J.; Holland, O. W.; Eby, R. E.; Wortman, J. J.; Ozguz, V.; Rozgonyi, G. A. Rapid Thermal Annealing of Arsenic and Boron-Implanted Silicon. *Appl. Phys. Lett.* 1983, *43*, 957–959.

(7) Jung, B. Laser-Induced Millisecond Heating of Polymers and Small Molecules for Pattern Development. Ph.D. Dissertation, Cornell University, Ithaca, NY, 2014.

(8) Sha, J.; Jung, B.; Thompson, M. O.; Ober, C. K.; Chandhok, M.; Younkin, T. R. Submillisecond Post-Exposure Bake of Chemically Amplified Resists by CO2 Laser Spike Annealing. *J. Vac. Sci. Technol. B* 2009, *27*, 3020–3024.

(9) Jung, B.; Sha, J.; Paredes, F.; Chandhok, M.; Younkin, T. R.; Wiesner, U.; Ober, C. K.; Thompson, M. O. Kinetic Rates of Thermal Transformations and Diffusion in Polymer Systems Measured during Sub-Millisecond Laser-Induced Heating. *ACS Nano* 2012, *6*, 5830–5836.

(10) Jung, B.; Satish, P.; Bunck, D. N.; Dichtel, W. R.; Ober, C. K.; Thompson, M. O. Laser-Induced Sub-Millisecond Heating Reveals Distinct Tertiary Ester Cleavage Reaction Pathways in a Photolithographic Resist Polymer. *ACS Nano* 2014, *8*, 5746–5756.

(11) Ichikawa, R.; Hata, M.; Okimoto, N.; Oikawa-Handa, S.; Tsuda, M. Acid-Catalyzed Deprotection Mechanism of Tert-Butyloxycarbonyloxy Polymers in Chemically Amplified Resists. *J. Polym. Sci. Part A Polym. Chem.* 1998, *36*, 1035–1042.

Lam Research Ex. 1013 - Page 116
Lam Research Corp. v. Inpria Corp.
IPR2025-00256 - U.S. Patent No. 11,537,048

(12) Ito, H.; Sherwood, M. NMR Analysis of Chemically Amplified Resist Films. 1999, *3678*, 104–115.

(13) Houle, F. A.; Poliskie, G. M.; Hinsberg, W. D.; Pearson, D.; Sanchez, M. I.; Ito, H.; Hoffnagle, J. A. Real-Time Analysis of Volatiles Formed during Processing of a Chemically Amplified Resist. *Proc. SPIE*, 2000, *3999*, 181–187.

(14) Reichmanis, E.; Houlihan, F. M.; Nalamasu, O.; Neenan, T. X.; Laboratories, T. B.; Hill, M. Chemical Amplification Mechanisms for Microlithography. 1994.

(15) Weiqiang Wu, Kirill Nuzhdin, Mariya Vyushkova, Ireneusz Janik, and D. B. Comparison of Acid Generation in EUV Lithography Films of Poly(4-Hydroxystyrene) (PHS) and Noria Adamantyl Ester (Noria-AD50). *The Journal of Physical Chemistry B*, 2012, 6215.

(16) MacDonald, S. A.; Willson, C. G.; Frechet, J. M. J.; Macdonald, A.; Grant, C.; Frechets, M. J. Chemical Amplification in High-Resolution Imaging Systems. *Acc. Chem. Res.* 1994, *27*, 151–158.

(17) Ayothi, R.; Yi; Cao, H. B.; Yueh, W.; Putna, S.; Ober, C. K. Arylonium Photoacid Generators Containing Environmentally Compatible Aryloxyperfluoroalkanesulfonate Groups. *Chem. Mater.* 2007, *19*, 1434–1444.

(18) Dill, F. H.; Hornberger, W. P.; Hauge, P. S.; Shaw, J. M. Characterization of Positive Photoresist. *Electron Devices, IEEE Trans.* 1975, *22*, 445–452.

(19) Perera, G. M.; Pandey, Y. N.; Patil, A. a.; Stein, G. E.; Doxastakis, M. Reaction Kinetics in Acid-Catalyzed Deprotection of Polymer Films. *J. Phys. Chem. C* 2012, *116*, 24706–24716.

(20) Schlegel, L.; Ueno, T.; Hayashi, N.; Iwayanagi, T. Determination of Acid Diffusion in Chemical Amplification Positive Deep Ultraviolet Resists. *Jpn. J. Appl. Phys.* 1991, *9*, 278–289.

(21) Kang, S. H.; Wu, W. L.; Choi, K. W.; De Silva, A.; Ober, C. K.; Prabhu, V. M. Characterization of the Photoacid Diffusion Length and Reaction Kinetics in EUV Photoresists with IR Spectroscopy. *Macromolecules* 2010, *43*, 4275–4286.

(22) Stewart, M. D.; Tran, H. V.; Schmid, G. M.; Stachowiak, T. B.; Becker, D. J.; Willson, C. G. Acid Catalyst Mobility in Resist Resins. *J. Vac. Sci. Technol. B Microelectron. Nanom. Struct.* 2002, *20*, 2946–2952.

(23) Stewart, M. D.; Somervell, M. H.; Tran, H. V; Postnikov, S. V; Willson, C. G. Study of Acid Transport Using IR Spectroscopy and SEM. *Adv. Resist Technol. Process. XVII* 2000, *3999*, 665–674.

Lam Research Ex. 1013 - Page 117
Lam Research Corp. v. Inpria Corp.
IPR2025-00256 - U.S. Patent No. 11,537,048

(24) Wang, M. X.; Jarnagin, N. D.; Lee, C. T.; Henderson, C. L.; Yueh, W.; Roberts, J. M.; Gonsalves, K. E. Novel Polymeric Anionic Photoacid Generators (PAGs) and Corresponding Polymers for 193 Nm Lithography. *J. Mater. Chem.* 2006, *16*, 3701–3707.

(25) Prabhu, V. M.; Kang, S.; VanderHart, D. L.; Satija, S. K.; Lin, E. K.; Wu, W. Photoresist Latent and Developer Images as Probed by Neutron Reflectivity Methods. *Adv. Mater.* 2011, *23*, 388–408.

(26) Croffie, E.; Cheng, M.; Neureuther, A. Moving Boundary Transport Model for Acid Diffusion in Chemically Amplified Resists. *J. Vac. Sci. Technol. B* 1999, *17*.

(27) Enomoto, S.; Oshima, A.; Tagawa, S. Reaction Mechanisms of Various Chemically Amplified EUV and EB Resist. 2013, *8679*, 86792C.

Lam Research Ex. 1013 - Page 118
Lam Research Corp. v. Inpria Corp.
IPR2025-00256 - U.S. Patent No. 11,537,048

CHAPTER 4 ULTRAFAST SELF-ASSEMBLY OF SUB-10 NM BLOCK COPOLYMER NANOSTRUCTURES BY SOLVENT-FREE LASER ANNEALING AT HIGH TEMPERATURE

ABSTRACT

Laser annealing for 3-20 millisecond dwells was applied to polystyrene-*block*-polydimethylsiloxane (PS-*b*-PDMS) to enhance microphase separation. The extent of ordering increased with temperature and annealing time while contrast between two blocks was lost for shorter annealing times at high temperature. Various polymers were used as surface modification to study the influence of surface chemistry in the BCP ordering. Among these polymers, poly(methyl methacrylate) (PMMA) improved ordering under the equivalent laser annealing conditions. Long range ordered sub-10 nm cylindrical morphology was achieved by combining graphoepitaxy with laser annealing at 440 °C for only a 20 ms dwell.

4.1. Introduction

Block copolymers (BCP) can self-assemble into nanoscale domains with various morphologies including spheres, cyliners and lamellae. By modifying substrate chemistry or geometry with appropriate periodicity and arrangement, and applying an external driving force, BCPs can develop dense repetitive structures with long range order, such as hexagonal dots or parallel line space patterns of lamellae or cylinders and even more complex structures including jogs, T-junctions or blends.[1–5] Because of these capabilities and low cost, directed

Lam Research Ex. 1013 - Page 119
Lam Research Corp. v. Inpria Corp.
IPR2025-00256 - U.S. Patent No. 11,537,048

self-assembly of block copolymers [2]has been extenseively studied for numerous applications including lithography,[6–8] organic photovoltaics,[9,10] membranes[11–13] and controlled drug delivery.[14–16] Especially in the semiconductor industry, directed self-assembly (DSA) has been studied for high volume manufacturing as an alternative method to achieve sub-20 nm features.[17] High resolution patterns require BCPs with low molecular weights and high χ values. Polystyrene-*block*-polydimethylsiloxane (PS-*b*-PDMS) is a so-called high χ material, with a χ around 0.26, which is much larger than the current widely studied polystyrene-b-poly(methyl methacrylate) (PS-*b*-PMMA) ($\chi \sim 0.06$ at room temperature).[18–20]

Although BCP thermodynamically prefer to phase separate, the ordering process does not occur at an appreciable speed at room temperature. Even using solvent vapors to increase chain mobility[21,22] still requires hours to form ordered structures, while elevated temperatures in conventional thermal annealing processes may easily approach the thermal degradation limits.[23] Rapid thermal annealing of BCP has been studied by using microwave radiation [24,25] and rapid thermal processing furnace.[26] More recently, ultrafast laser induced heating has been used in BCP self-assembly. Order-order transition of PS-*b*-PDMS was observed in the presence of solvent vapor by laser annealing in the ten-millisecond regime, yet no long range order was achieved. [27] Uniformly aligned PS-*b*-PMMA was achieved in the absence of solvent vapor by laser annealing in the hundred-millisecond time frame.[28] In this paper, we will demonstrate millisecond laser spike annealing of PS-*b*-PDMS in the absence of solvent vapor. The influences of laser annealing temperature and dwell times as well as substrate

[2] This Chapter has been submitted for peer review.

Lam Research Ex. 1013 - Page 120
Lam Research Corp. v. Inpria Corp.
IPR2025-00256 - U.S. Patent No. 11,537,048

modification will be discussed in this paper. Ultimately, defectless graphoepitaxy DSA of PS-b-PDMS was accomplished using laser spike annealing.

4.2. Results and discussion

4.2.1. Microphase separation by laser spike annealing

Laser annealing is an ultra-fast heating method which was first used in shallow junction annealing[29–31] and recently in organic systems.[32,33] Laser spike annealing is proposed in this study for BCP self-assembly due to its capability of transiently increasing a polymer's stability by hundreds of degree and increasing reaction rates by several orders of magnitude.[34] Diode laser annealing (λ=980 nm) was utilized in this study to enhance the self-assembly of PS-*b*-PDMS in the absence of solvent. The diode laser was fiber coupled and phase changed through a quartz plate homogenizer and focused through a set of lenses. The long axis of diode laser is nearly flat (FWHM =1460 μm) and the short axis still has a Gaussian profile (FWHM=375 μm). Although polymers have some absorption at this wavelength, the film is thin enough to be considered as transparent, and the heating occurs arose from Si bandgap absorption; heat is subsequently dissipated by thermal conduction into the substrate. Peak temperatures on the suface at a given dwell time, are determined by the incident laser power and were caibrated using previously reported protocols.[34]

During the annealing process, this line focused diode laser beam was scanned across the Si wafer along its short axis with scans overlapped with a spacing of 1200 μm to minimize stitching effects. The entire heating and cooling process was controlled by laser scan velocity

Lam Research Ex. 1013 - Page 121
Lam Research Corp. v. Inpria Corp.
IPR2025-00256 - U.S. Patent No. 11,537,048

(10-100 mm/s), resulting in ultrafast heating and cooling (10^4-10^5 K/s). The entire heating and cooling process occurs within several milliseconds (Figure 4.1).

Given the time scale of laser annealing, a cylinder forming PS-*b*-PDMS (M_w = 22 kg mol^{-1}, PDI = 1.1, f_{PS} = 33%) was chosen (Figure 4.2), since each polymer chain needs to move shorter distances compared to lamella morphologies, during the ordering process.[35] The polydimethylsiloxane (PDMS) block contained ~ 23% polyvinylmethylsiloxane, with the vinyl groups potentially serving to either crosslink the block (in order to lock in structures after processing) to enable additional functionalization for future applications.

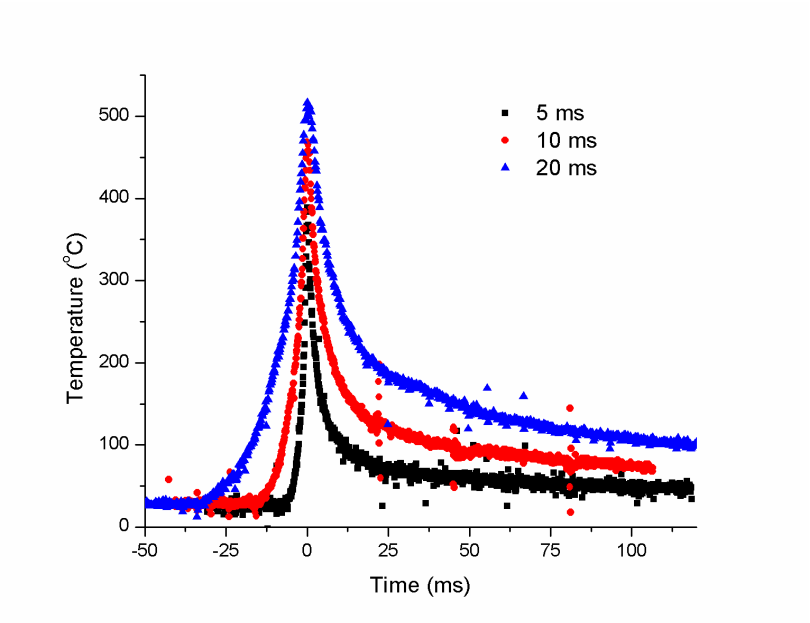

Figure 4.1 In situ measured temperature profiles for dwell times of 5 ms, 10 ms and 20 ms. The time origin in each condition is set to when the peak temperature is reached.

Lam Research Ex. 1013 - Page 122
Lam Research Corp. v. Inpria Corp.
IPR2025-00256 - U.S. Patent No. 11,537,048

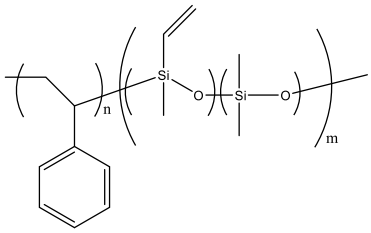

Figure 4.2. Structures of PS-*b*-PDMS used in this work.

Thermal stability of PS-*b*-PDMS during ultra-fast laser heating was first tested for 3-20 ms dwell times with decomposition was observed near 600 °C. Figure 3 shows that microphase separation was achieved during a 3 ms dwell laser annealing at approximately 200 °C (50W). Parallel cylinders with a spacing of 19.4 nm was observed by SEM after selectively removal the top PDMS layer and PS block. Although 200 °C was not a ultra-high temperature, it is well above glass transition temperature of either block of PS-*b*-PDMS ($T_{g,PS}$≈100 °C and $T_{g,PS}$≈-125 °C). Moreover, the relaxation time of PDMS segment at room temperature is in the picosecond regime,[36,37] while the relaxation time of PS segment at 200 °C calculated based on the published experiment data is approximately several milliseconds.[38,39] Therefore, it is not overly surprise that microphase separation can be achieved at this short duration.

No appreciable orientation preference was observed along the laser annealing directions. As reported in the "zone annealing" method, thermal gradient in the range of 10-70 K/mm can direct the grain growth by inducing the shear flow effects.[40] Although the thermal gradient of laser annealing (30 K/mm) is similar as zone annealing, the dwell time of this thermal gradient might be too short to induce the directional flow. Instead, the local defect annihilation at high temperature is more likely to take place in short time and high temperature annealing.

Lam Research Ex. 1013 - Page 123
Lam Research Corp. v. Inpria Corp.
IPR2025-00256 - U.S. Patent No. 11,537,048

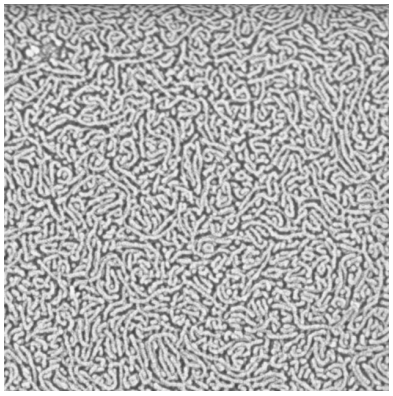

Figure 4.3. Microphase separation of PS-b-PDMS by laser annealing for 3 ms at approximately 200 °C (50W).

4.2.2. Influence of laser power and dwells on BCP ordering

Despite PS-*b*-PDMS was able to microphase separate during a 3 ms dwell laser annealing, the ordering of BCP has to improve in order for lithography application. Therefore, laser annealing power and dwell time were varied in order to examine their effects on the BCP ordering. At low temperatures, polymer chains were still trapped in a non-equilibrium state[35] with no observation of cylindrical morphology (Figure 4a). As temperature increases above the T_g, polymer chains gain enough mobility enough so that two phases start to phase separate in order to minimize the free energy, resulting increased in BCP ordering with increasing temperature as seen in Figure 4a-4d, 4e-4h and 4i-4j.

Grazing incidence small angle X-ray scattering (GISAXS) was used to measure ordering parameters and periodicity of the cylinder morphology (Figure 5a and 5b). Only the primary peak was observed in the as-annealed (non-etched) sample (Figure 5a), but a secondary peak is clearly observed after selective removal of the PS block by reactive ion etching (RIE)

Lam Research Ex. 1013 - Page 124
Lam Research Corp. v. Inpria Corp.
IPR2025-00256 - U.S. Patent No. 11,537,048

(Figure 5b). Figure 5c shows scattering as a function of q* for samples annealed at various temperature for 10 ms. The peak shifts from q* = 0.37 nm^{-1} to 0.34 nm^{-1} at 40 W, and its intensity continued to increase confirming that BCP ordering increases as temperature increases, consistent with SEM images.

However, the increase in ordering saturated above a threshold temperature at each dwell time as seen in Figure 4c, 4g and 4j, note however that longer annealing times led to larger ordered domains upon saturation. In Figure 4j, although a vertical orientation seems to dominate, the BCP alignment actually exhibited a random orientation if viewed on a large scale. In addition, contrast loss was observed above saturation threshold temperature for 5 ms and 10 ms dwell times (Figure 4.4d and 4.4 h), which suggests mixing at the interface between the two blocks.

The ordering of BCPs at the same annealing temperature but different dwell times was different. For example, a peak temperature at 385 °C (40 W) for 20 ms was approximately the same as that of 380 °C for 10 ms (60 W), but the ordering at 20 ms was better than at 10 ms (Figure 4.4h and 4.4j). We also observed this effect when comparing annealing conditions of 290 °C (50 W) for 10 ms with 295 °C (60 W) for 5 ms in Figure 4.4d and 4.4g.

Lam Research Ex. 1013 - Page 125
Lam Research Corp. v. Inpria Corp.
IPR2025-00256 - U.S. Patent No. 11,537,048

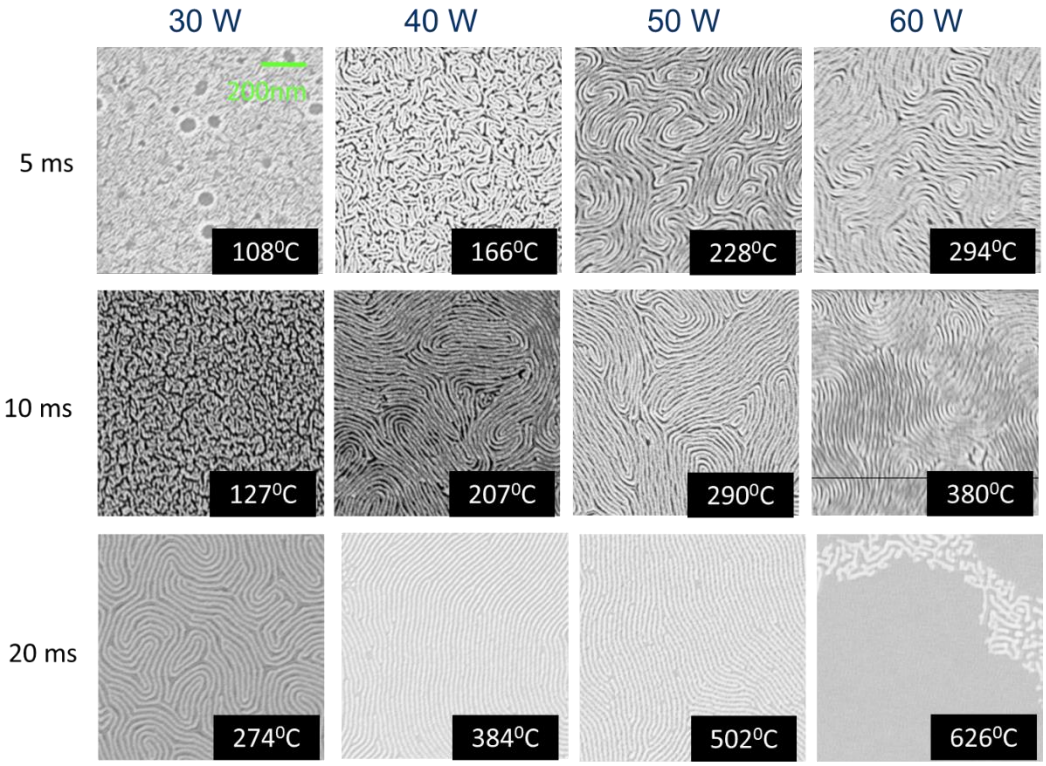

Figure 4.4. SEM images of laser annealed films composed of PS-b-PDMS on Si wafers that have previously been modified with PS brushes. The annealing temperature for each sample is indicated in each image.

Lam Research Ex. 1013 - Page 126
Lam Research Corp. v. Inpria Corp.
IPR2025-00256 - U.S. Patent No. 11,537,048

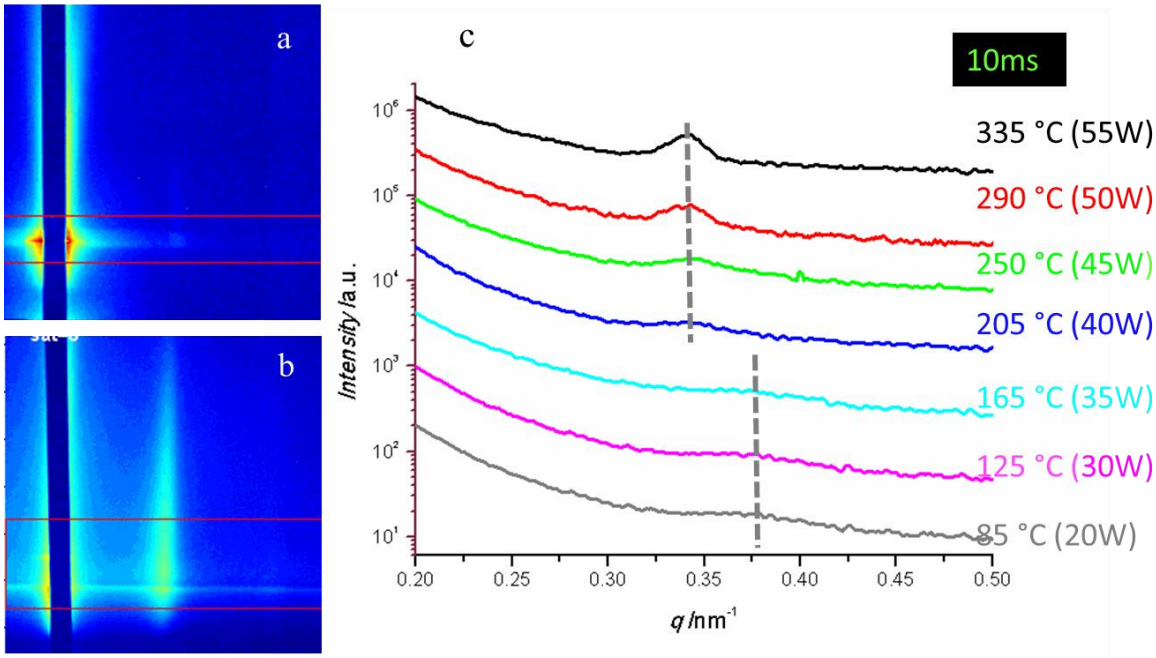

Figure 4.5. GISAXS of laser annealed film composed of PS-b-PDMS on the top of PS brush modified Si wafers. (a) GISAXS of sample annealed at 250 °C (45 W) for 10ms. (b) GISAXS of the same sample etched; a secondary peak is now clearly observed. (c) GISAXS traces from non-etched samples as a function of annealing temperature (power).

The reasons for these difference in ordering are illustrated in the schematic plot in Figure 6. Polymer chains gain mobility above T_g and begin to phase separate, therefore films annealed at low power (below order disorder transition temperature T_{ODT}) continuously increase their order during the time that the temperature is above T_g (Figure 6b). However, the thermodynamic driving force disappears and diffusion of polymer chains leads to the intermixing of two blocks above T_{ODT}. As a result, the initial ordering is partially lost during the period of time that the system is above T_{ODT}, with ultimate ordering in this condition determined by the time spent cooling from T_{ODT} to T_g. If the system is cooled quickly,

Lam Research Ex. 1013 - Page 127
Lam Research Corp. v. Inpria Corp.
IPR2025-00256 - U.S. Patent No. 11,537,048

contrast lose due to remnant mixing at the interface. But if the system is cooled slowly enough, phase separation during cooling will be sufficient to re-establish a sharp interface. The effects we observed in Figure 4d and 4h likely arise from this mixing above T_{ODT}. The phenomenon of contrast loss is less significant for 20 ms since the slower cooling allows sufficient time for full phase separation to be reestablished. Therefore, the BCP order at the same temperature is correlated with dwell times.

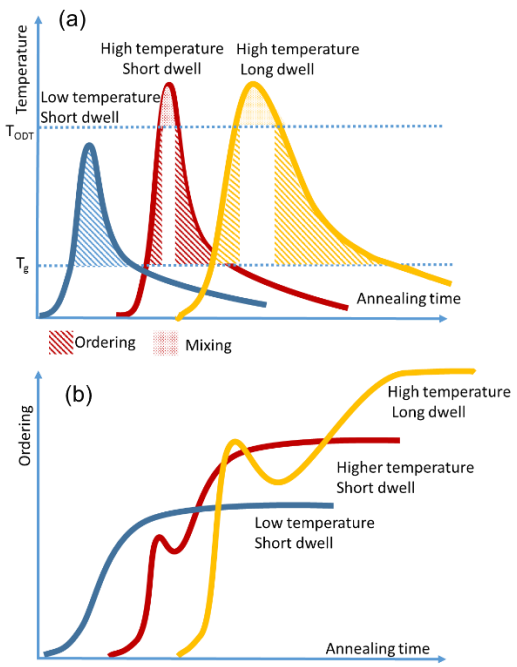

Figure 4.6. Schematic plot of the ordering process for different conditions. (a) Time temperature profiles for three annealing conditions. (b) Ordering characteristic as a function of time for these conditions. Between T_g and T_{ODT}, the ordering increases while above TODT the ordering decrease. The ultimate ordering depends critically on the time above TODT and the cooling rate to T_g.

Lam Research Ex. 1013 - Page 128
Lam Research Corp. v. Inpria Corp.
IPR2025-00256 - U.S. Patent No. 11,537,048

4.2.3. The influences of substrate surface modification on thin film BCP morphology during laser annealing

In addition to annealing temperature and dwell times, surface chemistry is also critical to block copolymer thin film self-assembly, as it controlls dewetting and microstructure orientation. PS and PDMS have much larger difference in the polymer-air surface energy (40.7 mJ/m^2 and 19.8 mJ/m^2 resepectively) than most block copolymer systems. Due to the low surface energy of PDMS, PS-*b*-PDMS film naturally forms a PDMS-air interface. PDMS also tends to wet the native SiO_2 surface, resulting in a PS volume fraction change in the center of the film. Consequently, no parallel cylindrical morphology was observed without a polymer brush surface modification (Figure 7a).

PS, poly(methyl methacrylate) PMMA and PS-co-PMMA random copolymers were applied to the Si wafer before applying BCP to promote the formation of a cylindrical morphology. As seen in Figure 7b-7d, ordering of the BCP is better with PMMA containing polymer brushes, although PMMA would not be normally used for the PS-*b*-PDMS system. PMMA has a surface energy of 41 mJ/m^2 (closer to PS than PDMS), so the PS matrix is drawn to the bottom to minimize interfacial energy. However, the slightly repulsion between the PS block and surface PMMA brushes compared to PS/PS enables higher chain mobility, presumably leading to better ordering during laser annealing. Laser annealing at 250 °C (45 W) for 10 ms was also used to chemically bind PS-OH to Si (as a surface modifier) instead of baking in vacuum oven overnight. This results in a 2 nm thick PS brush and similar level of BCP ordering as that for PS (Figure 7e). By using laser annealing for the polymer binding and

Lam Research Ex. 1013 - Page 129
Lam Research Corp. v. Inpria Corp.
IPR2025-00256 - U.S. Patent No. 11,537,048

BCP film annealing, the total process time for DSA is greatly reduced from hours or days to seconds.

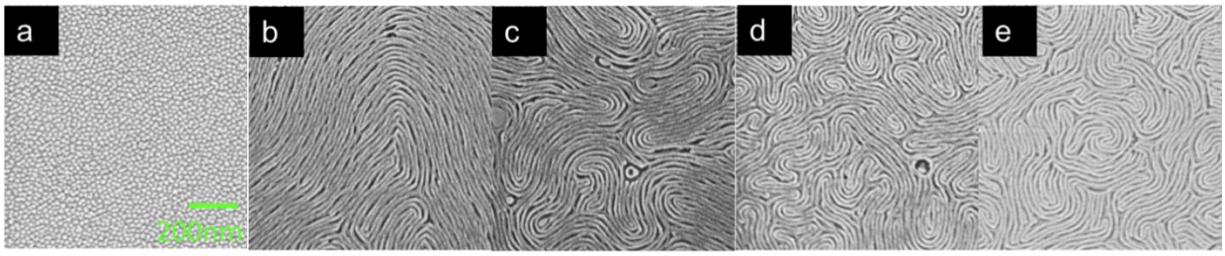

Figure 4.7. SEM images of laser annealing at 250 °C (45 W) for 10ms film composed of PS-*b*-PDMS on Si substrate with different surface modifications: a) bare Si with native SiO_2 layer b) PMMA brushes c) PS-*co*-PMMA brushes d) PS brushes e) PS brushes grafted by laser annealing at 250 °C (45 W) for 10ms.

4.2.4. Graphoepitaxy assisted self-assembly by laser annealing

To demonstrate the capability of utilizing laser annealing for long range alignment of block copolymer structures, we used photolithography and RIE to prepare Si substrates with 250 nm to 1000 nm wide trenches with a depth of 40nm. The patterned substrates were then modified by PS or PMMA brushes. Figure 8 shows the self-assembled PS-*b*-PDMS on these patterned wafers. Annealing at 230 °C for 5 mins on a hotplate, cylinders start to align first along the wall of the trenches. Annealing for the same time at 250 °C shows significantly more alignment, yet many bridging defects were observed and the contrast between blocks was reduced compared to 230 °C. The behavior is similar under laser annealing (Figure 8c and 8d). Nevertheless, simply increasing temperature is not sufficient to achieve perfect alignment. Therefore we increased the laser annealing time to 20 ms. At a slightly higher

Lam Research Ex. 1013 - Page 130
Lam Research Corp. v. Inpria Corp.
IPR2025-00256 - U.S. Patent No. 11,537,048

temperature, significant improvement of alignment is observed as shown in Figure 8e. Long-range alignment in the trenches and a reduction of the defectivity is achieved with contrast maintained between the two blocks due to the effects of both higher temperature and longer cooling time, which is crucial for pattern transfer processes.

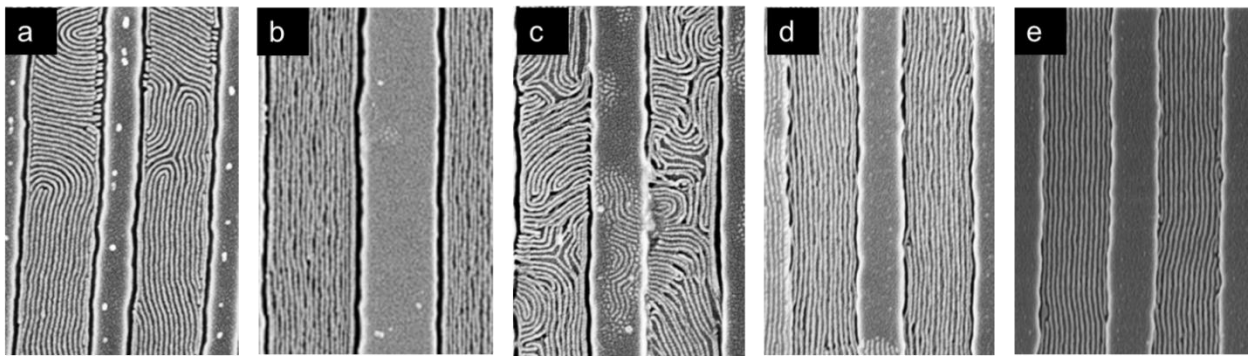

Figure 4.8. SEM images of PS-b-PDMS on PS brush modified substrate. The substrate is pre-patterned with periodic lines. The width of trenches and mesa are 275 nm and 100 nm respectively. The annealing condition from a) hotplate 230 °C 5 min, b) hotplate 250 °C 5 min, c) laser 250 °C (45 W) 10 ms, d) laser 335 °C (55 W) 10 ms, e) laser 440 °C (45 W) 20 ms.

4.3. Conclusions

This research demonstrated for the first time ordered and aligned PS-*b*-PDMS structures formed by solvent-free direct laser annealing on milliseconds time scale, orders of magnitude faster than other thermal annealing methods. During laser annealing, temperatures up to 650 °C were reached transiently. The ordering of cylindrical structures during laser annealing increased with increasing temperature and dwell time. The periodicity of PS-*b*-PDMS (19.4 nm) and the increase in ordering with temperature were confirmed by GISXAS. We further studied the effects of various brushes on a substrate to control the BCP morphology. PMMA

Lam Research Ex. 1013 - Page 131
Lam Research Corp. v. Inpria Corp.
IPR2025-00256 - U.S. Patent No. 11,537,048

brushes, neutral to neither blocks of this polymer and not normally considered as underlayer for PS-*b*-PDMS, were shown to help improve ordering during laser annealing. Finally, by fabricating trenches on the Si substrate with surface brushes, we were able to achieve highly ordered and defect-reduced sub-10 nm patterning using laser annealing at 440 °C for a 20 ms dwell.

4.4. Experimental Section

Materials: Polystyrene-block-polydimethylsiloxane (PS-*b*-PDMS) ($M_{n,PS}$ = 16 kg mol^{-1} , $M_{n,PDMS}$ = 6 kg mol^{-1} ; PDI = 1.1) with 23% of vinyl methyl siloxane was synthesized by anionic polymerization. Hydroxyl-terminated PS (M_n = 10 kg mol^{-1}), hydroxyl terminated PMMA (M_n = 35 kg mol^{-1}, PDI=1.86) and hydroxyl terminated PMMA-*co*-PS (M_n = 133 kg mol^{-1}, PS= 61%, PDI=1.86) were purchased from Polymer Source Inc. and used as received.

Thin film preparation: Polymer brush modified substrates were prepared by spinning coating a 1 wt. % hydroxyl terminated polymer solution in toluene onto oxygen plasma cleaned Si wafers. After baking in a vacuum oven at 170 °C overnight or laser annealing at 45 W for 10ms, the wafers were submerged in toluene, sonicated for 20 minutes and rinsed with toluene. The thickness of this underlayer was determined using a Woollam Ellipsometer. Afterwards, a solution of 1.2 wt. % block copolymer in toluene was spun coated onto patterned or unpatterned substrate to form approximately 35 nm thick thin film.

Thermal annealing and laser annealing: Thermal annealing at temperature up to 250 °C was performed on a hotplate in a normal room ambient. Laser annealing was performed by scanning a focused diode laser across the wafer with a 1 mm track spacing in the ambient

Lam Research Ex. 1013 - Page 132
Lam Research Corp. v. Inpria Corp.
IPR2025-00256 - U.S. Patent No. 11,537,048

environment. The diode laser (λ = 980 nm) was focused to a ~ 2500 μm × ~ 250 μm near flat-top beam and the dwell time was defined as the beam width divided by the scan velocity. To enhance SEM contrast of PS-*b*-PDMS, reactive ion etching was used to selectively remove the PDMS block. Samples were first etched with a CF_4 plasma etch for 4s to remove the top PDMS layer, followed by an O_2 RIE etch for 10s to remove the PS block and oxidize the PDMS block. SEM images were obtained from etched and Pd/Au sputtered samples using a Zeiss Supra SEM operating at 1 kV accelerating potential.

GISAXS characterization: GISAXS was performed at the D1 beam line at the Cornell High Energy Synchrotron Source. The X-ray beam was operated at 10 KeV with a grazing incident angle slightly higher than the critical angle of the polymer at 0.135°. The flux of the beam was 10^{13} photons/ s mm^2 and each image was produced by exposure for 0.2 s.

Acknowledgements

This work is based upon research conducted at the Cornell High Energy Synchrotron Source (CHESS) which is supported by the National Science Foundation and the National Institutes of Health/National Institute of General Medical Sciences under NSF award DMR-1332208, in the Cornell Center for Materials Research (NSF-DMR 0520404), and in the Cornell Nanoscale Facility (NSF-ECS 0335765). Coauthor C.L. acknowledges support by the Deusche Forschungsgemeinschaft. We would also like to thank our collaborators, Michele Laus, Katia Sparnacci, Michell Perego and Luca Boarino for many helpful discussions on this topic.

Lam Research Ex. 1013 - Page 133
Lam Research Corp. v. Inpria Corp.
IPR2025-00256 - U.S. Patent No. 11,537,048

Reference

(1) Xiao, S.; Yang, X.; Steiner, P.; Hsu, Y.; Lee, K.; Wago, K.; Kuo, D. Servo-Integrated Patterned Media by Hybrid Directed Self-Assembly. *ACS Nano* 2014, *8*, 11854–11859.

(2) Yang, X. M.; Wan, L.; Xiao, S.; Xu, Y.; Weller, D. K. Directed Block Copolymer Assembly versus Electron Beam Lithography for Bit-Patterned Media with Areal Density of 1 Terabit/inch2 and beyond. *ACS Nano* 2009, *3*, 1844–1858.

(3) Segalman, R. A.; Yokoyama, H.; Kramer, E. J. Graphoepitaxy of Spherical Domain Block Copolymer Films. *Adv. Mater.* 2001, *13*, 1152–1155.

(4) Kim, S. O.; Solak, H. H.; Stoykovich, M. P.; Ferrier, N. J.; De Pablo, J. J.; Nealey, P. F. Epitaxial Self-Assembly of Block Copolymers on Lithographically Defined Nanopatterned Substrates. *Nature* 2003, *424*, 411–414.

(5) Herr, D. J. C. Directed Block Copolymer Self-Assembly for Nanoelectronics Fabrication. *J. Mater. Res.* 2011, *26*, 122–139.

(6) Stoykovich, M. P.; Müller, M.; Kim, S. O.; Solak, H. H.; Edwards, E. W.; de Pablo, J. J.; Nealey, P. F. Directed Assembly of Block Copolymer Blends into Nonregular Device-Oriented Structures. *Science* 2005, *308*, 1442–1446.

(7) Tavakkoli K G, A.; Gotrik, K. W.; Hannon, a F.; Alexander-Katz, A.; Ross, C. A.; Berggren, K. K. Templating Three-Dimensional Self-Assembled Structures in Bilayer Block Copolymer Films. *Science* 2012, *336*, 1294–1298.

(8) Bita, I.; Yang, J. K. W.; Jung, Y. S.; Ross, C. A.; Thomas, E. L.; Berggren, K. K. Graphoepitaxy of Self-Assembled Block Copolymers on Two-Dimensional Periodic Patterned Templates. *Science* 2008, *321*, 939–943.

(9) Botiz, I.; Darling, S. B. Optoelectronics Using Block Copolymers. *Materials Today*, 2010, *13*, 42–51.

(10) Topham, P. D.; Parnell, A. J.; Hiorns, R. C. Block Copolymer Strategies for Solar Cell Technology. *Journal of Polymer Science, Part B: Polymer Physics*, 2011, *49*, 1131–1156.

(11) Li, L.; Schulte, L.; Clausen, L. D.; Hansen, K. M.; Jonsson, G. E.; Ndoni, S. Gyroid Nanoporous Membranes with Tunable Permeability. *ACS Nano* 2011, *5*, 7754–7766.

(12) Jackson, E. A.; Lee, Y.; Hillmyer, M. A. ABAC Tetrablock Terpolymers for Tough Nanoporous Filtration Membranes. *Macromolecules* 2013, *46*, 1484–1491.

(13) Tao, Y.; Ma, B.; Segalman, R. A. Self-Assembly of Rod-Coil Block Copolymers and Their Application in Electroluminescent Devices. *Macromolecules* 2008, *41*, 7152–7159.

(14) Lo, K. H.; Chen, M. C.; Ho, R. M.; Sung, H. W. Pore-Filling Nanoporous Templates from Degradable Block Copolymers for Nanoscale Drug Delivery. *ACS Nano* 2009, *3*, 2660–2666.

(15) Yang, S. Y.; Yang, J. A.; Kim, E. S.; Jeon, G.; Oh, E. J.; Choi, K. Y.; Hahn, S. K.; Kim, J. K. Single-File Diffusion of Protein Drugs through Cylindrical Nanochannels. *ACS Nano* 2010, *4*, 3817–3822.

(16) Jeon, G.; Yang, S. Y.; Kim, J. K. Functional Nanoporous Membranes for Drug Delivery. *J. Mater. Chem.* 2012, *22*, 14814.

(17) Liu, C.-C.; Thode, C. J.; Rincon Delgadillo, P. A.; Craig, G. S. W.; Nealey, P. F.; Gronheid, R. Towards an All-Track 300 Mm Process for Directed Self-Assembly. *J. Vac. Sci. Technol. B Microelectron. Nanom. Struct.* 2011, *29*, 06F203.

(18) Son, J. G.; Gotrik, K. W.; Ross, C. A. High-Aspect-Ratio Perpendicular Orientation of PS- B -PDMS Thin Films under Solvent Annealing. *ACS Macro Lett.* 2012, *1*, 1279–1284.

(19) Jung, Y. S.; Ross, C. A. Orientation-Controlled Self-Assembled Nanolithography Using a Polystyrene-Polydimethylsiloxane Block Copolymer. *Nano letters*, 2007, *7*, 2046–2050.

(20) Son, J. G.; Chang, J.-B.; Berggren, K. K.; Ross, C. A. Assembly of Sub-10-Nm Block Copolymer Patterns with Mixed Morphology and Period Using Electron Irradiation and Solvent Annealing. *Nano Lett.* 2011, *11*, 5079–5084.

(21) Chen, J. T.; Thomas, E. L.; Ober, C. K.; Hwang, S. S. Zigzag Morphology of a Poly(Styrene-B-Hexyl Isocyanate) Rod Coil Block-Copolymer. *Macromolecules* 1995, *28*, 1688–1697.

(22) Bosworth, J. K.; Paik, M. Y.; Ruiz, R.; Schwartz, E. L.; Huang, J. Q.; Ko, A. W.; Smilgies, D. M.; Black, C. T.; Ober, C. K. Control of Self-Assembly of Lithographically Patternable Block Copolymer Films. *ACS Nano* 2008, *2*, 1396–1402.

(23) Welander, A. M.; Kang, H.; Stuen, K. O.; Solak, H. H.; Müller, M.; de Pablo, J. J.; Nealey, P. F.; Pablo, J. J. De; Nealey, P. F. Rapid Directed Assembly of Block Copolymer Films at Elevated Temperatures. *Macromolecules* 2008, *41*, 2759–2761.

(24) Borah, D.; Senthamaraikannan, R.; Rasappa, S.; Kosmala, B.; Holmes, J. D.; Morris, M. a. Swift Nanopattern Formation of PS-B-PMMA and PS-B-PDMS Block

Lam Research Ex. 1013 - Page 135
Lam Research Corp. v. Inpria Corp.
IPR2025-00256 - U.S. Patent No. 11,537,048

Copolymer Films Using a Microwave Assisted Technique. *ACS Nano* 2013, *7*, 6583–6596.

(25) Park, W. I.; Kim, K.; Jang, H.-I.; Jeong, J. W.; Kim, J. M.; Choi, J.; Park, J. H.; Jung, Y. S. Directed Self-Assembly with Sub-100 Degrees Celsius Processing Temperature, Sub-10 Nanometer Resolution, and Sub-1 Minute Assembly Time. *Small* 2012, *8*, 3762–3768.

(26) Ferrarese Lupi, F.; Giammaria, T. J.; Ceresoli, M.; Seguini, G.; Sparnacci, K.; Antonioli, D.; Gianotti, V.; Laus, M.; Perego, M. Rapid Thermal Processing of Self-Assembling Block Copolymer Thin Films. *Nanotechnology* 2013, *24*, 315601.

(27) Majewski, P. W.; Yager, K. G. Millisecond Ordering of Block Copolymer Films via Photothermal Gradients. *ACS Nano* 2015, *9*, 3896–3906.

(28) Singer, J. P.; Gotrik, K. W.; Lee, J.-H.; Kooi, S. E.; Ross, C. A.; Thomas, E. L. Alignment and Reordering of a Block Copolymer by Solvent-Enhanced Thermal Laser Direct Write. *Polymer (Guildf).* 2014, *55*, 1875–1882.

(29) Talwar, S.; Markle, D.; Thompson, M. Junction Scaling Using Lasers for Thermal Annealing. *Solid State Technol.* 2003, *46*, 83.

(30) Ho, J. C.; Yerushalmi, R.; Smith, G.; Majhi, P.; Bennett, J.; Halim, J.; Faifer, V. N.; Javey, A. Wafer-Scale, Sub-5 Nm Junction Formation by Monolayer Doping and Conventional Spike Annealing. *Nano Lett.* 2009, *9*, 725–730.

(31) Cho, K.; Numan, M.; Finstad, T. G.; Chu, W. K.; Liu, J.; Wortman, J. J. Transient Enhanced Diffusion during Rapid Thermal Annealing of Boron Implanted Silicon. *Appl. Phys. Lett.* 1985, *47*, 1321.

(32) Sha, J.; Jung, B.; Thompson, M. O.; Ober, C. K.; Chandhok, M.; Younkin, T. R. Submillisecond Post-Exposure Bake of Chemically Amplified Resists by CO2 Laser Spike Annealing. *J. Vac. Sci. Technol. B* 2009, *27*, 3020–3024.

(33) Jung, B.; Satish, P.; Bunck, D. N.; Dichtel, W. R.; Ober, C. K.; Thompson, M. O. Laser-Induced Sub-Millisecond Heating Reveals Distinct Tertiary Ester Cleavage Reaction Pathways in a Photolithographic Resist Polymer. *ACS Nano* 2014, *8*, 5746–5756.

(34) Jung, B.; Sha, J.; Paredes, F.; Chandhok, M.; Younkin, T. R.; Wiesner, U.; Ober, C. K.; Thompson, M. O. Kinetic Rates of Thermal Transformations and Diffusion in Polymer Systems Measured during Sub-Millisecond Laser-Induced Heating. *ACS Nano* 2012, *6*, 5830–5836.

(35) Yokoyama, H. Diffusion of Block Copolymers. *Mater. Sci. Eng. R Reports* 2006, *53*, 199–248.

Lam Research Ex. 1013 - Page 136
Lam Research Corp. v. Inpria Corp.
IPR2025-00256 - U.S. Patent No. 11,537,048

(36) Valle-Carrandi, L. del; Alegría, A.; Colmenero, J. PDMS Behaviour under Confinement in Strongly Segregated Mesophases of PS-PDMS Diblock Copolymers. *Eur. Phys. J. Spec. Top.* 2010, *189*, 257–261.

(37) Del Valle-Carrandi, L.; Alegría, A.; Arbe, A.; Colmenero, J. Unexpected PDMS Behavior in Segregated Cylindrical and Spherical Nanophases of PS-PDMS Asymmetric Diblock Copolymers. *Macromolecules* 2012, *45*, 491–502.

(38) Santangelo, P. G.; Roland, C. M.; Chang, T.; Cho, D.; Roovers, J. Dynamics near the Glass Temperature of Low Molecular Weight Cyclic Polystyrene. *Macromolecules* 2001, *34*, 9002–9005.

(39) Abou Elfadl, A.; Herrmann, A.; Hintermeyer, J.; Petzold, N.; Novikov, V. N.; Rössler, E. A. Molecular Weight Dependence of Fragility in Polymers. *Macromolecules* 2009, *42*, 6816–6817.

(40) Berry, B. C.; Bosse, A. W.; Douglas, J. F.; Jones, R. L.; Karim, A. Orientational Order in Block Copolymer Films Zone Annealed below the Order--Disorder Transition Temperature. *Nano letters*, 2007, *7*, 2789–2794.

Lam Research Ex. 1013 - Page 137
Lam Research Corp. v. Inpria Corp.
IPR2025-00256 - U.S. Patent No. 11,537,048

CHAPTER 5 MECHANISM STUDIES OF CARBOXYLIC ACID LIGAND STABILIZED METAL OXIDE NANOPARTICLE EUV (ONE) RESIST

5.1. Introduction and motivation

Extreme ultraviolet (13.5 nm) lithography is theoretically able to extend the Rayleigh resolution limit to 15 nm half pitch, while ArF double patterning produces 30-20 nm half-pitch.[1,2] This technology was proposed several years ago to replace 193 nm lithography, yet was delayed due to many engineering challenges. Recently, the insertion of EUV lithography to high volume manufacturing has become more realistic, as stable 100W EUV light sources became available and are being tested.[3–5] On the other hand, the development of chemically amplified resist (CAR) has not yet made a breakthrough for EUV. CAR which was designed for DUV lithography does not take full advantages of the short wavelength of EUV radiation. Instead sensitivity decreased when the wavelength was reduced to 13.5 nm; moreover, image blurring becomes more severe due to out of band radiation.[6] Out of band radiation is caused by photoelectron and secondary radiation generated after ionization of resist materials, which range from 100 nm to 400 nm wavelength. CARs are more sensitive to these lower energy photons, so undesirable reactions occur when they randomly occur in the resist film. Therefore, in order to meet EUV requirements of high resolution, low roughness and high sensitivity, discovering resists with novel patterning mechanism which can take advantage of high energy EUV photons are critical.

Lam Research Ex. 1013 - Page 138
Lam Research Corp. v. Inpria Corp.
IPR2025-00256 - U.S. Patent No. 11,537,048

Oxide nanoparticle EUV (ONE) resists with extraordinary EUV sensitivity, first reported by Ober *et al* form such a resist platform.[7] The first generation of HfO_2 nanoparticles with methacrylic acid (MAA) as ligands produced dual tone DUV photoresists with relatively low DUV sensitivity, yet they were able to resolve negative tone 25 nm 1:2 line space patterns with an remarkably high EUV sensitivity (4.2 mJ/cm^2). The different sensitivity between EUV and DUV radiation is a great advantage for avoiding out of band effects.

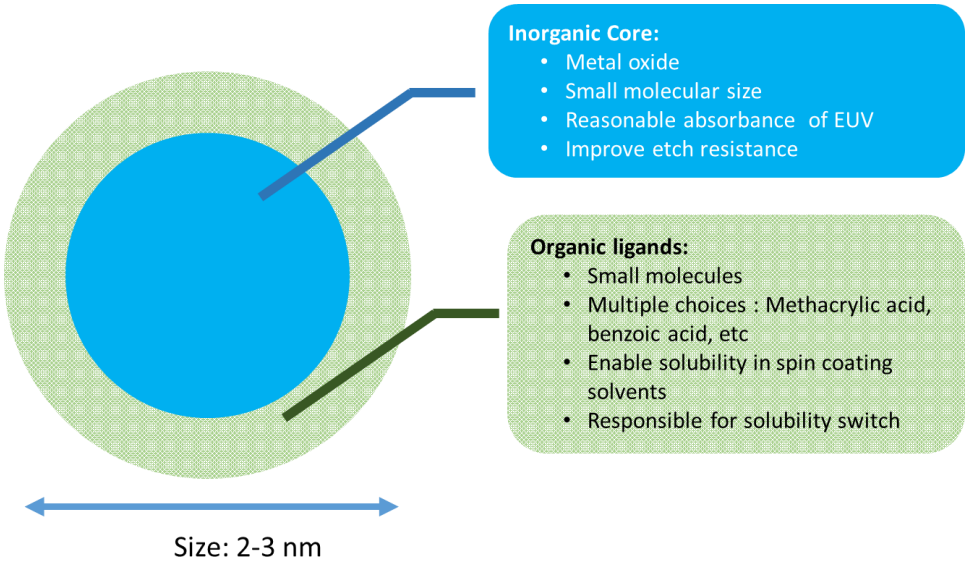

Figure 5.1 ONE resist scheme.

As shown in Figure 5.1, ONE resists contain metal oxide cores and ligands are covalently bound to metal oxide. The nanoparticle sizes measured by dynamic light scattering (DLS) are of 2-5 nm, as shown in schematic Figure 5.1. The 45% organic content provides the solubility of the ONE resist in organic solvents and stabilizes nanoparticles from aggregation.

Lam Research Ex. 1013 - Page 139
Lam Research Corp. v. Inpria Corp.
IPR2025-00256 - U.S. Patent No. 11,537,048

Furthermore, the many choices of different organic ligands have great potential for resist formulation optimization. On the other hand, the inorganic content provides thermal stability, chemical stability and etch resistance.

Both the organic and inorganic content are responsible for the EUV absorption, which is calculated by the following equation:

$$\mu = \frac{N_A \rho}{MW} \sum_i x_i \sigma_{\alpha i}$$

where is μ the EUV absorption coefficient of the given compound, ρ is the density, MW is the molecule weight of a compound, x_i is the number fraction of component i and $\sigma_{\alpha i}$ is the atomic photo-absorption cross section. 13.5 nm radiation has a corresponding photon energy of 91.8 eV. The atomic photo-absorption cross section from 10 eV -100 keV was measured by Howerton *et al*. in 1975 [8,9]. Figure 2 is the photoabsorption cross section at 91.8 eV.

Lam Research Ex. 1013 - Page 140
Lam Research Corp. v. Inpria Corp.
IPR2025-00256 - U.S. Patent No. 11,537,048

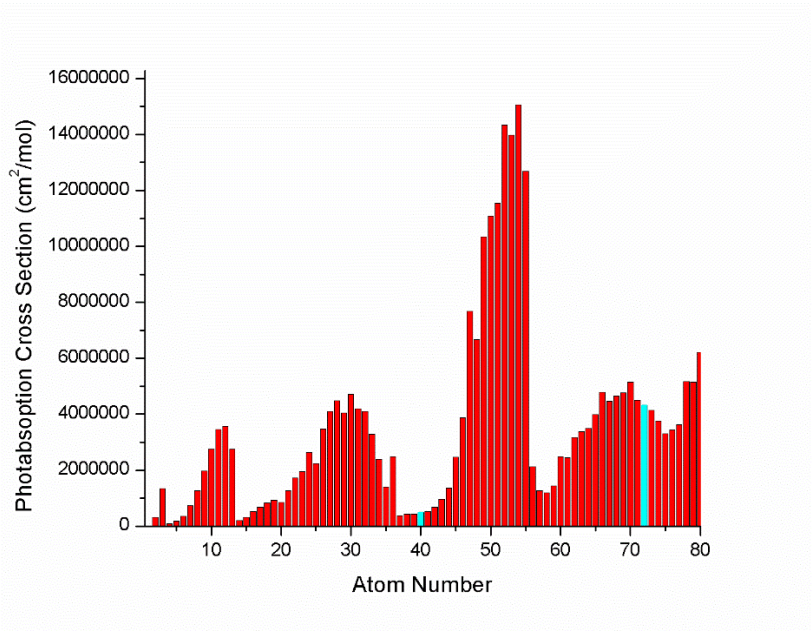

Figure 5.2 Atomic EUV absorbance cross section. Blue lines are for Zr (left) and Hf (right).

EUV absorption of ZrO_2, HfO_2 and MAA are 7.57, 8.4 and 4.31 respectively. Metal oxide has a higher photoabsorption due to its high density and oxygen content. In addition, the similar photoabsorption of ZrO_2 and HfO_2 explains the similar EUV sensitivity of ZrO_2 and HfO_2 with the same ligands.

Although a PAG or photoradical initiator were added as part of the ONE resist formulation with MAA to provide a double bond potentially for crosslinking, NMR and FTIR studies showed the double bond remained unreacted after exposure.[10] Therefore crosslinking is not the negative tone patterning mechanism. Instead, FTIR studies show that free MAA content increased while bound MAA content decreased after exposure. Therefore, ligand exchange mechanism is proposed.[11] According to the calculations, one anion generated upon UV exposure will replace 7 ligands, resulting in a solubility change. As positive tone ONE resist mechanism, it has been proposed that ligands leave the nanoparticle film and make

Lam Research Ex. 1013 - Page 141
Lam Research Corp. v. Inpria Corp.
IPR2025-00256 - U.S. Patent No. 11,537,048

nanoparticles easier to aggregate and less soluble.[12] Although FTIR analysis of chemical change after exposure is valid, it did not provide a clear explanation of entire patterning mechanism. For example, how does the ligand exchange affects solubility and the difference of PEB and PEB-free samples are not easily explained. Later studied by M Krysak showed that ONE resist without PAG addition can also resolve negative tone patterns.[13] It has been suggested the ligand loss is directed by EUV radiation, which contradicts with the previous aspects of previous ligand exchange theory. In this study, the author will address these questions and provide a more comprehensive understanding of patterning by using different characterization methods.

5.2. Experimental

5.2.1. Materials

All reagent materials were purchased from Sigma Aldrich and were used as received. All solvents were purchased from fisher science and were used as received.

5.2.2. Nanoparticles synthesis

5.2.2.1. Methacrylic acid stabilized hafnium oxide or Zirconium oxide nanoparticles

3 g (12 mmol) of either hafnium isopropoxide or zirconium isopropoxide was added to 12 mL of Methacrylic acid to a three-necked round-bottomed flask fitted with a condenser. The

Lam Research Ex. 1013 - Page 142
Lam Research Corp. v. Inpria Corp.
IPR2025-00256 - U.S. Patent No. 11,537,048

mixture was stirred for 15 minutes before raise the temperature to 65 °C. After equilibrating for 90 minutes, 1 ml of deionized (DI) water was added to the mixture drop by drop and the solution turns clear. After reacting for 18 hours, the solution was cooled down and then was added 5 times of 1:1 water methanol by volume. After vortexing, the mixture was centrifuged at 8000 rpm for 8 minutes. The solvents were decanted and then 5 ml of nanoparticles was then washed with 36 ml water centrifuged at 8000 rpm for 5 minutes. Collecting the precipitates and dry in a vacuum oven at 65 °C overnight. 1.8 g of white power was obtained.

5.2.3. Physical characterization

5.2.3.1. Dynamic light scattering

1 wt.% nanoparticle dry powders was dissolved in PGMEA and filtered through 0.2 μm PTFE filters. The averaged particles dynamic size was measured with a Malvern Zetasizer Nano-ZS with Dynamic Light Scattering at room temperature.

5.2.3.2. Thermogravimetric analysis

Lam Research Ex. 1013 - Page 143
Lam Research Corp. v. Inpria Corp.
IPR2025-00256 - U.S. Patent No. 11,537,048

Thermal analysis was performed in a TA instrument Q500 thermal gravimetric analyzer (TGA) or an Exstar TG/DTA 6200 (Seiko Instruments, Inc., Torrance, CA) at the heating rate of 10 °C/min under N_2.

5.2.3.3. Chemical characterization

Spectra recorded in $(CD_3)_2CO$ were referenced to internal tetramethylsilane (0 ppm). Transmittance or absorbance FT-IR spectra of nanoparticle dry powders were obtained by using Mattson Instruments Galaxy 2020 FT-IR spectrometer in ATR mode. Quantitative elemental analysis as well as chemical bonding information were analyzed using a SSX-100 X-ray photoelectron spectroscopy (XPS) system.

5.2.3.4. Dissolution rate measurement

Dissolution rate of nanoparticles film in developer was measured by an Inficon Quartz crystal microbalance. 10 wt. % of resist solution was spin coated to a clean quartz crystal. After the crystal was placed in the oscillator, the frequency changes was started to log. Then the oscillator was dipped in to slowly stirred developer. The frequency change recorded during the development process, which is directly proportional to the mass of the film on the crystal according to Sauerbrey equation below. Using this equation, the changes in frequency are converted into film thickness. The thickness change versus time during the process was normalized.

$$\Delta f = -\Delta m \frac{2f^2}{A\sqrt{\rho_q \mu_q}}$$

Lam Research Ex. 1013 - Page 144
Lam Research Corp. v. Inpria Corp.
IPR2025-00256 - U.S. Patent No. 11,537,048

Here, Δf = frequency change, f = resonant frequency (Hz), A = area, ρ_q = quartz density μ_q = quartz shear modulus, and Δm = mass change.

5.2.3.5. Negative tone process by DUV lithography

5 wt. % of n-hydroxynaphthanene triflate was added to nanoparticle powders. Then nanoparticles with PAG was dissolved in PGMEA to form a 5 wt. % solution. After sonication for 5 minutes, the solution was filtered through 0.2 μm PTFE filters and spun coated on to unprimed wafer at 4000 rpm for 60s, followed by a post-apply bake at 110 °C for 60s. After exposed to DUV radiance at 248nm, the resist films were developed in PGMEA and 4-methyl-2pentonl mix solvents and blow-dried. The ratio of two solvents and the development time are optimized for each nanoparticle to get the best contrast and imaging result. Post-exposure bake is not necessary unless noted.

5.2.3.6. EUV lithography

EUV exposures were performed using the SEMATECH 0.3-NA extreme ultraviolet (EUV) microlithography tool in the advance light source of Lawrence Berkeley National Lab. The solution preparation is the same as the DUV patterning. The spin coating speed is adjusted to form a uniform film at 40 nm with ±10% variation.

5.2.3.7. Imaging process

Lam Research Ex. 1013 - Page 145
Lam Research Corp. v. Inpria Corp.
IPR2025-00256 - U.S. Patent No. 11,537,048

The SEM images were taken using Keck SEM at 0.8 kV without Au/Pd sputtering. The CD and LER were calculated using SuMMIT image analysis software (EUV technology, Martinez, CA).

5.3. Results and discussion

5.3.1. Synthesis

Hydrolysis, acidolysis and condensation reactions are the main reaction mechanisms of the nanoparticle synthesis.[14,15] The hydrolysis of metal alkoxide precursors and subsequent condensation reactions were catalyzed by acid and water. The presence of carboxylic acids compete with water to react with hafnium hydroxide and form the ligand stabilized metal oxide nanoparticle gel. During wash steps, the unreacted acids was extracted by acetone and the nanoparticles were precipitated from the water.

5.3.2. Structural characterization

Dynamic light scattering was used to measure hydrodynamic size of nanoparticles undergoing Brownian motion by a laser beam. The hydrodynamic size of nanoparticles includes the hafnium oxide cores, the attached ligands and the surrounding solvent. The averaged particles sizes have a narrow distribution around 2-5 nm (Figure 5.3). The small particle size provides small enough building blocks for high resolution patterning. The small angle scattering of as-synthesized nanoparticle powders indicated that nanoparticles are in the amorphous form with correlation length between two nanoparticle cores are of 1.5 nm (Figure 5.4). The size

Lam Research Ex. 1013 - Page 146
Lam Research Corp. v. Inpria Corp.
IPR2025-00256 - U.S. Patent No. 11,537,048

distribution is due to the multiple molecule structures formed during synthesis at room temperature.

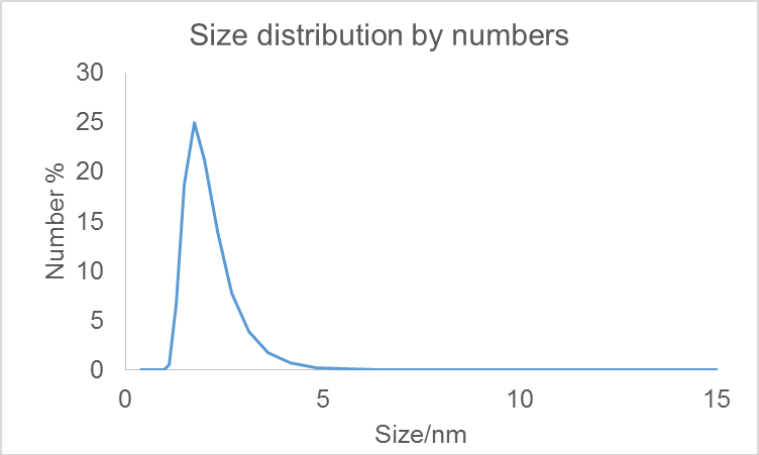

Figure 5.3 HfO_2-MAA nanoparticle size distribution measured by DLS.

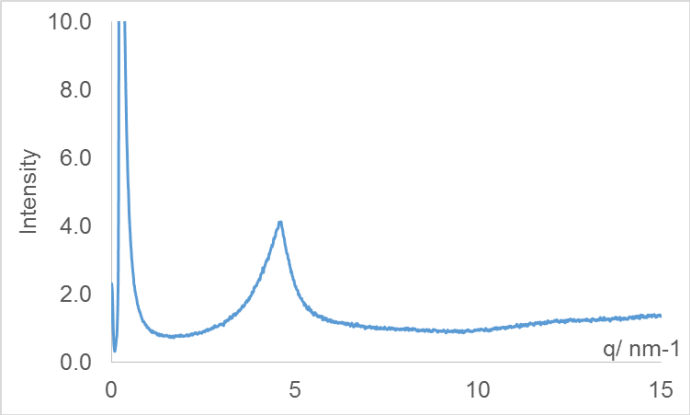

Figure 5.4 SAXS of HfO_2-MAA powders.

Lam Research Ex. 1013 - Page 147
Lam Research Corp. v. Inpria Corp.
IPR2025-00256 - U.S. Patent No. 11,537,048

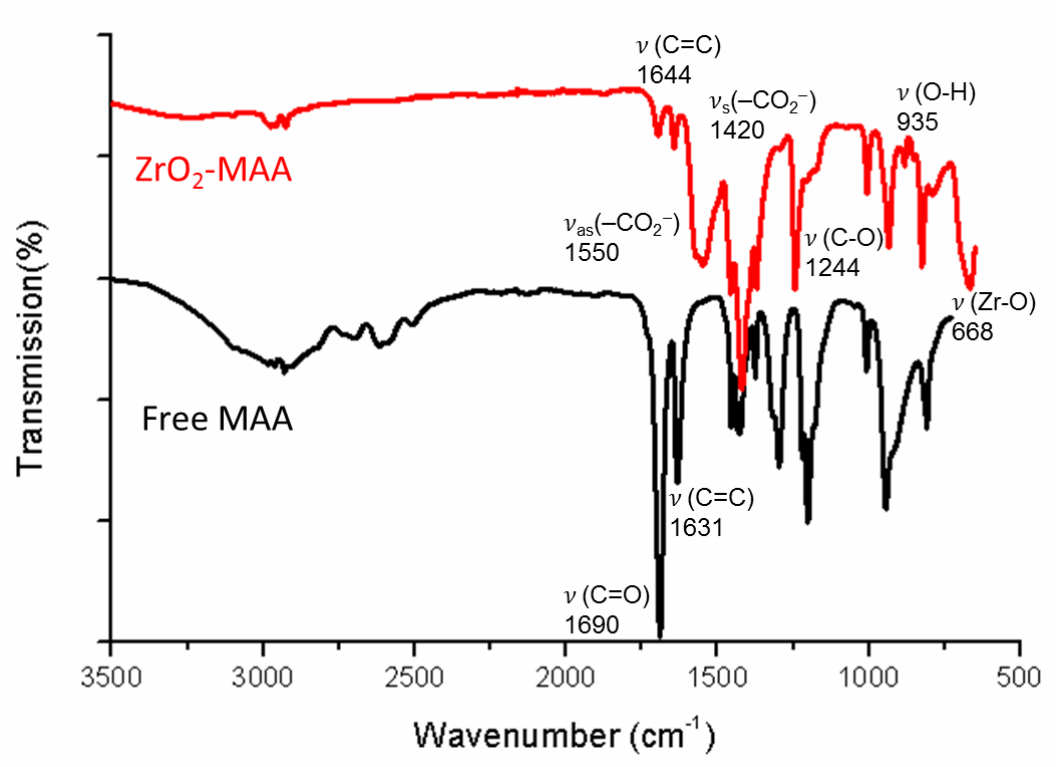

Figure 5.5 FTIR of ZrO_2-MAA (top) and free MAA (bottom)

Figure 5.5 presents the IR spectra of both free methacrylic acid and hafnium oxide nanoparticles with methacrylic acid. In the FTIR analysis, we can see some C-H stretching at around 2960-3050 cm^{-1} in both nanoparticles and free MAA spectra. C=H stretching peak at 1631cm^{-1} in the free methacrylic acid shifts to 1641 cm^{-1} in the nanoparticle sample, and C-O stretching at 1293 cm^{-1} shifts to 1244 cm^{-1}. The spectra of free MAA shows the C=O stretching at 1690 cm^{-1}, while after bonding to hafnium oxide , the C=O stretching peaks shift to lower wave number with the $\nu_{asy}(CO_2^-)$ at 1550 cm^{-1} and $\nu_{sy}(CO_2^-)$ at 1420 cm^{-1} suggesting the MAA ligands are successfully bound to the ZrO_2 complex. The Δ between the symmetric and asymmetric C=O stretching is an indication of the configuration that acids are bound to oxides. Theoretically, unidentate, bridging and chelating complexes have Δ at approximately

Lam Research Ex. 1013 - Page 148
Lam Research Corp. v. Inpria Corp.
IPR2025-00256 - U.S. Patent No. 11,537,048

200-320 cm^{-1}, 140-190 cm^{-1} and below 130 cm^{-1}. [16] Therefore, the 130cm^{-1} Δ can be ascribed to the chelating configuration. The FTIR spectra of all the nanoparticles obtained show Δ in the range of 100-130 cm^{-1}, which suggest a great part of ligands bind to nanoparticles in chelating configuration while some might bind in bridging configuration. Zr-O stretching vibration is shown below 700 cm^{-1}, confirming the formation of ZrO_2. O-H stretching corresponding to Metal-OH is around 3750 cm^{-1}.

X-ray photoelectron spectroscopy (XPS) was used to study the composition and structure of ZrO_2-MAA nanoparticles (Figure 5.6). The Zr3d spectra were split into doublet of $Zr3d_{3/2}$ at 185.6 eV and $Zr3d_{5/2}$ at 183.3 eV which suggest Zr is in +4 oxidized states. The C 1s region can be convoluted into two components: one at 285.0 eV attributed to alkyl carbon and the other at 288.8 eV attributed to carbonyl carbon. The O 1s region can be convoluted into three components: the lowest BE component at 527.8 eV corresponding to Zr-O-Zr bond, the medium BE component at 530.4 eV corresponding to Zr-OH bond and the highest BE component 532.0 eV corresponding to C-O bond. The atomic analysis of XPS spectra showed the ratio of C,O and Zr is 5.78:3.34:1, which can be converted to $ZrO_{0.44}$ $MAA_{1.45}$.

Lam Research Ex. 1013 - Page 149
Lam Research Corp. v. Inpria Corp.
IPR2025-00256 - U.S. Patent No. 11,537,048

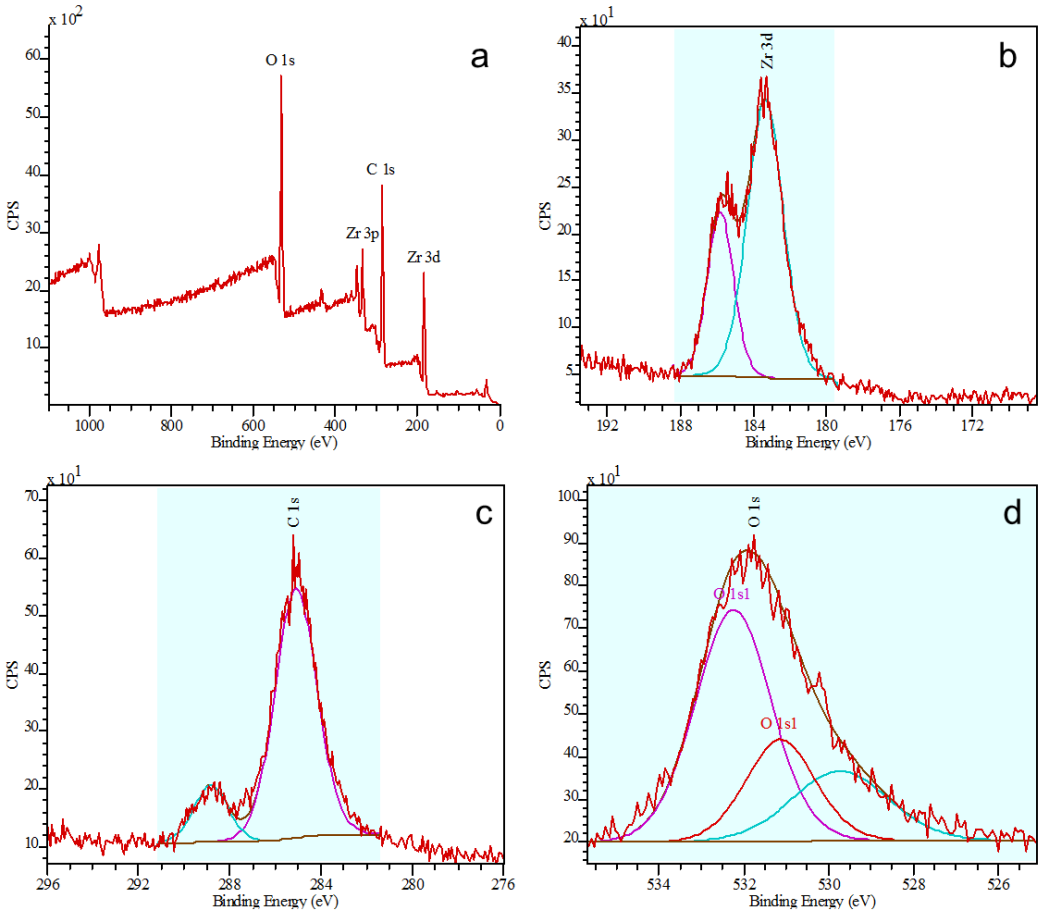

Figure 5.6 XPS spectrum of ZrO_2-MAA. a) a full scan of hybrid nanoparticles b) Zr 3d region c) C 1s region d) O 1s region.

5.3.3. Organic content and ligand strength measurement by TG/DTA studies

TGA determines the weight loss during a heating circle. Differential thermal analysis measures the temperature difference between tested samples and an inert reference that undergo identical thermal cycles. If an endothermic process take place, DTA would record a negative temperature peak and vice versa. Therefore TG/DTA was used to probe thermal effects of reaction and phase as well as mass change.

Lam Research Ex. 1013 - Page 150
Lam Research Corp. v. Inpria Corp.
IPR2025-00256 - U.S. Patent No. 11,537,048

Nanoparticles usually contain 45-70% of organic content depending on the molecular weight of ligands. The organic content can be used to calculate to the ratio of ligands to zirconium. For example, ZrO_2-MAA contains 45% of organic content, therefore the ligand to Zr ratio can be calculated using the following equation, as the oxygen in MAA can be used to form ZrO_2 during heating. However, the ligand to Zr ratio calculated from TGA is less than XPS studies, as XPS might only probe the surface of resist film.

$$\text{MAA} - \text{Zr ratio} = \frac{0.40/(12 * 4 + 6)}{0.60/(91 + 16 * 2)} \approx 1.52$$

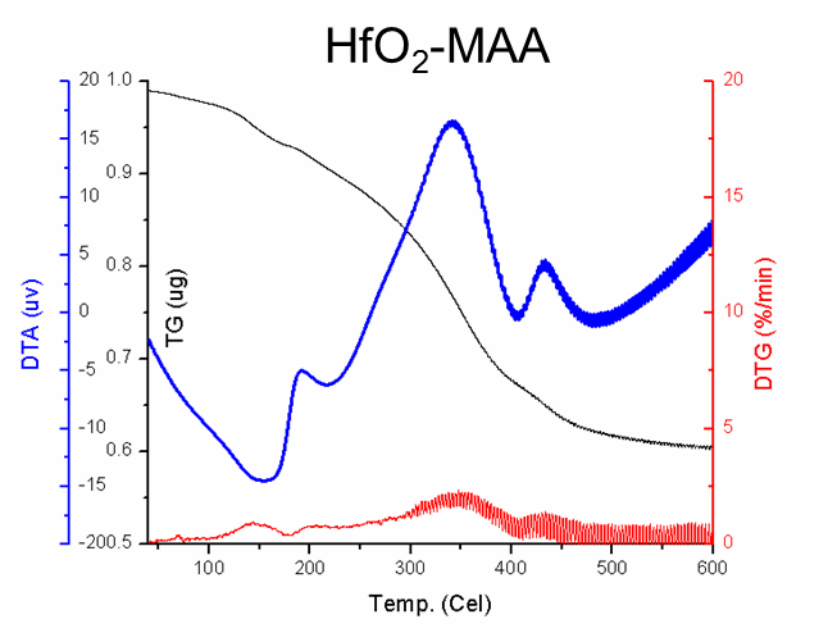

Figure 5.7 DTA curves of HfO2-MAA.

A typical DTA curve for HfO_2-MAA nanoparticles is shown in Figure 5.7 and the DTG is the first derivative of the TGA data which is normalized to its initial weight. The first endothermic transition in the DTA curve appears at 154 °C corresponds to the first weight loss peak in the DTG curves which should be attributed to the initial desorption of ligands.

Lam Research Ex. 1013 - Page 151
Lam Research Corp. v. Inpria Corp.
IPR2025-00256 - U.S. Patent No. 11,537,048

The second peak at 200 °C and third peak at 341 °C correspond to exothermic transitions in DTA which should be attributed to both ligand loss and the decomposition of the byproducts. The forth exothermic peak at 430 °C is due to the oxidation of ZrO_2 nanoparticles.

In order to further evaluate ligand loss at different stages, we performed the TGA studied held at constant temperatures. As seen in Figure 5.8, when nanoparticle powders were held at 154 °C, there is only about 2% weight loss during 20 minutes heating. In contrast, when the samples were raised to 341°C, nanoparticles lost more than 31% weight after 10 minutes which accounts for the majority of ligands that bind to ZrO_2 cores. Although from TGA studies shows annealing at 154 °C only cause 2% weight loss, it caused a huge difference in dissolution behavior of nanoparticles.

Lam Research Ex. 1013 - Page 152
Lam Research Corp. v. Inpria Corp.
IPR2025-00256 - U.S. Patent No. 11,537,048

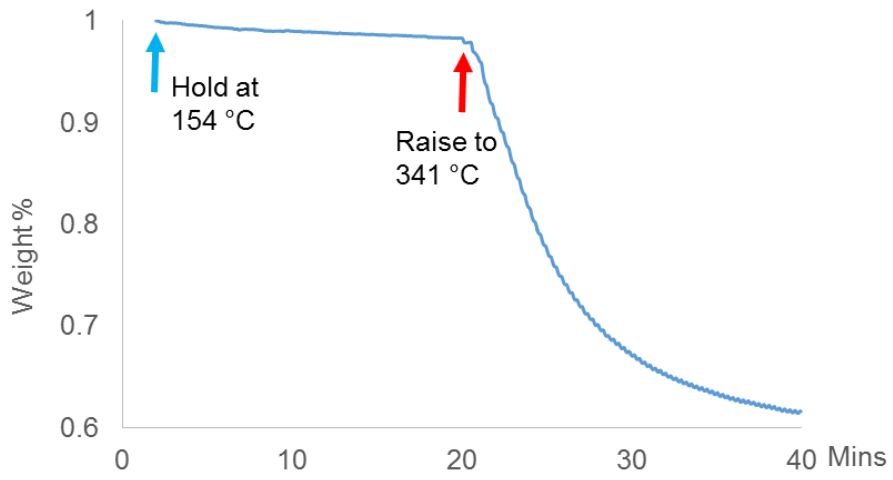

Figure 5.8 TGA of ZrO_2-MAA hold at 154 °C and 341 °C for 20 mins.

Lam Research Ex. 1013 - Page 153
Lam Research Corp. v. Inpria Corp.
IPR2025-00256 - U.S. Patent No. 11,537,048

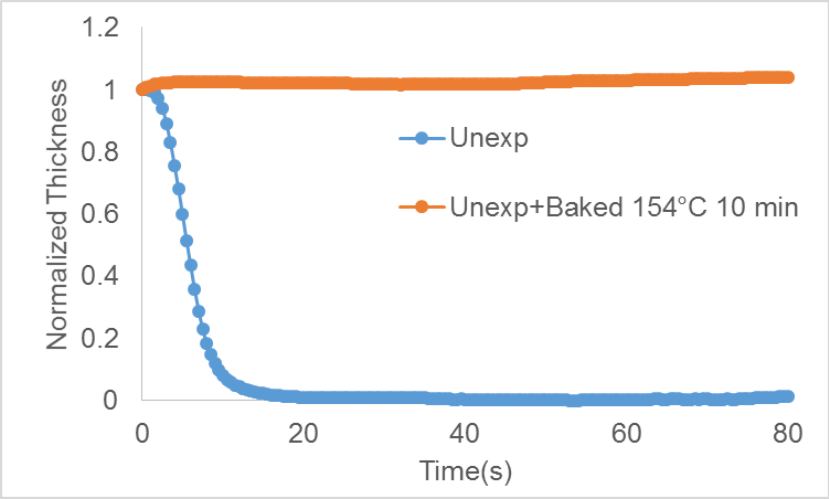

Figure 5.9 Dissolution rate of nanoparticles thin film in 4M2P before and after annealing at 154 °C measured by QCM.

As seen in Figure 5.9, nanoparticles are readily dissolved in 4M2P, a common developer, within 18 seconds. However, the film became totally insoluble even after several minutes. The enormous solubility difference despite little weight loss could be explained by either of the following three possibilities. First, the solubility is very sensitive to organic content changes. Second, large quantity of ligands although cleaved still exist in the film during heating, but nanoparticles with fewer ligands become insoluble. Third, the Zr-O-Zr network formed during heating resulted in huge solubility changes.

The first possibility may be excluded as nanoparticles of different batches synthesis have more organic content variation compared to the heated samples. However, to clarify the latter two possibilities, FTIR studies were needed to reveal the chemical environment changes during heating. From the FTIR spectra of samples heated at 154 °C for 20 minutes (Figure 5.10), we can see the majority of ligands are bound to nanoparticle surface while free MAA

Lam Research Ex. 1013 - Page 154
Lam Research Corp. v. Inpria Corp.
IPR2025-00256 - U.S. Patent No. 11,537,048

has escaped from the film since the free ligands are completely removed as the C=O stretching at 1690 cm^{-1} disappeared, the $\nu_{asy}(CO_2^-)$ at 1550 cm^{-1} and $\nu_{sy}(CO_2^-)$ at 1420 cm^{-1} decreased, while the Zr-O content (around 600 cm^{-1}) has greatly increased. From these data, we can conclude Zr-O-Zr bonds are formed during heating and cleaved MAA ligands have escaped from the film. The reason for a solubility change by nanoparticles heated to 154 °C are due to Zr-O-Zr formation rather than ligand loss.

From TGA analysis in Figure 5.8, once hold isothermally at 341 °C, which is the second weight loss peak in TGA curve, nanoparticles lost more than 35% of its total weight during the initial 10 minutes heating. This was confirmed by FTIR analysis which showed that almost all ligands were desorbed from the nanoparticle surface as the characteristic peaks of MAA disappeared and Zr-O stretching peak at 668 cm^{-1} now dominated the spectra (Figure 5.10). The two stretching peaks of 1531 cm^{-1} and 1401 cm^{-1} are CO byproducts absorbed in the nanoparticles. Those CO byproducts absorbed to nanoparticles will finally be removed from ZrO_2 at higher temperature and it is consistent with the brown color of the nanoparticles after annealing at 341 °C.

Lam Research Ex. 1013 - Page 155
Lam Research Corp. v. Inpria Corp.
IPR2025-00256 - U.S. Patent No. 11,537,048

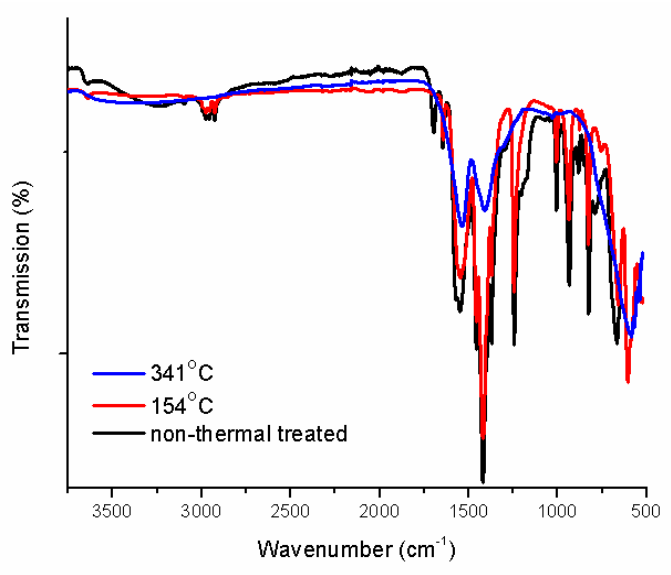

Figure 5.10 FTIR of nanoparticles sample with no thermal treatment, nanoparticles heated to 154 °C or 341 °C.

5.3.4. Effects of post-exposure bake on negative tone development process

5.3.4.1. Effects of PEB on exposure dose

ZrO_2-MAA films with 5 wt. % 3P3A PAG loading were exposed to DUV (254 nm), followed by selected PEB conditions. The thickness of the resist film after development in 4M2P for 10s was measured as shown in Figure 5.12. Films thickness after 10 s of development continued to increase with exposure dose until it reached a saturated thickness at around 120 nm which is defined as E_0. As post-exposure bake steps were applied, E_0 decreased from 150 mJ/cm^2 to 100 mJ/cm^2 (90 °C 60 s) and 25 mJ/cm^2 (130 °C 30 s).

Lam Research Ex. 1013 - Page 156
Lam Research Corp. v. Inpria Corp.
IPR2025-00256 - U.S. Patent No. 11,537,048

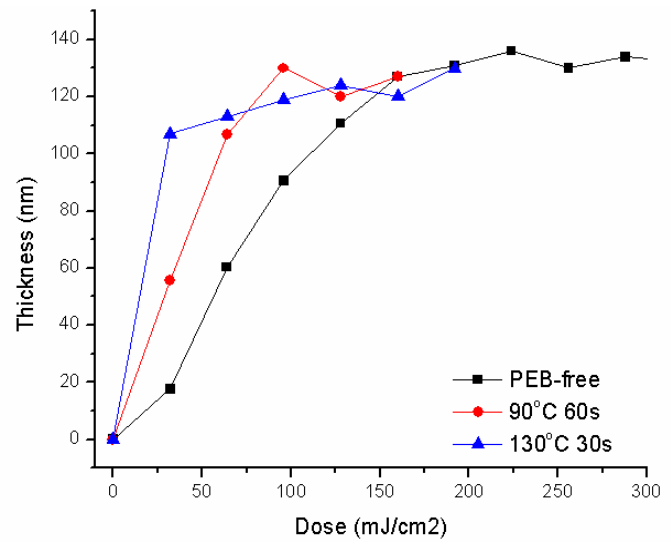

Figure 5.11 Contrast curves of ZrO_2-MAA at different PEB conditions.

5.3.4.2. Effects of PEB on film thickness and line width

ZrO_2-MAA films with 5 wt.% NI-tf PAG loading were exposed to 254 nm DUV exposure at 80 mJ/cm^2, followed by PEB and development in a 1:1 ratio 4M2P:PGMEA co-solvent for 10s. As shown in Figure 5.13, resist line width (dark part) increased as PEB temperature increased. Similar effects of PEB were also observed on HfO_2-methylvaleric acid (MVA). Without PEB, the small features of HfO_2-MVA were almost washed away during development, while PEB helps to maintain small features by increasing the thickness in the exposed region. PEB increase the film thickness through decreasing the dissolution rate. As shown in Figure 5.14, the dissolution rate decreased by three times compared to an non-exposed film, resulting in less thickness loss of negative tone patterns. During a 10s development, the thickness loss of the exposed resist decreased from 50% to 9%. The

Lam Research Ex. 1013 - Page 157
Lam Research Corp. v. Inpria Corp.
IPR2025-00256 - U.S. Patent No. 11,537,048

uncertainties of resist chemistry at the exposure boundary can be amplified by low dissolution rate contrast which corresponds to a rougher edge and top surface.

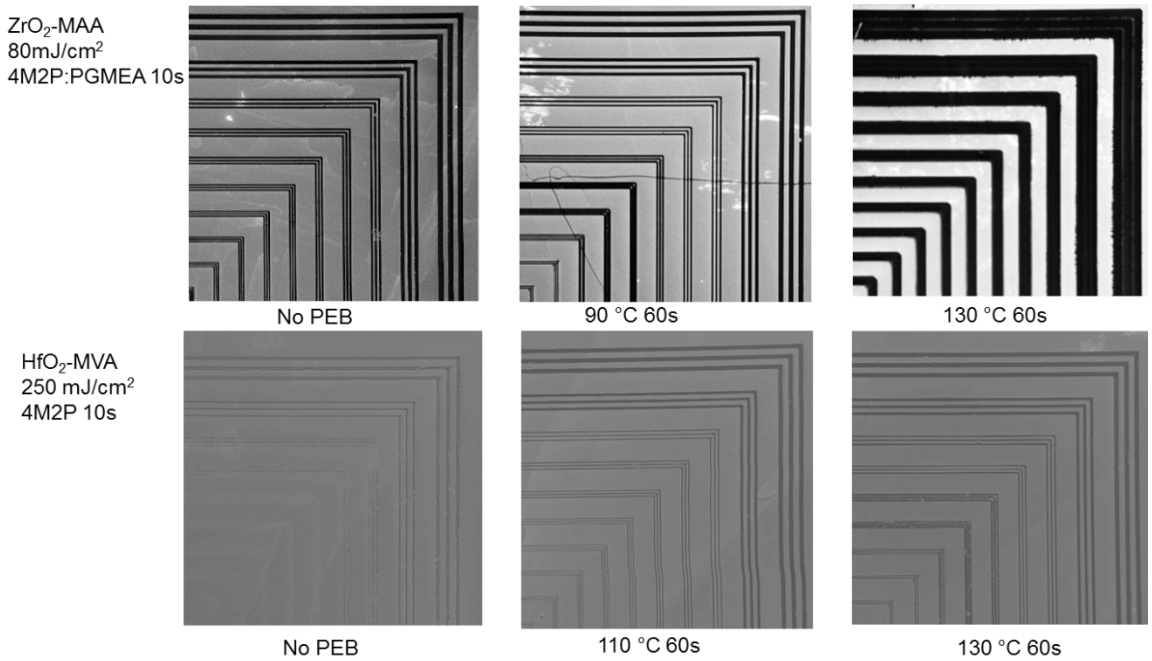

Figure 5.12 Effects of PEB on the pattern width and negative tone resist thickness.

Lam Research Ex. 1013 - Page 158
Lam Research Corp. v. Inpria Corp.
IPR2025-00256 - U.S. Patent No. 11,537,048

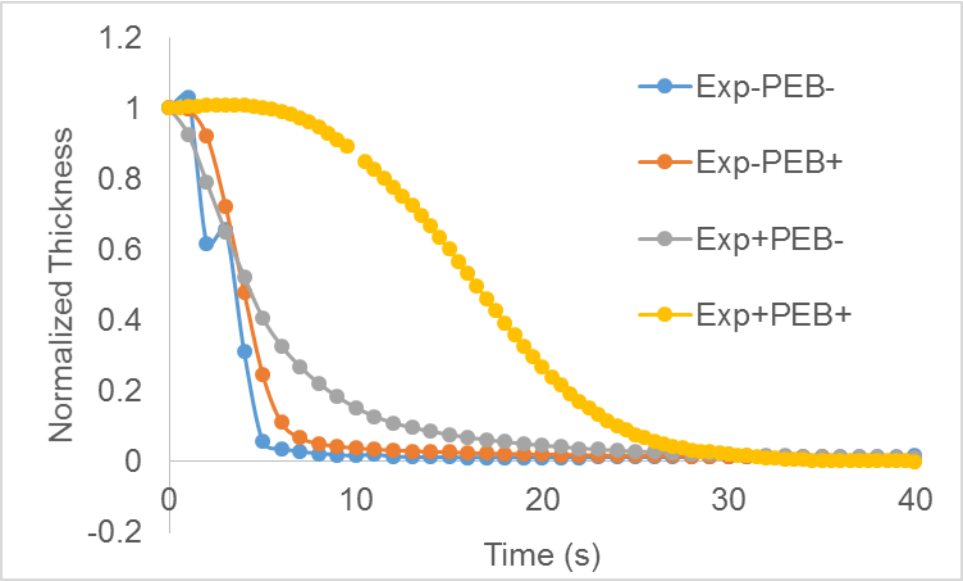

Figure 5.13 Dissolution rate of ZrO_2-MAA thin film with or without exposure and PEB.

5.3.4.3. Effects of PEB on development time

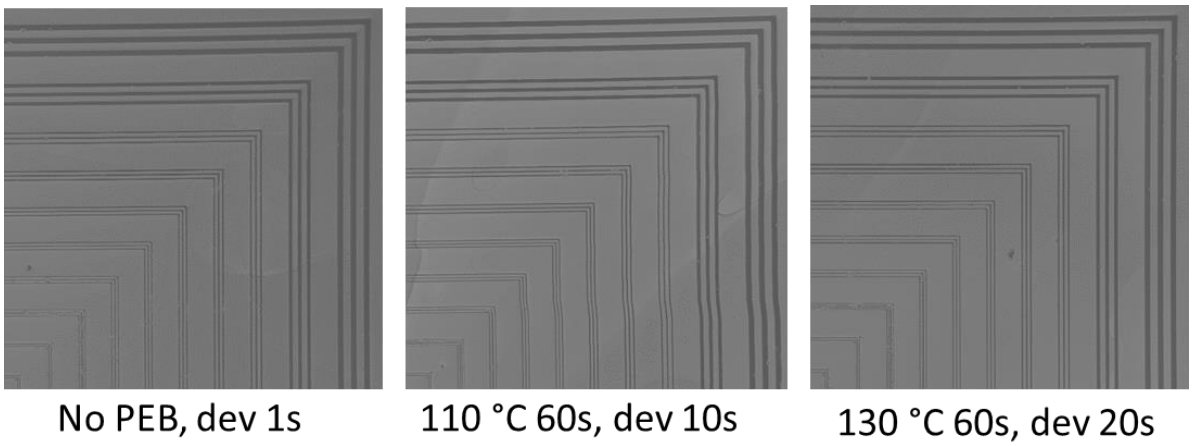

Figure 5.14 Contact aligner line space patterns of HfO2-2-methyl-2-pentenoic acid at various PEB temperatures and developed in 4M2P (250 mJ/cm2, 254 nm).

Lam Research Ex. 1013 - Page 159
Lam Research Corp. v. Inpria Corp.
IPR2025-00256 - U.S. Patent No. 11,537,048

HfO_2-MVA film with 5 wt. % NI-tf PAG loading were exposed to 254 nm DUV exposure at a dose of 250 mJ/cm^2. After exposure, these films were baked at 110 °C 60 s and 130 °C 60 s respectively and subjected to development in 4M2P. Development times were varied in order to obtain optimal patterning results. The width of resist lines in line space patterns decreased with increasing development time. Therefore, the optimized development times measured here were the optimized development times to form line patterns closest to aligner mask patterns. As seen in Figure 5.15, to achieved similar line width at the same exposure dose, the development time in 4M2P had to increase with increasing PEB time as thermal treated film became harder to remove.

5.3.5. Mechanism for the solubility switch for the cases of exposure only and of exposure with PEB

5.3.5.1. TGA and FTIR studies of ligands loss during PEB

In order to understand the effects of post-exposure bake for negative tone pattern formation, the TGA of ZrO_2-MAA before and after exposure was studied. ZrO_2-MAA samples without any PAG loading or any UV exposure were held isothermally at 110 °C and 130 °C, respectively for 20 mins heated in an open chamber and showed total 1.5% weight loss for both temperatures. From previous FTIR studies, we know this weight loss is likely due to both cleavage and outgassing of ligands. As a result, during a 60 s or even 30 s PEB process, the ligand loss should be less than 0.1%. Compared to the total of over 50% of organic content, ligand loss due to thermal effects should not lead to any solubility change unless condensation occurs.

Lam Research Ex. 1013 - Page 160
Lam Research Corp. v. Inpria Corp.
IPR2025-00256 - U.S. Patent No. 11,537,048

However, the ligand loss rate at 130 °C greatly increased after exposure. Thus a 1.5% weight loss of exposed samples occurred within 5 minutes of heating, compared to 20 minutes for unexposed samples (Figure 5.16). This increase in the ligand loss rate is probably due to a change in the local chemical environment after UV exposure. The PAG not only generates stronger ligands to replace the initial carboxylate ligands upon UV exposure, but also creates a low pH environment which may also affect nanoparticle stability.[17–19] As nanoparticles become less stable after exposure, it is more likely to lose even more ligands and the loss of ligands could potentially lead to increased formation of Zr-O-Zr we speculate takes place during heating. This change was confirmed by FTIR studies of as-spun and PEB treated samples (Figure 5.17). As particles lost more ligands and formed covalent bonds upon heating, the resist film became less soluble in developer. The higher the temperature of PEB, the higher the rate increases in ligand loss and covalent bond formation. Therefore, an E_0 decrease with pattern width, film thickness and development time increase occurred with increasing PEB temperature.

After exposure, we observed the transformation of some bound ligands to become free ligands in the film. and the Subsequent development removed any free ligands from the film, while the PEB step removed additional ligands through heating so the development after PEB doesdoes not lead to not any further decrease in ligand quantities. Therefore, the FTIR studies of samples exposed to PEB, those that were developed and those with PEB with followed by development samples showed similar decreases in the ligand compared to as-spun samples.

Lam Research Ex. 1013 - Page 161
Lam Research Corp. v. Inpria Corp.
IPR2025-00256 - U.S. Patent No. 11,537,048

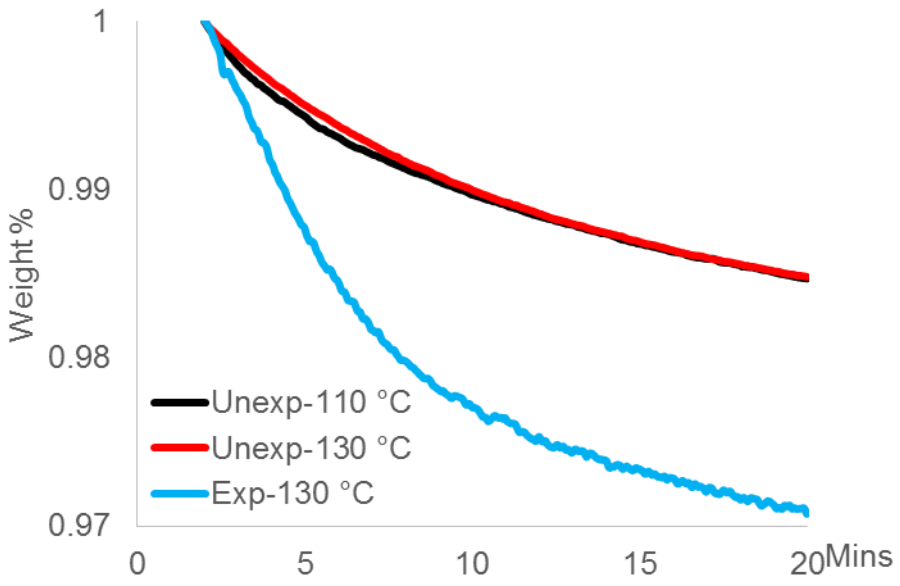

Figure 5.15 TGA of ZrO_2-MAA with 5 wt% PAG heated at 110 °C 130 °C for 20 mins before and after 150 mJ/cm2 DUV exposure.

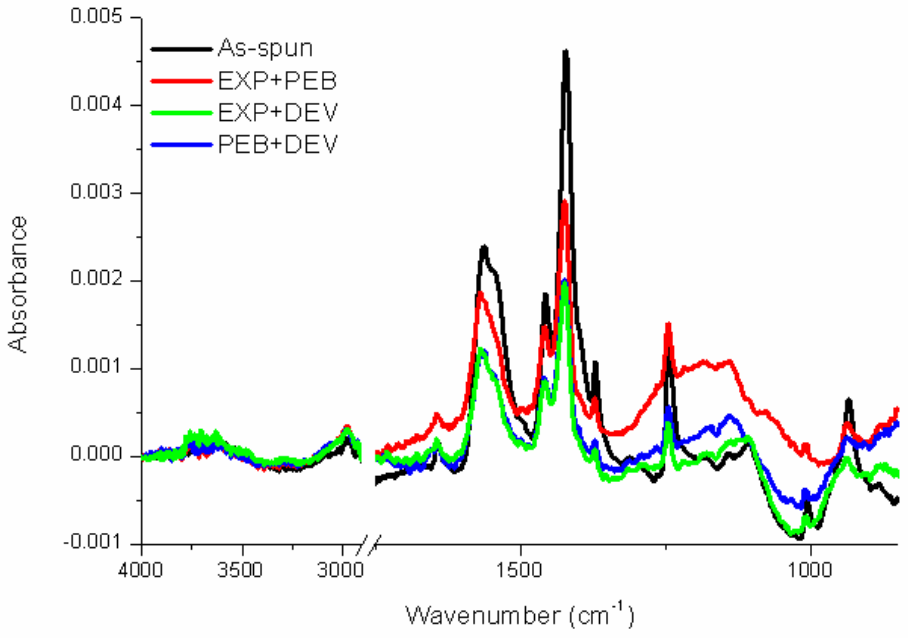

Figure 5.16 FTIR absorbance spectra of PEB and developed ONE resist film on Si

Lam Research Ex. 1013 - Page 162
Lam Research Corp. v. Inpria Corp.
IPR2025-00256 - U.S. Patent No. 11,537,048

5.3.5.2. XPS analysis

X-ray photoelectron spectroscopy (XPS) can detect atoms and their surrounding chemical environment by measuring the kinetic energy and the number of electrons escaping during X-ray irradiation. The bonding energy can be used to evaluate surrounding local environment. The O 1s region is convoluted into three components Zr-OH at 527.8 eV, Zr-O-Zr at 530.3 eV and Zr-O-CO_2^- at 531.8 eV (Figure 5.18a). As shown in Figure 5.18b, the O 1s region width decreased and the peak shifted to a lower energy corresponding to the decrease of Zr-O-C. As a consequence, Zr-O-Zr and Zr-OH components increased. However, the quantification of each component is complicated as the FWHM and peak position can greatly change the component ratio.

The statistical ratio of each atom can be used to calculate the empirical composition of materials. The atom ratio of Zr, O and C of the resist film both with and without exposure and after PEB are summarized in table 5.5. The ligand to metal ratio decrease from 1.45 to 1.40 after exposure, while the Zr-O ratio increase from 0.44 to 0.53. After PEB, the ratio of ligands to Zr decreased to 1.23 while Zr-O increase to 0.59, which is consistent with FTIR studies.

As indicated by FTIR, carboxylate ligands bind to nanoparticles through chelation. When a ligand is removed from nanoparticles, two chelating bonds break. If Zr-OH is formed, two additional oxygen atoms are needed to replace one ligand, but if a Zr-O-Zr is formed, only one oxygen is needed for one ligand. Therefore, from the XPS elemental ratio change of Zr, oxygen and ligands, we might expect that Zr-OH is formed during exposure but more ZrO_2 is formed during PEB. The formation of Zr-OH was confirmed by FTIR that Zr-OH peak

Lam Research Ex. 1013 - Page 163
Lam Research Corp. v. Inpria Corp.
IPR2025-00256 - U.S. Patent No. 11,537,048

around 3750 cm^{-1} increased upon exposure (Figure 5.18). Significant Zr-O-Zr network growth did not occurred as the DLS showed that the nanoparticles size remained the same after exposure (Figure 5.19).

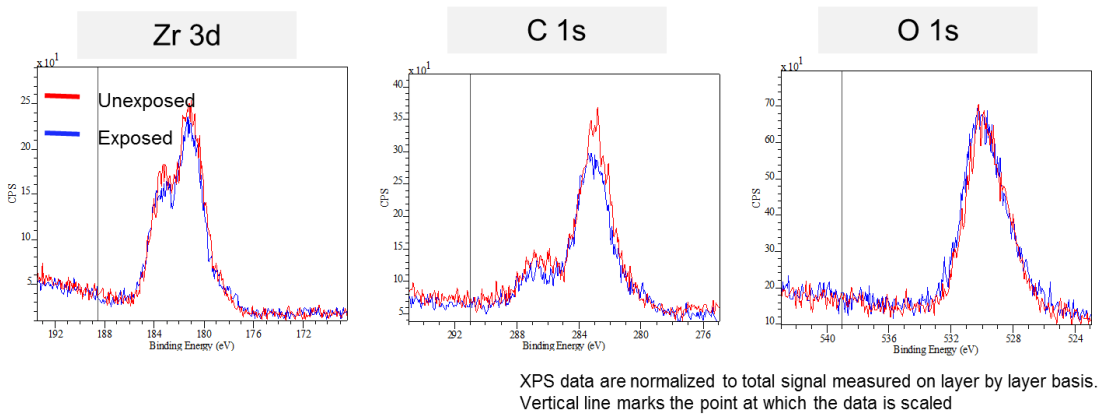

Figure 5.17 XPS spectra of unexposed and exposed ZrO_2-MAA film. a) Zr 3d region b) C 1s region, c) O 1s region.

Table 5.1 Elemental ratio of ZrO_2-MAA films by XPS

Elements ratio (%)	Unexpose	Exposed	PEB
C	57.15	56.35	54.94
O	32.96	33.51	33.98
Zr	9.88	10.08	11.08
Overall	$ZrO_{0.44}$ $MAA_{1.45}$	$ZrO_{0.53}$ $MAA_{1.40}$	$ZrO_{0.59}$ $MAA_{1.23}$

Lam Research Ex. 1013 - Page 164
Lam Research Corp. v. Inpria Corp.
IPR2025-00256 - U.S. Patent No. 11,537,048

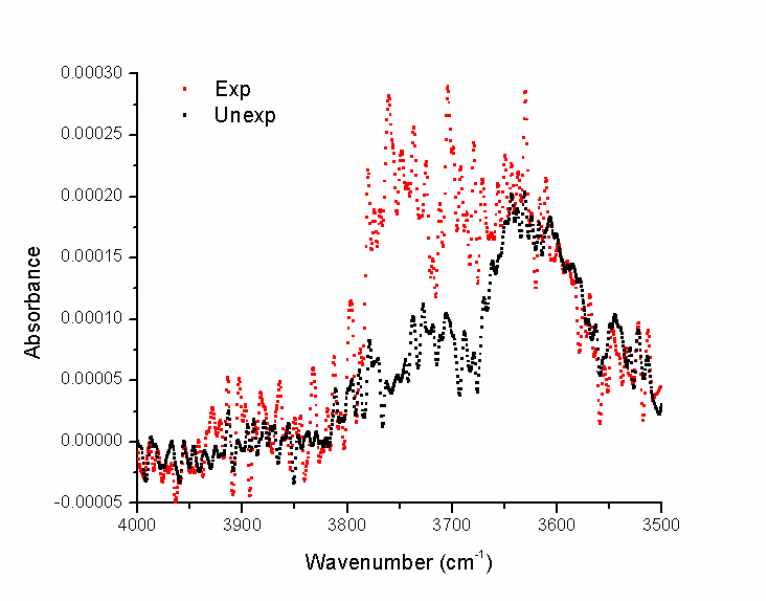

Figure 5.18 FTIR of ZrO_2-MAA exposed and unexposed samples. Zr-OH absorbance between 3600 cm^{-1} -3800 cm^{-1} increase after exposure.

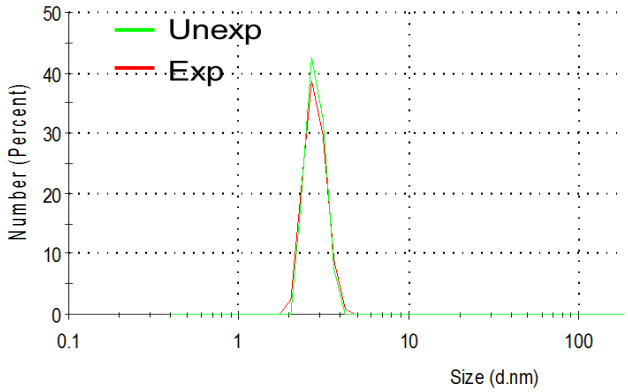

Figure 5.19 Nanoparticle hydrodynamic size distribution with and without exposure.

In summary, the patterning results demonstrate that PEB is effective in decreasing the dose and increasing the dissolution rate difference and this improves the resist sensitivity and could potentially decrease LWR. A mechanistic analysis revealed that PAG not only provided a

Lam Research Ex. 1013 - Page 165
Lam Research Corp. v. Inpria Corp.
IPR2025-00256 - U.S. Patent No. 11,537,048

stronger anion for ligand exchange, but also facilitate direct ligand removal from nanoparticles by EUV radiation. When ligands are removed, hydroxyl groups formed, therefore nanoparticles size after exposure does not change significant. In contrast, condensation of Zr-OH occurs during PEB, so the growth of more stable ZrO_2 network leads to dramatic changes in solubility and an increase in pattern width. Moreover, since some OH groups also exist in an unexposed resist, condensation in the unexposed regions could also happen to a lesser extent than exposed regions, but still resulting in longer developing time.

The formation of a Zr-O network is a chemically random process which not only forms in the exposed region but also at the exposure boundary. This uncertainty of Zr-O network formation is possibly detrimental to critical dimension uniformity and high resolution dense patterns. In comparison, film exposed without PEB mainly generated Zr-OH after ligand cleavage which more faithfully transfers mask patterns, yet for many systems exposure does not create enough difference in the dissolution rate. This work provides a fundamental understanding of the patterning mechanism. In future, more studies on ligand cleavage and Zr-O formation kinetics will be required to better optimize the dose and PEB to obtain high resolution, low roughness and high resist profile contrast patterns.

5.4. Conclusion

This chapter presents the characterization of HfO_2 and ZrO_2 nanoparticles stabilized by MAA ligands. These particles have narrow size distribution with an average diameter of 1.5 nm measured by SAXS and contains ~ 45 wt. % to 65 wt. % organic content. FTIR studies showed that ligands are bound to nanoparticles using mostly chelating and partially bridging

Lam Research Ex. 1013 - Page 166
Lam Research Corp. v. Inpria Corp.
IPR2025-00256 - U.S. Patent No. 11,537,048

configuration. The XPS studies showed that Zr is in the +4 oxidized state and the empirical composition is $ZrO_{0.44}MAA_{1.45}$. Both Zr-OH and Zr-O-Zr exist in the nanoparticle compositions.

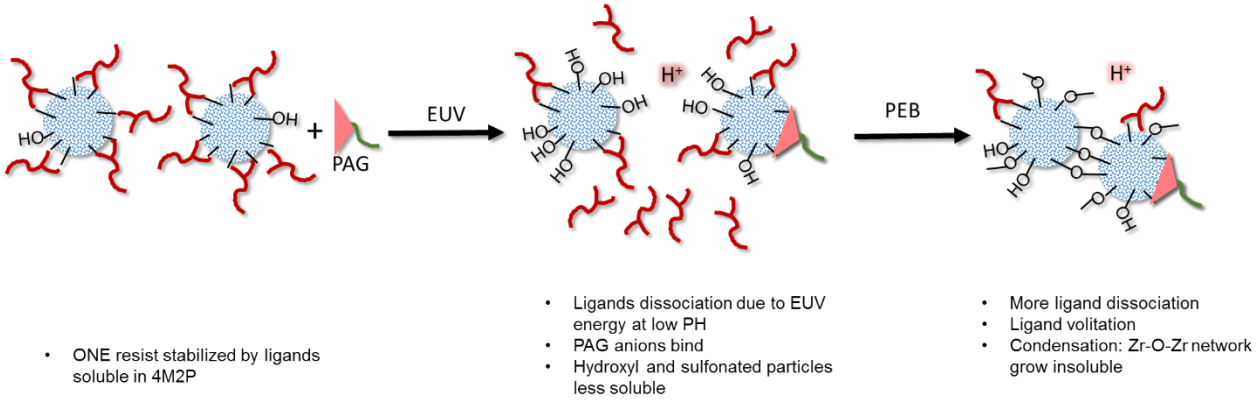

Figure 5.20 Schematic plot of Negative tone patterning mechanism of ONE resist.

TG/DTA studies revealed that nanoparticles have two maximum weight loss rate peaks during the entire heating process. The first peak corresponds to an endothermic process of ligand cleavage and ligand outgassing and the second peak corresponds to complete ligand removal and exothermic processes of byproduct decomposition. Although less than 5% of the weight is lost during an isothermal heating at 154 °C, nanoparticles became totally insoluble in 4M2P through the loss of ligand and the formation of Zr-O-Zr bounds.

XPS and FTIR studies revealed a more comprehensive negative tone mechanism as shown in Figure 5.19. High energy EUV photons were able to directly kick off ligands and change the

Lam Research Ex. 1013 - Page 167
Lam Research Corp. v. Inpria Corp.
IPR2025-00256 - U.S. Patent No. 11,537,048

polarity of the nanoparticles. The majority of EUV photons were consumed for direct ligand dissociation and reduced energy to DUV region. These secondary electrons are strongly absorbed by the PAG as it is more sensitive to DUV wavelength. After UV decomposition of the PAG, anion byproducts bind to the nanoparticles and the low pH environment caused more ligand dissociation. Therefore, nanoparticles with less carboxylic acid, more triflate and OH groups became less soluble in developer. In addition, the PEB step enables condensation reactions to take place, therefore the growing Zr-O-Zr network formation drastically changes solubility of ONE resists and leads to resist line width increases. Although condensation during PEB reduces the thickness loss during negative tone development, the uncertainty of Zr-O-Zr is likely to induce uncertainty in line width or roughness.

Reference

(1) Wu, B.; Kumar, A. Extreme Ultraviolet Lithography: A Review. Journal of Vacuum Science & Technology B: Microelectronics and Nanometer Structures, 2007, 25, 1743.

(2) Wagner, C.; Harned, N. EUV Lithography: Lithography Gets Extreme. Nat. Photonics 2010, 4, 26.

(3) Pirati, A.; Peeters, R.; Smith, D.; Lok, S.; Minnaert, A.; van Noordenburg, M.; Mallmann, J.; Harned, N.; Stoeldraijer, J.; Wagner, C.; et al. Performance Overview and Outlook of EUV Lithography Systems . In; 2015; Vol. 9422, p. 94221P – 94221P – 18.

(4) Mizoguchi, H.; Nakarai, H.; Abe, T.; Nowak, K. M.; Kawasuji, Y.; Tanaka, H.; Watanabe, Y.; Hori, T.; Kodama, T.; Shiraishi, Y.; et al. Performance of One Hundred Watt HVM LPP-EUV Source . In; 2015; Vol. 9422, p. 94220C – 94220C – 13.

(5) Van Setten, E.; Schiffelers, G.; Psara, E.; Oorschot, D.; Davydova, N.; Finders, J.; Depre, L.; Farys, V. Imaging Performance and Challenges of 10nm and 7nm Logic Nodes with 0.33 NA EUV . In; 2014; Vol. 9231, pp. 923108–923114.

(6) George, S. A.; Naulleau, P. P. Out of Band Radiation Effects on Resist Patterning. In Proc. of SPIE; 2011; Vol. 7969, pp. 796911–796914.

Lam Research Ex. 1013 - Page 168
Lam Research Corp. v. Inpria Corp.
IPR2025-00256 - U.S. Patent No. 11,537,048

(7) Krysak, M.; Trikeriotis, M.; Schwartz, E.; Lafferty, N.; Xie, P.; Smith, B.; Zimmerman, P.; Montgomery, W.; Giannelis, E.; Ober, C. K. Development of an Inorganic Nanoparticle Photoresist for EUV, E- Beam and 193 Nm Lithography. In Proc. of SPIE; Allen, R. D.; Somervell, M. H., Eds.; 2011; Vol. 7972, p. 79721C – 79721C – 6.

(8) Hubbell, J. H.; Veigele, W. J.; Briggs, E. A.; Brown, R. T.; Cromer, D. T.; Howerton, R. J. Erratum: Atomic Form Factors, Incoherent Scattering Functions, and Photon Scattering Cross Sections. J. Phys. Chem. Ref. Data 1977, 6.

(9) Hubbell, J. H.; Veigele, W. J.; Briggs, E. a.; Brown, R. T.; Cromer, D. T.; Howerton, R. J. Atomic Form Factors, Incoherent Scattering Functions, and Photon Scattering Cross Sections. Journal of Physical and Chemical Reference Data, 1975, 4, 471–538.

(10) Trikeriotis, M.; Krysaki, M.; Chung, Y. S.; Ouyang, C.; Cardineau, B.; Brainard, R.; Ober, C. K.; Giannelis, E. P.; Cho, K. Nanoparticle Photoresists from HfO_2 and ZrO_2 for EUV Patterning. J. Photopolym. Sci. Technol. 2012, 25, 583–586.

(11) Kryask, M.; Trikeriotis, M.; Ouyang, C.; Chakrabarty, S.; Giannelis, E. P.; Ober, C. K. Nanoparticle Photoresists: Ligand Exchange as a New, Sensitive EUV Patterning Mechanism. J. Photopolym. Sci. Technol. 2013, 26, 659–664.

(12) Krysak, M. E. Small Molecule Photoresist Materials for next Generation Lithography. Ph.D. Dissertation, Cornell University, 2013.

(13) Krysak, M. E.; Blackwell, J. M.; Putna, S. E.; Leeson, M. J.; Younkin, T. R.; Harlson, S.; Frasure, K.; Gstrein, F. Investigation of Novel Inorganic Resist Materials for EUV Lithography. In Proc. of SPIE; 2014; Vol. 9048, pp. 904805–904807.

(14) Trimmel, G.; Gross, S.; Kickelbick, G.; Schubert, U. Swelling Behavior and Thermal Stability of Poly(methylmethacrylate) Crosslinked by the Oxozirconium Cluster Zr4O2(methacrylate)12. Appl. Organomet. Chem. 2001, 15, 401–406.

(15) Sanchez, C.; Livage, J.; Henry, M.; Babonneau, F. Chemical Modification of Alkoxide Precursors. J. Non. Cryst. Solids 1988, 100, 65–76.

(16) Nakamoto, K. Infrared and Raman Spectra of Inorganic and Coordination Compounds; 1986; Vol. 85.

(17) Badawy, A. M. El; Luxton, T. P.; Silva, R. G.; Scheckel, K. G.; Suidan, M. T.; Tolaymat, T. M. Impact of Environmental Conditions (pH, Ionic Strength, and Electrolyte Type) on the Surface Charge and Aggregation of Silver Nanoparticles Suspensions. Environ. Sci. Technol. 2010, 44, 1260–1266.

Lam Research Ex. 1013 - Page 169
Lam Research Corp. v. Inpria Corp.
IPR2025-00256 - U.S. Patent No. 11,537,048

(18) Yu, S.; Chow, G. M. Carboxyl Group (– CO 2 H) Functionalized Ferrimagnetic Iron Oxide Nanoparticles for Potential Bio-Applications. J. Mater. Chem. 2004, 14, 2781–2786.

(19) Pettibone, J. M.; Cwiertny, D. M.; Scherer, M.; Grassian, V. H. Adsorption of Organic Acids on TiO2 Nanoparticles: Effects of pH, Nanoparticle Size, and Nanoparticle Aggregation. Langmuir 2008, 24, 6659–6667.

Lam Research Ex. 1013 - Page 170
Lam Research Corp. v. Inpria Corp.
IPR2025-00256 - U.S. Patent No. 11,537,048

CHAPTER 6 NEW LIGAND COMPOSITIONS FOR METAL OXIDE NANOPARTICLE EUV RESIST

6.1. Introduction

Ligand stabilized metal oxide nanoparticle EUV (ONE) resists are among the most promising EUV resists presently being investigated due to their extraordinary sensitivity. These non-chemically amplified resists utilize a novel patterning mechanism to achieve a solubility change after exposure as discussed in detail in Chapter 5. Ligands are bound to metal oxide nanoparticles in chelating or bridging configurations and they are directly removed by EUV radiation in a low pH environment. Ligand exchange with photoacid generator (PAG) anions and formation of a hydroxide surface upon radiation exposure results in a solubility switch in organic developer, thus forming negative tone patterns.

The EUV sensitivity of ONE resists strongly depends on ligand binding strength. In an earlier study, ZrO_2 or HfO_2 nanoparticles with benzoic acid, methacrylic acid (MAA), isobutyric acid (IBA) and trans-2,3-dimethylacrylic acid (DMA) showed increasing EUV sensitivity with increasing pKa values.[1–4] In order to verify this hypothesis, nanoparticles with aromatic ligands in a wide pK_a range were synthesized including bromobenzoic acid, nitrobenzoic acid, o-toluic acid and p-toluic acid.[5] EUV patterning of both p-toluic acid and bromobenzoic acid required doses of 40 mJ/cm^2 and higher, suggesting EUV sensitivity is determined not only by pK_a but by other factors as well.

Lam Research Ex. 1013 - Page 171
Lam Research Corp. v. Inpria Corp.
IPR2025-00256 - U.S. Patent No. 11,537,048

In this chapter, nanoparticles with 12 different ligands with a broad range of pK_a values were synthesized to compare their structural effects on patterning sensitivities. These 12 aliphatic ligands include saturated and unsaturated groups with linear and branched carboxylic acids having 3-6 carbon atoms. In order to study the ligand binding strength, we utilized thermal energy to cleave off ligands and dynamic thermogravimetric analysis (TGDTA) to record the heat flow accompanied by these reactions. In addition to ligand biding strength, the development process which affects sensitivity and pattern quality was studied. Quartz crystal microbalance (QCM) was utilized to measure the dissolution rate change after exposure and deep ultraviolet (DUV) patterning. Other process considerations such as base quenchers, aging effects and manufacturing compatible development method were also evaluated for ONE resists in this chapter.

6.2. Experimental

6.2.1. Materials

All reagent materials were purchased from Sigma Aldrich and were used as received. All solvents were purchased from fisher science and were used as received.

6.2.2. Nanoparticles synthesis

6.2.2.1. 2-methyl-2-pentenoic acid stabilized hafnium oxide nanoparticles

3 g (12 mmol) of either hafnium or zirconium isopropoxide was added to 25 mL of THF to a three-necked round-bottomed flask fitted with a condenser. The mixture was stirred for 15

Lam Research Ex. 1013 - Page 172
Lam Research Corp. v. Inpria Corp.
IPR2025-00256 - U.S. Patent No. 11,537,048

minutes at room temperature before raise the temperature to 65 °C. After equilibrating for 15 minutes, 3 ml of 1: 5 deionized (DI) water and acid mixture was added to the mixture drop by drop and the solution turned clear. After 18 hours, another 3 ml of 1: 5 deionized (DI) water and acid mixture was added. After 3 hours, the solution was cooled and 5 times water by volume was added. The mixture was centrifuged at 8000 rpm for 8 minutes. The solvents were then decanted and 5 ml of nanoparticles were then washed with 36 ml 1:1 methanol water solution and centrifuged at 8000 rpm for 8 minutes. This washing step was repeated twice to remove unreacted acid. Precipitate was collected and dried in a vacuum oven at 65 °C overnight. 1.5-2 g of white power was obtained.

Crotonic acid, 2,3-dimethylacrylic acid and 3,3-dimethylacrylic acid stabilized hafnium oxide nanoparticles were synthesized using this method.

6.2.2.2. 2-Methylpentanoic acid stabilized hafnium oxide nanoparticles

3 g (12 mmol) of either hafnium or zirconium isopropoxide was added to 12 mL of 2-Methylpentanoic acid to a three-necked round-bottomed flask fitted with a condenser. The mixture was stirred for 15 minutes before raise the temperature to 65 °C. After equilibrating for 90 minutes, 1 ml of deionized (DI) water was added to the mixture drop by drop and the solution turns clear. After reacting for 18 hours, the solution was cooled down and then was added 5 times of 1:1 water methanol by volume. The mixture was centrifuged at 8000 rpm for 8 minutes. The solvents were decanted. Then 5 ml of nanoparticles was then washed with 36 ml water or 1:1 methanol water solution and centrifuged at 8000 rpm for 8 minutes twice.

Lam Research Ex. 1013 - Page 173
Lam Research Corp. v. Inpria Corp.
IPR2025-00256 - U.S. Patent No. 11,537,048

Precipitate was collected and dried in a vacuum oven at 65 °C overnight. 1.5-2 g of white power was obtained.

Propionic acid, acrylic acid, butyric acid, isobutyric acid, 2-methyl butyric acid, methacrylic acid, 3-methylbutanoic acid, methoxy benzoic acid were synthesized using this method.

6.2.3. Physical characterization

6.2.3.1. Dynamic light scattering

1 wt. % nanoparticle dry powders was dissolved in PGMEA and filtered through 0.2 μm PTFE filters. The averaged particles dynamic size was measured with a Malvern Zetasizer Nano-ZS for dynamic light scattering at room temperature.

6.2.3.2. Thermogravimetric analysis

Thermal analysis was performed in a TA instrument Q500 thermal gravimetric analyzer (TGA) or an Exstar TG/DTA 6200 (Seiko Instruments, Inc., Torrance, CA) at the heating rate of 10 °C/min under N_2.

6.2.3.3. Chemical characterization

Transmittance or absorbance FT-IR spectra of nanoparticle dry powders were obtained by using Mattson Instruments Galaxy 2020 FT-IR spectrometer in ATR mode.

6.2.3.4. Dissolution rate measurement

Lam Research Ex. 1013 - Page 174
Lam Research Corp. v. Inpria Corp.
IPR2025-00256 - U.S. Patent No. 11,537,048

Dissolution rate of nanoparticle film in developer was measured by an Inficon Quartz crystal microbalance. 10 wt. % of resist solution was spin coated to a clean quartz crystal. After the crystal was placed in the oscillator, the frequency changes was started to log. Then the oscillator was dipped in to slowly stirred developer. The frequency change recorded during the development process, which is directly proportional to the mass of the film on the crystal according to Sauerbrey equation below. Using this equation, the changes in frequency are converted into film thickness. The thickness change versus time during the process was normalized.

$$\Delta f = -\Delta m \frac{2f^2}{A\sqrt{\rho_q \mu_q}}$$

Here, Δf = frequency change, f = resonant frequency (Hz), A = area, ρ_q = quartz density μ_q = quartz shear modulus, and Δm = mass change.

6.2.3.5. Negative tone process by DUV lithography

5 wt. % of n-hydroxynaphthanene triflate with respect to nanoparticle powders was dissolved in PGMEA to form a 5 wt. % solution. After sonication for 5 minutes, the solution was filtered through 0.2 μm PTFE filters and spun coated on to unprimed wafer at 4000 rpm for 60 s, followed by a post-apply bake at 110 °C for 60 s. After exposed to DUV radiance at 248 nm, the resist films were developed in PGMEA and 4-methyl-2pentonl mix solvents and blow-dried. The ratio of two solvents and the development time were optimized for each nanoparticle to get the best contrast and imaging result. Post-exposure bake is not necessary unless noted anywhere.

Lam Research Ex. 1013 - Page 175
Lam Research Corp. v. Inpria Corp.
IPR2025-00256 - U.S. Patent No. 11,537,048

6.2.3.6. EUV lithography

EUV exposure were performed using the SEMATECH 0.3-NA extreme ultraviolet (EUV) microlithography tool in the advance light source of Lawrence Berkeley National Lab. The solution preparation is the same as the DUV patterning. The spin coating speed was adjusted to form a uniform film at 40 nm with ±10 % variation.

6.2.3.7. Imaging process

The SEM images were taken using Keck SEM at 0.8 kV without Au/Pd sputtering. The CD and LER were calculated using SuMMIT image analysis software (EUV technology, Martinez, CA).

6.3. Results and discussion

6.3.1. Synthesis

The s procedure for ZrO_2 or HfO_2 nanoparticle synthesis using the 12 different ligands of this study was adapted from previous protocols[4] with some modification. No significant differences were observed between ZrO_2 and HfO_2 nanoparticles. However, carboxylic acids with different polarities affected the synthesis. Normally, acetone (7 ml) was added to reaction mixture after first precipitation to dissolve unreacted acid and nanoparticles. When water (35 ml) was added, acetone and the carboxylic acid became miscible with water and the nanoparticles precipitated. However, carboxylic acids with longer carbon chains are less polar and thus immiscible with water. Nanoparticles and acetone were all in the oil phase and did

Lam Research Ex. 1013 - Page 176
Lam Research Corp. v. Inpria Corp.
IPR2025-00256 - U.S. Patent No. 11,537,048

not precipitate in water. Therefore, a 1: 1 mixture of methanol and water solution in place of pure water was added to allow the carboxylic acid to become miscible with the solution and the nanoparticles eventually precipitated.

6.3.2. Characterization

After synthesis, nanoparticle sizes were measured with both small angle X-ray scattering (SAXS) and dynamic light scattering (DLS). SAXS studies showed all these nanoparticles were amorphous and that the and correlation distance between the nanoparticles metal oxide cores was ~1.4-1.5 nm. However, due to the insolubility of HfO_2 nanoparticles with acrylic acid (AA) and propionic acid (PA) in PGMEA or 2-butanone, these two nanoparticles did not proceed to further DLS investigation or lithographic evaluation. The size of the HfO_2 nanoparticles made with crotonic acid (CTA), 2,3-dimethylacrylic acid (DMA) and 3,3-dimethylacrylic acid (SA), butyric acid (BUA), isobutyric acid (IBA), 2-methyl butyric acid (IPA), methacrylic acid (MAA), 3-methylbutanoic acid (IVA), 2-methylpentanoic acid (MVA) and 2-methyl-2-pentenoic acid (MPA) acid were around 2-5 nm by DLS. These ligand structures are summarized in Figure 6.1.

FTIR spectroscopy showed that ligands were successfully bound to HfO_2 cores, as C=O stretching peaks shifted to lower wave number and split into $\nu_{asy}(CO_2^-)$ and $\nu_{sy}(CO_2^-)$. The wavenumber difference between $\nu_{asy}(CO_2^-)$ and $\nu_{sy}(CO_2^-)$ are around 100-150 cm^{-1}, suggesting the binding configuration were mostly chelating with some bridging (Figure 6.2).

Lam Research Ex. 1013 - Page 177
Lam Research Corp. v. Inpria Corp.
IPR2025-00256 - U.S. Patent No. 11,537,048

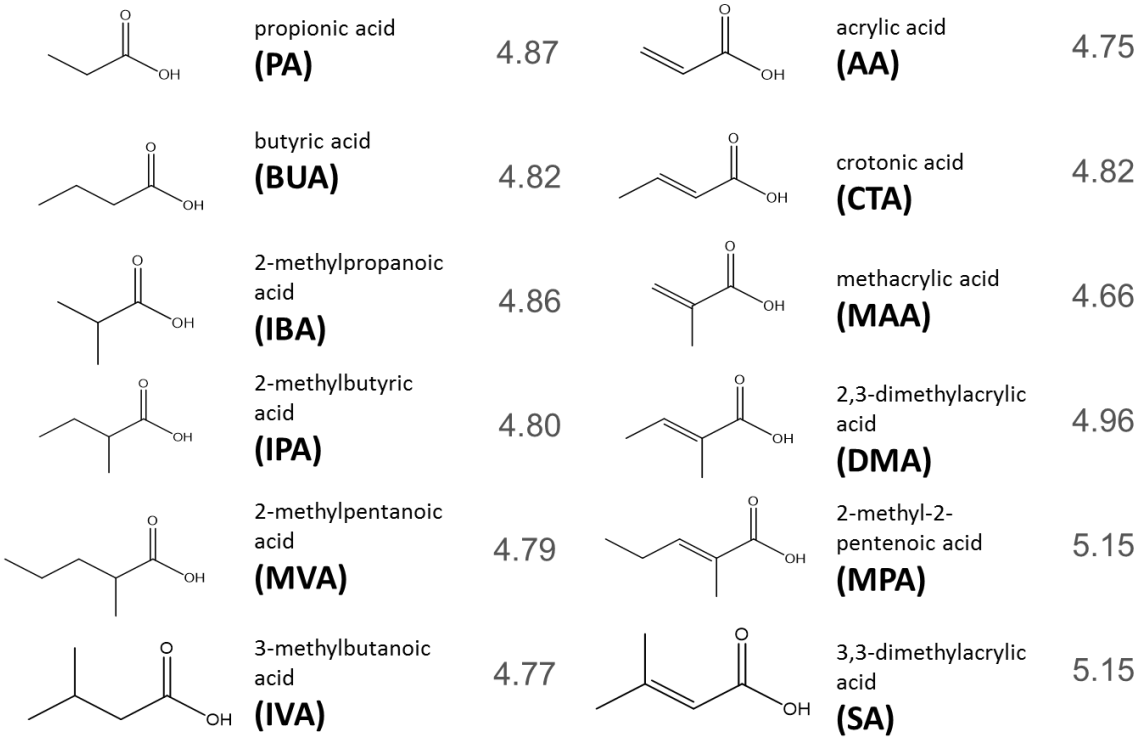

Figure 6.1 Chemical structures of ligands for solubility tests.

Lam Research Ex. 1013 - Page 178
Lam Research Corp. v. Inpria Corp.
IPR2025-00256 - U.S. Patent No. 11,537,048

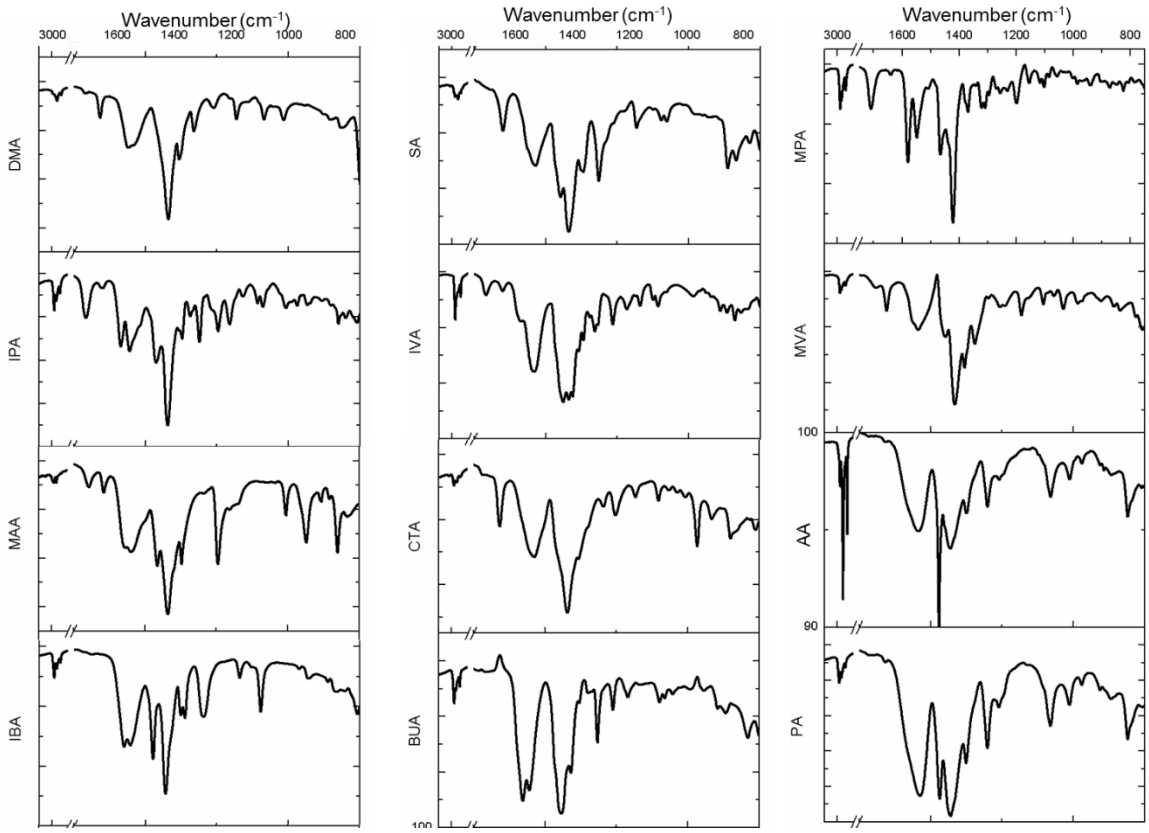

Figure 6.2 FTIR spectra of HfO_2 nanoparticles with 12 different ligands.

6.3.3. Ligand binding strength measured by TG/DTA

The TGA studies showed that these nanoparticles contained between 30%-65% organic content depending on the composition (Figure 6.3). Some difference was due to the different molecule weight of these ligands and some difference was due to batch-to-batch variation however they did not show significant differences in solubility in PGMEA. HfO_2-MPA had higher organic content due to the presence of free acids as shown in FTIR spectra (Figure 6.3). MPA is less polar compared to other ligands, thus more acetone washing is required to remove free acid from these nanoparticles.

Lam Research Ex. 1013 - Page 179
Lam Research Corp. v. Inpria Corp.
IPR2025-00256 - U.S. Patent No. 11,537,048

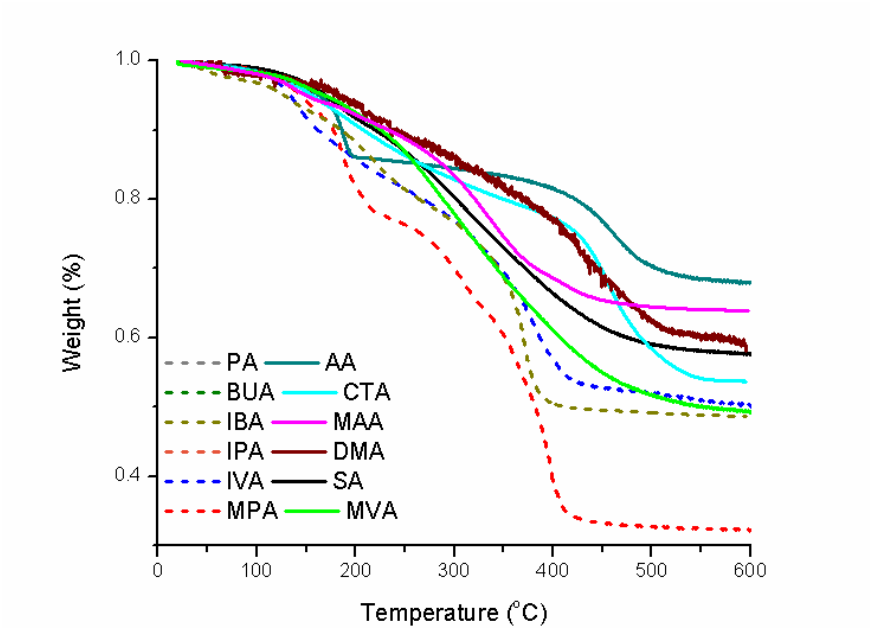

Figure 6.3 TGA of HfO_2 nanoparticles with 12 different ligands.

Free ligand volatilization is a continuous physical process upon heating and at its boiling point almost all free ligands have escaped from the film. However, loss of ligands that are covalently bound only occurred at higher temperatures when sufficient energy is provided to break bonds. As shown in Figure 6.4, differential thermogravimetry (DTG) showed two characteristic peaks: one occurs around 150 °C with a small weight loss and the other, a more significant change occurs above 300 °C. Mass-spectra coupled TGA studies of deconate-protected Ag particles also have been reported to show a two-stage ligand desorption.[6] These two ligand loss stages were attributed to different binding sites on the Ag nanoparticle surface. In our nanoparticle system, FTIR data (Figure 6.2) showed ligands bind to nanoparticles mostly using chelating and some bridging configuration, therefore we can also expect both weight loss peaks could possibly arise from ligand removal from two binding configurations.

Lam Research Ex. 1013 - Page 180
Lam Research Corp. v. Inpria Corp.
IPR2025-00256 - U.S. Patent No. 11,537,048

In order to study ligand binding strength, we measured the first ligand loss onset temperature (T_1) and the maximum ligand loss temperature (T_2) for these 12 nanoparticles using TGDTA (Table 6.1 and Table 6.6.2). T_1 of the nanoparticles with unsaturated ligands and aromatic ligands was higher than that of the nanoparticles with saturated ligands. However, nanoparticles with unsaturated ligands showed progressive weight loss during the entire heating process and T_2 was closer to T_1 (Figure 6.4). In contrast, nanoparticles with saturated ligands or aromatic ligands showed a sharp ligand loss peak at T_2. T_2 of the aromatic ligands was more than 100 °C higher than that of the aliphatic ligands which might be correlated with their lower EUV sensitivity.

Lam Research Ex. 1013 - Page 181
Lam Research Corp. v. Inpria Corp.
IPR2025-00256 - U.S. Patent No. 11,537,048

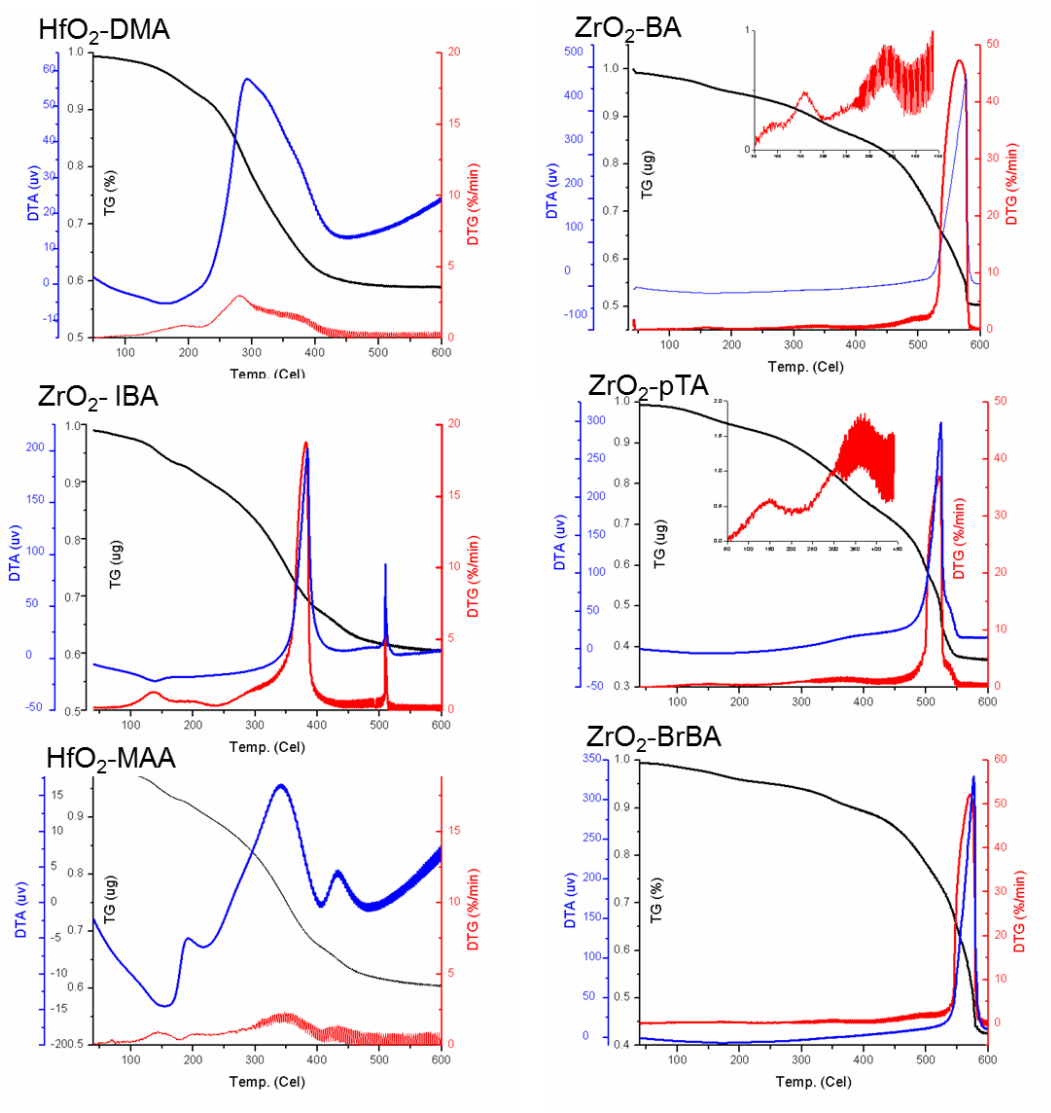

Figure 6.4 TG/DTA/DTG analysis of nanoparticles with aliphatic and aromatic ligands.

The weaker the ligands bound to nanoparticles, the higher sensitivity of the nanoparticle resists was observed. Consequently, EUV sensitivity of nanoparticles with various ligands is likely to follow the trend of their thermal ligand cleavage temperature T_2. Yet, EUV lithography evaluation with more nanoparticles is required to further confirm this hypothesis. Ligand binding strength is not only determined by ligand structures, but also many other

Lam Research Ex. 1013 - Page 182
Lam Research Corp. v. Inpria Corp.
IPR2025-00256 - U.S. Patent No. 11,537,048

factors such as metal species, steric effects, electron donation, π vs. δ interactions etc[7,8]. In addition, as mentioned in the previous chapter, PAG loading and UV exposure could facilitate the ligand removal process, thus the evaluation of acid catalysis effects on ligand cleavage is also important.

Table 6.1 First ligand loss onset temperature of nanoparticles with aromatic (aromatic) ligands.

Ligand (aromatic)	Endothermic peak	Ligand (saturated)	Endothermic peak	Ligand (unsaturated)	Endothermic peak
BA	164	PA	156	AA	189
p-MOBA	148	BUA	149	CTA	156
BrBA	176	IBA	144	MAA	154
p-TA	157	IPA	149	DMA	165
o-TA	158	MVA	187	MPA	140
PAA	149	IVA	136	SA	168

Table 6.6.2 Maximum ligand loss temperature of nanoparticles. .

Ligand (aromatic)	Exothermic peak	Ligand (saturated)	Exothermic peak	Ligand (unsaturated)	Exothermic peak
BA	565	PA	362	AA	460
p-MOBA	460	BUA	377	CTA	293
BrBA	571	IBA	374	MAA	341
p-TA	521	IPA	363	DMA	282
o-TA	483	MVA	390	MPA	301
PAA	525	IVA	376	SA	295

The unique aspect of ONE resists is their utilization of EUV photons which might give rise to their extraordinary EUV sensitivity and much lower DUV sensitivity. ONE resists are able to directly take up EUV photons to break the metal-ligand bonds[9]. Although DUV radiation is also able to break these bonds, a much higher dose is required. In contrast, chemically amplified resists (CAR) are not as sensitive to EUV radiation as to DUV radiation. DUV

Lam Research Ex. 1013 - Page 183
Lam Research Corp. v. Inpria Corp.
IPR2025-00256 - U.S. Patent No. 11,537,048

radiation is mainly absorbed by the PAG which initiates a cascade of reactions in the resist films. However, EUV radiation is mainly absorbed by resist polymers which generate negatively charged electrons and radicals.[10,11] The radicals are subsequently converted to protons and these protons catalyzed the chemical amplification process. Therefore, the efficiency of CAR utilizing EUV radiation to date is lower than when utilizing DUV radiation.

Moreover, out of band radiation in the wavelength range of 100 nm - 400 nm, which travel randomly in the resist film, is more readily absorbed by the PAG than nanoparticles. Therefore PAGs absorb this out of band radiation and generate anions for ligand exchange and protons for providing a low pH environment to facilitate ligand removal from the nanoparticles. The out of band effects on image blurring is likely less significant for ONE resists than CAR system.

Brainard *et al.* developed another type of metal oxo cluster EUV resist and they found the sensitivity decrease with the molecular weight of ligands for the tin-oxo and bismuth clusters.[12] Yet, we observed that these large molecular weight ligands which required much larger doses were all aromatic ligands, which is similar to our finds. In their recent studies, they found EUV sensitivity of antimony organometallic compounds decreased with the olefins loading.[13] Yet, in this study again, we also observed that the sensitivities decreased with increase number of aromatic ligands. Moreover, the antimony acrylate compound showed a sharper contrast curve compare to antimony acetate, which is similar to our dissolution results of saturated and unsaturated ligands although in a different kind of solvent.

Lam Research Ex. 1013 - Page 184
Lam Research Corp. v. Inpria Corp.
IPR2025-00256 - U.S. Patent No. 11,537,048

6.3.4. Effect of ligand on nanoparticle solubility

Carboxylic acid ligands not only prevent nanoparticles from aggregating in solution, they are also responsible for solubility changes in developer. Dissolution rate of hafnium oxide nanoparticles protected by 10 different ligands (BUA, CTA, IBA, MAA, IPA, DMA, MVA, MPA, IVA and SA) in 4-methyl-2-pentanol (4M2P) with and without exposure to 254 nm DUV radiation (150 mJ/cm^2) were measured by QCM. Among these aliphatic ligands, 5 of them are unsaturated and the other 5 ligands are saturated. They contain 3 to 5 carbons and are either linear or branched structures as shown in Figure 6.1. 10 wt. % of a nanoparticle solution was spun cast onto quartz crystals, followed by a post apply bake step at 110 °C to form uniform films. These crystals were then dipped into a slowly stirred beaker with developer and the thickness change was recorded as shown in Figure 6.5.

Nanoparticles with saturated ligands such as HfO_2-MAA, HfO_2-SA and HfO_2-MPA have larger dissolution rate differences after DUV exposure compared to nanoparticles with unsaturated ligands such as HfO_2-IBA or HfO_2-MVA. For negative tone development, larger dissolution rate differences between exposed and non-exposed nanoparticles are favorable to maintain a sharp contrast resist profile and absolute dissolution times affect control of the development process. Therefore, nanoparticles with unsaturated ligands showing a slower dissolution rate (>10 s) in 4M2P have advantages in overall lithography performance.

Lam Research Ex. 1013 - Page 185
Lam Research Corp. v. Inpria Corp.
IPR2025-00256 - U.S. Patent No. 11,537,048

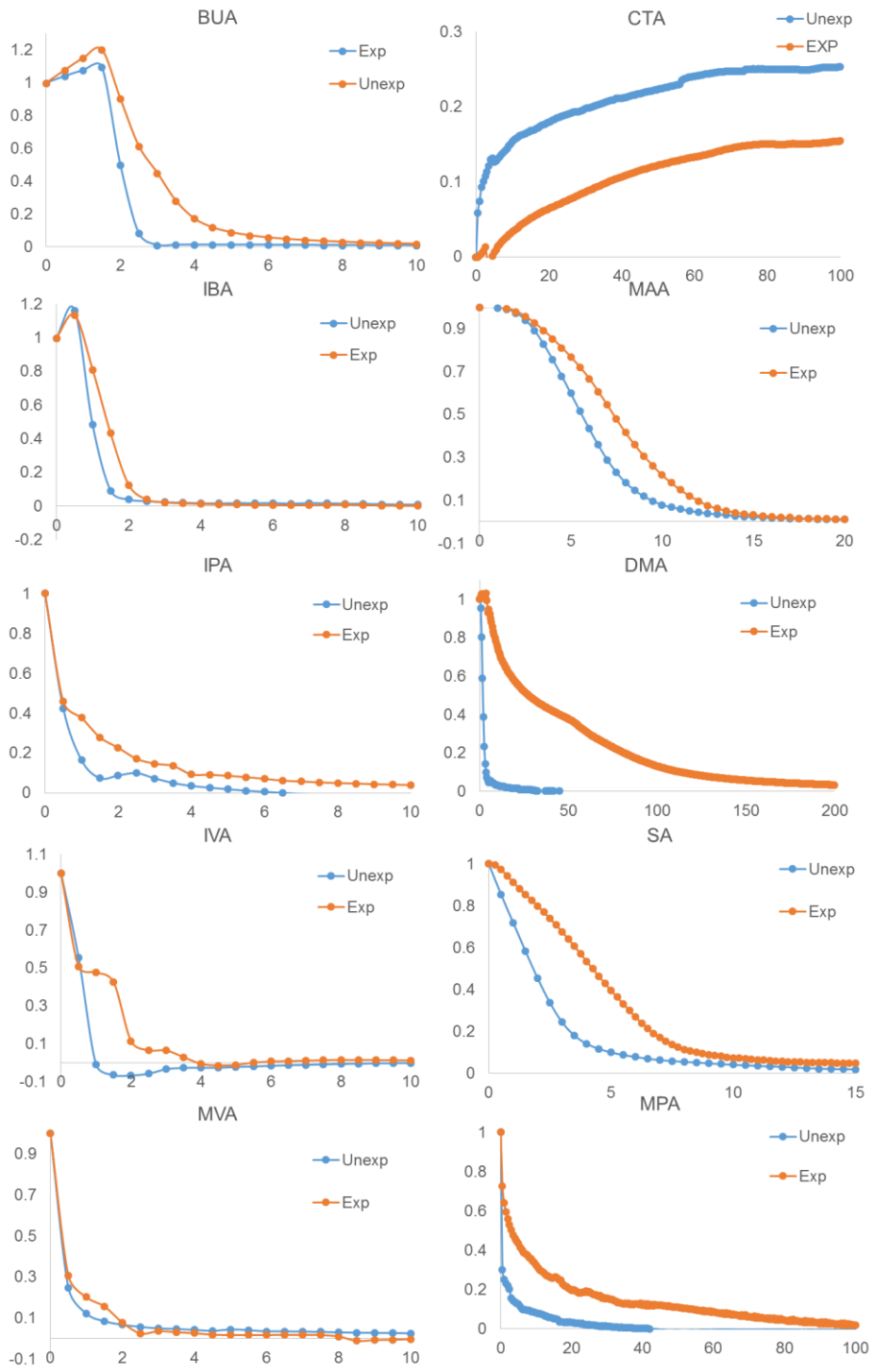

Figure 6.5 Dissolution rate of HfO_2-IBA, HfO_2-MAA, HfO_2-IPA, HfO_2-SA, HfO_2-MVA and HfO_2-MPA in 4M2P without and with exposure.

Lam Research Ex. 1013 - Page 186
Lam Research Corp. v. Inpria Corp.
IPR2025-00256 - U.S. Patent No. 11,537,048

6.3.5. DUV patterning of nanoparticle resist

6.3.5.1. Patterning capabilities and exposure sensitivities of nanoparticles for DUV lithography

Nanoparticles with various ligands were patterned using a DUV contact aligner operating at 254 nm. SEM images of resist patterns are shown in Figure 6.6. Due to the fast dissolution rate of HfO_2-MVA and HfO_2- IVA in 4-methyl-2-pentanol (4M2P) developer, no patterns were could be obtained for these two resists. The other 8 resists were DUV patterned at a dose of 150 mJ/cm^2. HfO_2-SA and HfO_2-DMA showed improved DUV sensitivity at less than 60 mJ/cm^2, developed in 1:1 PGMEA and 4M2P mixed solvents for 15 seconds. Although nanoparticles are generally less sensitive to DUV radiation, the relatively high DUV sensitivity might suggest a weak ligand strength. HfO_2-DMA in previous studies showed the highest EUV sensitivity. Therefore, we would expect the high DUV sensitivity of HfO_2-SA also translates into high EUV sensitivity.

Lam Research Ex. 1013 - Page 187
Lam Research Corp. v. Inpria Corp.
IPR2025-00256 - U.S. Patent No. 11,537,048

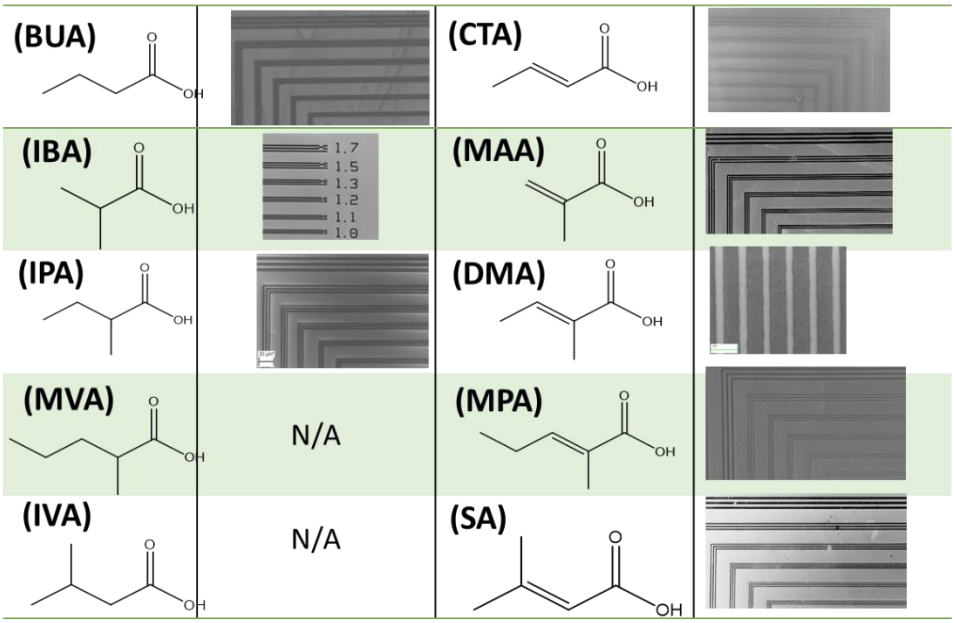

Figure 6.6 DUV patterning results of nanoparticles with various ligands. Patterning results of ZrO_2-MVA and IVA were not obtained due to their fast dissolution rate.

6.3.5.2. The effects of mixing nanoparticles with different solubility.

HfO_2-BUA and HfO_2-CTA were difficult to dissolve in several developers including 4M2P, PGMEA, 2-butanone or butyl acetate. ZrO_2-butyric acid did not dissolve in all these solvents even after hours of solvent exposure. ZrO_2-crotionic acid showed negative tone patterning only when using PGMEA as developer for 50 s; nevertheless the unexposed regions were hard to remove completely even after prolonged development (Figure 6.7). On the other hand, the ZrO_2-IVA thin films dissolved readily within 1 second for all these developers. The significant dissolution difference between linear (such as CTA and BUA) and branched (IVA) might arise from the higher van der Waals interaction between linear chains. Since linear chains tend to stack together better and have larger contact surface areas between chains, they

Lam Research Ex. 1013 - Page 188
Lam Research Corp. v. Inpria Corp.
IPR2025-00256 - U.S. Patent No. 11,537,048

are more difficult to dissolve once coated and annealed. But because double bonds of an unsaturated ligand (CTA) introduces “kinks” in the hydrocarbon backbone, unsaturated segments will not pack into a regular structure compared to saturated acid which slightly improved its solubility.

Resist	Developer/ time	DUV contact aligner
ZrO_2-IVA	PGMEA, 4M2P, Butyl acetate, 2-butanone, All resist washed away within 1s	
HfO_2-CTA ZrO_2-CTA	PGMEA 50s, Almost hard to dissolved in any solvents	
HfO_2-BuA ZrO_2-BUA	PGMEA, 4M2P, Butyl acetate, 2-butanone, o-xylene, Almost hard to dissolved in any solvents	

formula	Developer/ time	DUV contact aligner
ZrO_2-IVA: HfO_2-CTA 1:1 (5% PAG)	4M2P:PGMEA 1:2 (10S)	
ZrO_2-IVA: HfO_2-BUA 1:1 (3% PAG)	4M2P:PGMEA 5:1 (10s)	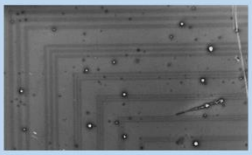

Figure 6.7 Effects of mixing nanoparticles with different solubility on the patterning

Mixtures of nanoparticles with branched/linear ligands were tested for their dissolution behavior using various solvents. By mixing a 1:1 ratio of easily dissolved nanoparticles (ZrO_2-IVA) and hard to dissolve nanoparticles (ZrO_2-CTA or BUA), either one of two

Lam Research Ex. 1013 - Page 189
Lam Research Corp. v. Inpria Corp.
IPR2025-00256 - U.S. Patent No. 11,537,048

possible situations may occur. The mixtures could either have moderate dissolution rate as a whole or the films might just partially dissolve. The results of development studies showed resist profile of both ZrO_2-crotonic acid and butyric acid mixtures with ZrO_2-IVA were improved. The exposed regions were completely removed during development, especially the mixture of CTA and IVA showed good resist profile (Figure 6.7).

6.3.6. The effects of base quenchers on EUV patterning of ZrO_2-MAA

Base quenchers are common additives in CAR formulations, which helps to suppress excessive acid diffusion. The effects of base quenchers for ONE resists were tested with ZrO_2-MAA. 1,8-Diazabicyclo[5.4.0]undec-7-ene (DBU) was chosen for this study. Free MAA was added to ZrO_2-MAA particles to adjust the organic content to 55% with 5 wt. % NI-tf (wrt nanoparticles) and 0.3 wt. % DBU (wrt nanoparticles) to prepare a 3 wt. % solution in PGMEA. The spin velocity was adjusted to form 40 nm film. After exposure to EUV light using the LBNL dark field reticle, the resist films were developed in 1:1 PGMEA and 4M2P developer. EUV patterning results with base quenchers are shown in Figure 6.9. The dose required for 1:2 22 nm line space patterns required a higher dose (9 mJ/cm^2) than previously reported results (5 mJ/cm^2)[1]. Base quenchers which reacted with PAG decomposition byproducts might decrease resist sensitivity, yet the role of base quenchers in ONE resists needs further investigation.

Lam Research Ex. 1013 - Page 190
Lam Research Corp. v. Inpria Corp.
IPR2025-00256 - U.S. Patent No. 11,537,048

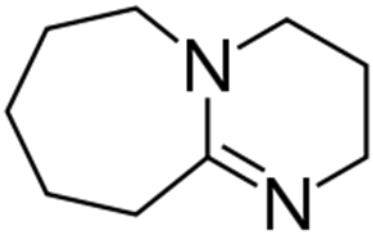

Figure 6.8 Chemical structures of base quencher DUB.

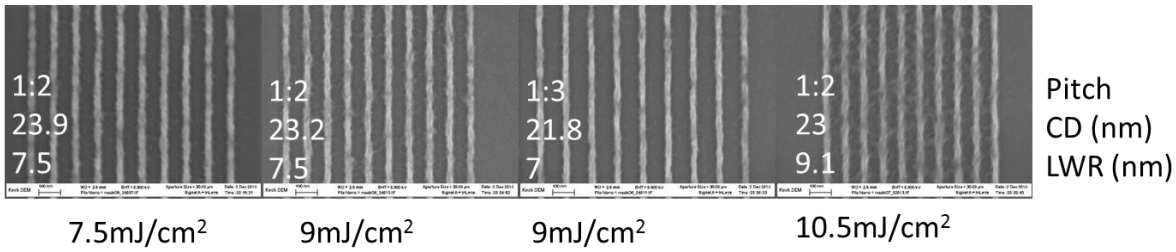

Figure 6.9 EUV patterning of ZrO_2-MAA with DBU.

6.3.7. Shelf life studies of nanoparticles.

The shelf life studies for nanoparticle resists involve two types of evaluations: 1) dynamic light scattering studies to examine whether aggregation occurred during storage and 2) EUV patterning to examine the sensitivity change and high resolution pattern quality. Nanoparticle resist powders are usually stored in a refrigerator at -4 °C and fresh solutions are prepared before spin coating. However, in many case these storage conditions might not always be available. Therefore the aging effects were assessed on nanoparticle solutions stored at either 40 °C or room temperature in the dark. The nanoparticle sizes of ZrO_2-MAA and HfO_2-

Lam Research Ex. 1013 - Page 191
Lam Research Corp. v. Inpria Corp.
IPR2025-00256 - U.S. Patent No. 11,537,048

benzoate measured by DLS remained approximately 2 nm suggesting no significant aggregation in solution had occurred after storing at 40 °C for 3 weeks.

The shelf-life studies of EUV performance were performed on ZrO_2-MAA formulated with 5 wt. % PAG and free MAA to adjust the organic content to 55% which had been stored at room temperature for 10, 45 and 80 days. Unfortunately, EUV patterning results of fresh samples analyzed by SEMATECH are not shown here due to the lack of availability of the data. The optimal doses for 22 nm of 0 d, 10 d and 45 d samples were 4.9 mJ/cm^2, 7.5 mJ/cm^2 and 16m J/cm^2 respectively (Figure 6.11). For 30 nm line space patterns, the doses for 0 d, 10 d, 45 d and 80 d are 3.5 mJ/cm^2, 6.3 mJ/cm^2, 12 mJ/cm^2. We were unable to obtain line space patterning of 80 d samples due to an underdose issue. Although some information is missing due to the limit of EUV availability, we can still observe a sensitivity decrease over time, in spite of its ability of maintain the same resolution from these data obtained.

We also observed increased development times for aged samples. The development time in 1:1 4M2P/PGMEA mixture required for fresh, 10 d, 45 d and 80 d samples were 10 s, 15s and 30s respectively. As discussed in Chapter 5, the main reason for dissolution rate changes are loss of ligands, ligand exchange and growth of Zr-O-Zr. However, it is unclear which mechanism dominates the ageing effects. Chemical analysis using FTIR or XPS is necessary to reveal an aging mechanism, yet, errors in measurement performed on samples on different days should be taken into account for subtle changes.

Lam Research Ex. 1013 - Page 192
Lam Research Corp. v. Inpria Corp.
IPR2025-00256 - U.S. Patent No. 11,537,048

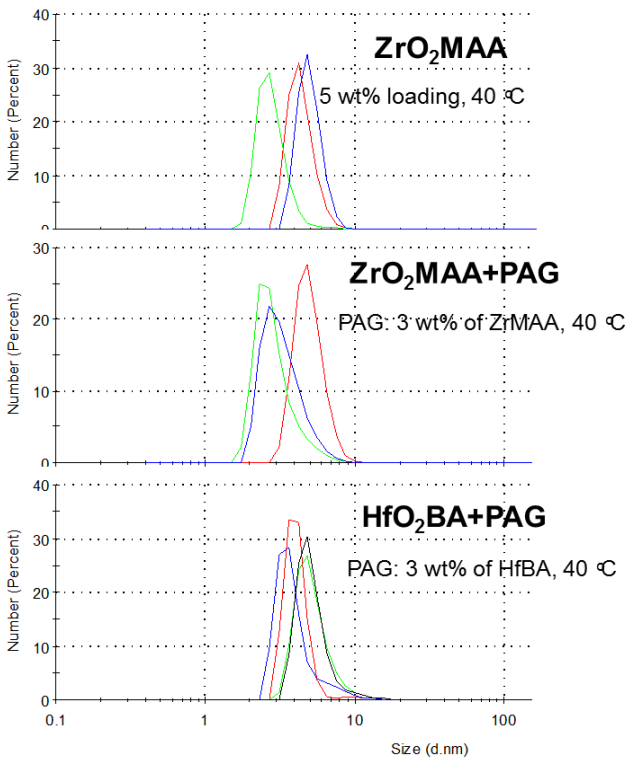

Figure 6.10 Nanoparticle size change of solution aging samples after 3 weeks.

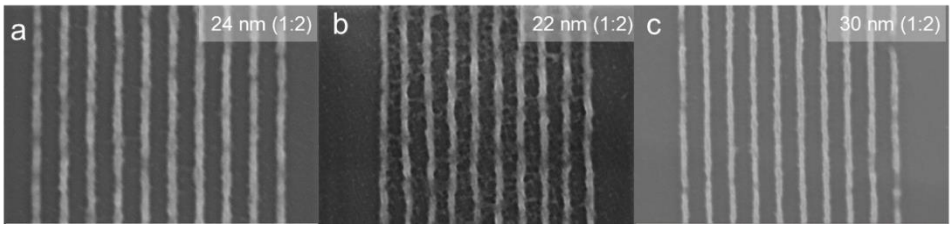

Figure 6.11 EUV patterning of aged solution. a) 10 days b) 45 days c) 80 days

Lam Research Ex. 1013 - Page 193
Lam Research Corp. v. Inpria Corp.
IPR2025-00256 - U.S. Patent No. 11,537,048

6.3.8. Development process

To enable nanoparticles to be tested on a 300 mm manufacturing EUV track, studies of automatic development processes are required to evaluate the changes of development methods on the patterning quality. For the dip-blow method (DB) which is currently used in the lab, resist residue is rinsed off when pulled from the solvent beaker and the developer is dried by N_2 flow (Figure 6.12a). For a more manufacturing compatible puddle-spin method (PS), resist residue and developer is spun off from the wafer (Figure 6.12b). Resist redisposition sometimes occurred when used the PS method, which is detrimental to the resist profile (Figure 6.13). Therefore, we adapted the PS method to a double PS method. Developer was first applied to wafers to dissolve the unexposed film and then spun off. Afterwards, developer was applied to wafers again to dissolve the residue and then spun off.

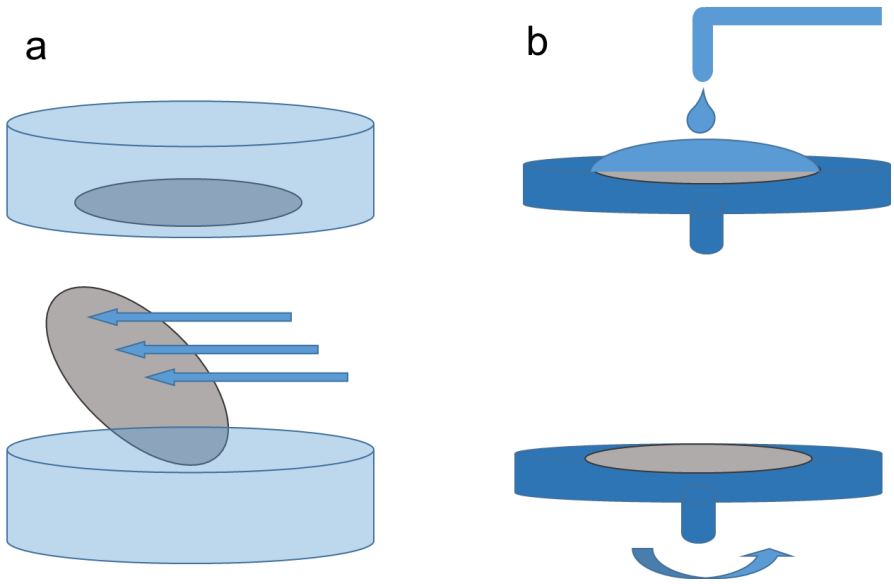

Figure 6.12 Schematic plot of two development processes

Lam Research Ex. 1013 - Page 194
Lam Research Corp. v. Inpria Corp.
IPR2025-00256 - U.S. Patent No. 11,537,048

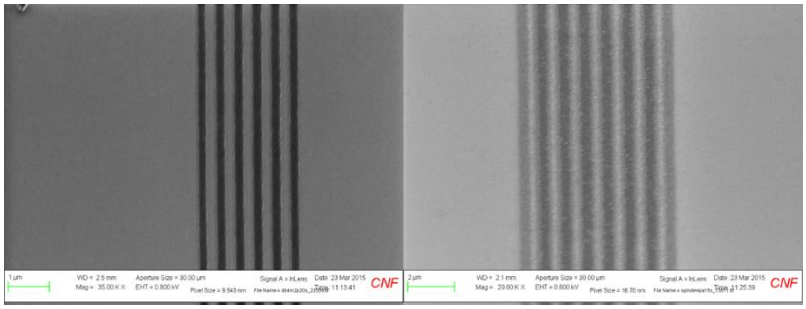

Figure 6.13 Comparisons of ZrO_2-MAA using dip-blow (left) and puddle-spin development (right). Resist residue was found to redeposit on the patterns.

The results of different development methods are shown in Figure 6.14. The dip-blow process used for 15 seconds demonstrated better fidelity to the mask for dense line space patterns; however, unexposed resist was not completely removed from the sparse bright field patterns. In comparison, the PS method effectively removed unexposed resist from the bright field sparse patterns, yet the line width of dense patterns was narrower than the mask patterns. Even for a short time double puddle-spin process (5+5 s), the real line width was 143 nm for a 250 nm target patterns. Nevertheless, double PS was able to achieve 130 nm lines for the bright field negative tone patterns which is very useful for via patterning. The overall development time for double PS is less than single PS.

Lam Research Ex. 1013 - Page 195
Lam Research Corp. v. Inpria Corp.
IPR2025-00256 - U.S. Patent No. 11,537,048

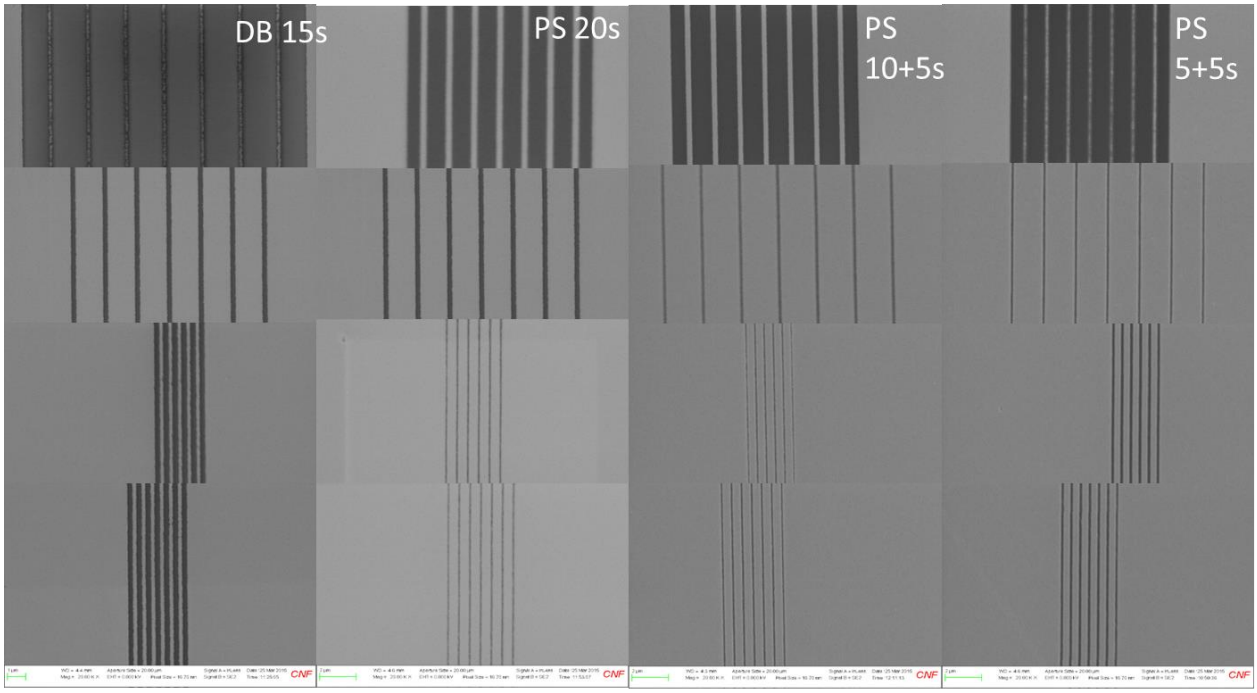

Figure 6.14 Effects of development recipe for 248 nm DUV patterning of ZrO_2-MAA. The first low is a bright field sparse line space patterns; second row is dark field sparse patterns; third row is bright field dense patterns; fourth row is dark field dense patterns

6.4. Conclusion

Nanoparticles with 12 different ligands were synthesized and characterized. Their ligand binding strength was measured using TGDTA. We found the unsaturated aliphatic ligands had progressive ligand loss during heating compared to saturated aliphatic ligands and aromatic ligands. The exothermic peak temperature above 300 °C which is the major ligand removal temperature showed some correlation with nanoparticle EUV sensitivities.

The dissolution rate of nanoparticles with 10 different ligands both with and without exposure were tested using QCM. Particles with unsaturated ligands shows greater dissolution rate

Lam Research Ex. 1013 - Page 196
Lam Research Corp. v. Inpria Corp.
IPR2025-00256 - U.S. Patent No. 11,537,048

change and longer dissolution time (>10 second) compared to saturated ligands, which is beneficial for overall lithographic performance.

Nanoparticles with various ligands were patterned with nonionic PAG using a DUV mask aligner. Most ligands have low sensitivity (150 mJ/cm^2) to DUV radiation; however, HfO_2-SA and HfO_2-DMA showed improved sensitivity (<60 mJ/cm^2). HfO_2-DMA was the most sensitive EUV resist among all nanoparticles tested, therefore we believe HfO_2-SA will also show extraordinary EUV sensitivity.

Shelf life studies of nanoparticles suggested no change in particle size or EUV resolution, but EUV sensitivity decreased and the development time increased. A new double puddle-spin method was developed for manufacturing compatible process steps.

ACKNOWLEDGEMENTS

The authors acknowledge SEMATECH for initial funding. The Cornell Center for Materials Research (NSF- DMR-1120296) and the Cornell Nanoscale Facility (Grant ECCS-0335765)), the KAUST-Cornell Center of Energy and Sustainability (KAUST_CU) and Lawrence Berkeley National Lab (DE-AC02-05CH11231) are thanked for the use of their facilities.

Reference

(1) Krysak, M.; Trikeriotis, M.; Schwartz, E.; Lafferty, N.; Xie, P.; Smith, B.; Zimmerman, P.; Montgomery, W.; Giannelis, E.; Ober, C. K. Development of an Inorganic Nanoparticle Photoresist for EUV, E-Beam, and 193nm Lithography. In *Proc. of SPIE*; 2011; Vol. 7972, p. 79721C – 79721C – 6.

Lam Research Ex. 1013 - Page 197
Lam Research Corp. v. Inpria Corp.
IPR2025-00256 - U.S. Patent No. 11,537,048

(2) Chakrabarty, S.; Ouyang, C.; Krysak, M.; Trikeriotis, M.; Cho, K.; Giannelis, E. P.; Ober, C. K. Oxide Nanoparticle EUV Resists: Toward Understanding the Mechanism of Positive and Negative Tone Patterning. In *Proc. of SPIE*; 2013; Vol. 8679, pp. 867906–867908.

(3) Chakrabarty, S.; Sarma, C.; Li, L.; Giannelis, E. P.; Ober, C. K. Increasing Sensitivity of Oxide Nanoparticle Photoresists. In *Proc. of SPIE*; 2014; Vol. 9048, p. 90481C – 90481C – 5.

(4) Jiang, J.; Chakrabarty, S.; Yu, M.; Ober, C. K. Metal Oxide Nanoparticle Photoresists for EUV Patterning. *J. Photopolym. Sci. Technol.* 2014, *27*, 663–666.

(5) Jiang, J.; Yu, M.; Zhang, B.; Neisser, M.; Chun, J. S.; Giannelis, E. P.; Ober, C. K. Systematic Study of Ligand Structures of Metal Oxide EUV Nanoparticle Photoresists. *Proc. SPIE*, 2015, *9422*, 942222–942226.

(6) Dong, T.-Y.; Chen, W.-T.; Wang, C.-W.; Chen, C.-P.; Chen, C.-N.; Lin, M.-C.; Song, J.-M.; Chen, I.-G.; Kao, T.-H. One-Step Synthesis of Uniform Silver Nanoparticles Capped by Saturated Decanoate: Direct Spray Printing Ink to Form Metallic Silver Films. *Phys. Chem. Chem. Phys.* 2009, *11*, 6269–6275.

(7) Hancock, R. D.; Martell, A. E. Ligand Design for Selective Complexation of Metal Ions in Aqueous Solution. *Chem. Rev.* 1989, *89*, 1875–1914.

(8) Rodgers, M.; Armentrout, P. Noncovalent Metal-Ligand Bond Energies as Studied by Threshold Collision-Induced Dissociation. *Mass Spectrom. Rev.* 2000, *19*, 215–247.

(9) Krysak, M. E.; Blackwell, J. M.; Putna, S. E.; Leeson, M. J.; Younkin, T. R.; Harlson, S.; Frasure, K.; Gstrein, F. Investigation of Novel Inorganic Resist Materials for EUV Lithography. In *Proc. of SPIE*; 2014; Vol. 9048, pp. 904805–904807.

(10) Yamamoto, H.; Kozawa, T.; Tagawa, S.; Cao, H. B.; Deng, H.; Leeson, M. J. Polymer-Structure Dependence of Acid Generation in Chemically Amplified Extreme Ultraviolet Resists. *Jpn. J. Appl. Phys.* 2007, *46*, L142.

(11) Kozawa, T.; Tagawa, S.; Cao, H. B.; Deng, H.; Leeson, M. J. Acid Distribution in Chemically Amplified Extreme Ultraviolet Resist. *J. Vac. Sci. Technol. B* 2007, *25*.

(12) Cardineau, B.; Del Re, R.; Marnell, M.; Al-Mashat, H.; Vockenhuber, M.; Ekinci, Y.; Sarma, C.; Freedman, D. A.; Brainard, R. L. Photolithographic Properties of Tin-Oxo Clusters Using Extreme Ultraviolet Light (13.5 Nm). *Microelectron. Eng.* 2014, *127*, 44–50.

(13) Passarelli, J.; Murphy, M.; Del Re, R.; Sortland, M.; Dousharm, L.; Vockenhuber, M.; Ekinci, Y.; Neisser, M.; Freedman, D. A.; Brainard, R. L. High-Sensitivity Molecular

Lam Research Ex. 1013 - Page 198
Lam Research Corp. v. Inpria Corp.
IPR2025-00256 - U.S. Patent No. 11,537,048

Organometallic Resist for EUV (MORE). In *Proc. SPIE*; 2015; Vol. 9425, p. 94250T – 94250T – 13.

Lam Research Ex. 1013 - Page 199
Lam Research Corp. v. Inpria Corp.
IPR2025-00256 - U.S. Patent No. 11,537,048